



KTH Engineering Sciences

Geant4 Monte Carlo Simulations of the International Space Station Radiation Environment

TORE ERSMARK

Doctoral Thesis
Stockholm, Sweden 2006

Cover image: The International Space Station seen from the space shuttle Discovery after undocking in August 2005 (courtesy of NASA).

TRITA FYS 2006:43
ISSN 0280-316X
ISRN KTH/FYS/--06:43--SE
ISBN 91-7178-398-9

KTH Fysik
SE-106 91 Stockholm
SWEDEN

Akademisk avhandling som med tillstånd av Kungl Tekniska Högskolan framlägges till offentlig granskning för avläggande av teknologie doktorsexamen fredagen den 9 juni 2006 klockan 13:30 i sal FD5, AlbaNova Universitetscentrum, Kungl Tekniska Högskolan, Roslagstullsbacken 21, Stockholm.

© Tore Ersmark, June 2006

Tryck: Universitetsservice US-AB

Abstract

A detailed characterization of the proton and neutron induced radiation environment onboard Columbus and the International Space Station (ISS) has been carried out using the Geant4 Monte Carlo particle transport toolkit. Dose and dose equivalent rates, as well as penetrating particle spectra corresponding to incident trapped protons, GCR protons, SPE protons and cosmic ray albedo neutrons are presented.

These results are based on detailed Geant4 geometry models of Columbus and ISS, comprising a total of about 750 and 350 geometry volumes, respectively. Additionally, the physics models of Geant4 have been validated with respect to space radiation shielding applications. Geant4 physics configurations based on the “Binary Cascade” and “Bertini Cascade” models of hadronic reactions were found to adequately model the particle interactions of the relevant space radiation fields. Other studied Geant4 models of hadronic reactions were found to be unsatisfactory for this application.

Calculated trapped proton dose rates are found to be strongly dependent on ISS altitude. Dose rates for different locations inside the Columbus cabin are presented, as well as for different models of the incident space radiation flux. Dose rates resulting from incident anisotropic trapped protons are found to be lower, or equal to, those of omnidirectional models. The anisotropy induced by the asymmetric shielding distribution of Columbus/ISS is also studied. GCR proton dose rates are presented, and it is demonstrated that the presence of thick shielding may increase the dose rate. A possible problem using Geant4 for future studies of effects induced by high-energy GCR ions is discussed. The dose rate due to cosmic ray albedo neutrons is demonstrated to be negligible.

The calculated trapped proton dose rates are $120 \mu\text{Gy/d}$ and $79 \mu\text{Gy/d}$ for solar minimum and maximum conditions, respectively. GCR dose rates are estimated based on calculated GCR proton dose rates to $161 \mu\text{Gy/d}$ and $114 \mu\text{Gy/d}$, respectively. These dose rates are found to be compatible with experimental measurements.

Contents

Contents	v
1 Introduction	1
1.1 The DESIRE project	1
1.2 The International Space Station	2
1.3 Author's contribution	3
2 Space radiation	7
2.1 The Sun	7
2.2 The Earth's magnetosphere and radiation belts	9
2.2.1 The outer belt	10
2.2.2 The inner belt	12
2.3 Galactic Cosmic Rays	13
2.3.1 Anomalous Cosmic Rays	13
2.4 SPEs	14
2.5 Cosmic ray albedo neutrons	14
2.6 Radiation biology and the space radiation environment	15
2.6.1 Dose, dose equivalent, equivalent dose	16
2.6.2 Heavy ions	17
3 Models of the Low-Earth Orbit radiation environment	19
3.1 Trapped electron belt models	19
3.2 Trapped proton belt models	21
3.2.1 Omni-directional models	21
3.2.2 Comparisons of omni-directional trapped proton models . .	23
3.2.3 Models of the trapped proton anisotropy	23
3.3 The GCR environment	24
3.4 Solar event particles	26
3.5 Cosmic ray albedo neutrons	27
3.6 Angular distribution of primary particles	28

4 Geant4	31
4.1 General properties of Geant4	32
4.2 Geant4 physics models	32
4.2.1 Electromagnetic interaction models	33
4.2.2 Hadronic interaction models	34
5 Tests and validation studies of Geant4	37
5.1 Validation by comparison to Los Alamos experimental data	38
5.2 Comparisons to SHIELD-HIT	38
5.2.1 Longitudinal and radial energy depositions	52
5.2.2 Neutron spectra	52
5.3 Comparisons to BRYNTRN	53
6 Geant4 geometry models of ISS and Columbus	57
6.1 ISS model	57
6.1.1 Habitable modules	59
6.1.2 Pressurized Mating Adapters	60
6.1.3 Other modules	60
6.1.4 Truncated ISS model	60
6.2 Columbus models	60
6.2.1 Columbus1	61
6.2.2 Columbus3	62
6.2.3 Columbus2	66
6.2.4 The Columbus models with/without ISS	66
6.3 Limitations of implemented models	66
7 Simulations of the Columbus/ISS radiation environment	69
7.1 Computational details	69
7.2 Comparison of geometry models	71
7.2.1 Simulated energy spectra	71
7.2.2 Simulated dose rates	72
7.3 Radiation belt protons	75
7.3.1 Altitude dependence	75
7.3.2 Dependence on model of incident environment and time in solar cycle	76
7.3.3 Dependence on location inside Columbus and anisotropic effects	80
7.4 Galactic cosmic rays	85
7.5 Solar particle events	88
7.6 Cosmic ray albedo neutrons	91
7.7 Conclusions and comparison to experimental data	91
8 Conclusions	95
Acknowledgments	97

List of Abbreviations and Names	99
List of Figures	103
List of Tables	109
Bibliography	111

Chapter 1

Introduction

With the advent of human spaceflight in the beginning of the sixties a number of new engineering challenges were encountered. While problems related to the increased radiation levels in space were certainly not among the most serious problems of that time, they are still an important and partly unsolved issue today. The increase of the radiation intensity at high altitudes was discovered already during the first years of the 20th century. A few years before the first manned missions the Earth's radiation belts were discovered and transient increases of radiation related to solar flares were also known of. In retrospect, the solar particle event on August 4, 1972 serves as an important reminder of what could have happened already during the short-duration missions of the early space-programs. The event occurred between the Apollo 16 and 17 missions, had it occurred during one of the missions the effects on the health of the astronauts would likely have been severe [1]. Early radiation related death would probably have been averted, at least with medical intervention. Later effects, such as leukemia, would however probably have manifested soon after the exposure.

Studies of the effects of radiation on astronauts on long-duration missions to space stations has been made both in the U.S. and Russia. So far no studies of the radiation situation onboard the International Space Station (ISS) have been done in Europe. It is of great importance and of general interest to do this since European astronauts will shortly be on long duration missions on ISS.

1.1 The DESIRE project

DESIRE is an acronym for “Dose Estimation by Simulation of the ISS Radiation Environment”. The ultimate goal of the project is to accurately calculate the radiation fields inside the European “Columbus” laboratory module on ISS, and to use them to estimate the radiobiological effects on astronauts. The subject of this thesis are the results from the project. A long-term goal of this activity has been the development of a European software package that can be used to predict

the radiation risks for other potential manned space flights, both in Low-Earth Orbit (LEO) and outside.

The accurate prediction of astronaut health risks due to space radiation rests on three separate sets of problems:

- What are the incident radiation fields outside of the space vehicle?
- How are the radiation fields transformed in the available shielding?
- What are the radiobiological effects of the radiation fields?

Information on the incident radiation fields includes the abundances of the various particle species and their energy distributions. Knowledge of the directional dependence of the radiation field is required if the attitude of the space vehicle is well defined with respect to the radiation field. The occurrence and parameters of some fields, such as solar particle events, are stochastic, and require statistical models of e.g. worst-case scenarios. Incident radiation field data can be retrieved from standard sources, such as the European Space Agency (ESA) Space Environment Information System (SPENVIS) system [2] or from the Cosmic Ray Effects on Micro-Electronics (1996 revision) (CREME96) [3]. These data are typically produced by models based on measurements of the radiation fields at some orbits or trajectories at certain dates and then by theoretical predictions extrapolated to more general future orbits. The various radiation field components in LEO are described in chapter 2.

The behavior of radiation in materials is in general a well investigated subject. Accurate radiation calculations are important in a wide variety of disciplines such as nuclear energy, medical radiation physics, high-energy physics, and of course space radiation shielding. The tool chosen for radiation transport in the DESIRE project is the 3-D Monte Carlo particle transport toolkit Geant4 [4] [5]. At present, commonly used particle transport programs for human space applications are not Monte Carlo based. Instead they rely on a simpler approximative method of 1-D straight-ahead propagation and transformation of radiation fields in a given mass thickness. Geant4 originated in the high-energy physics community at the European Organization for Nuclear Research (CERN), but are nowadays developed by a large international collaboration including many institutes and universities as well as ESA. A short introduction to Geant4 and its physics models important for the DESIRE project is available in chapter 4.

Detailed radiobiological effects of space radiation, such as radiation doses to individual organs, are not treated in this thesis. A brief introduction to effects of space radiation and dose equivalents, which may generally be interpreted as “risks”, is offered in section 2.6.

1.2 The International Space Station

ISS operations began on 20 November 1998 with the launch of the Zarya module and the subsequent arrival of the first crew. Since then it has been the only permanently

inhabited human outpost in space and has been extended with several additional pressurized modules, as well as solar power and radiator facilities. The present ISS configuration is shown in Fig. 1.1.

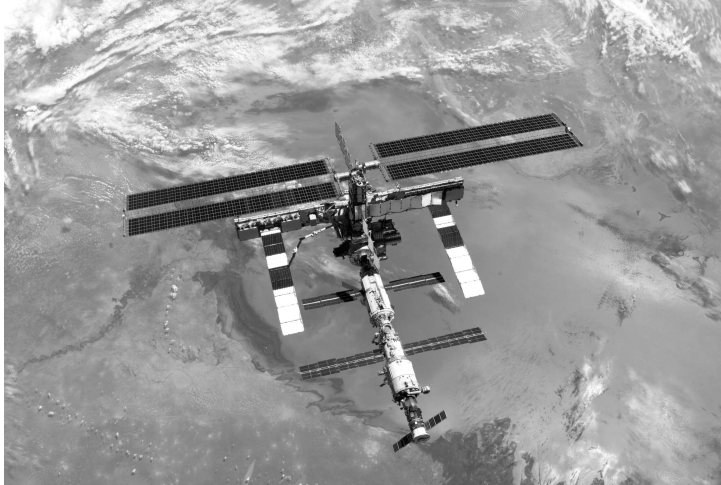


Figure 1.1: Photo of ISS taken from the space shuttle Discovery in August 2005 (courtesy of NASA).

ISS is in a 51.6° inclination circular orbit, i.e., the angle between the plane of the orbit and the equatorial plane is 51.6° . This means that it during each orbit reaches as far north as the approximate latitude of London, and about as far south as the southern tip of South America. Fig. 1.2 shows an example of the ISS ground track for three consecutive orbits. Fig. 1.3 shows the ISS altitude history since launch. The sawtooth shape of the graph reflects the gradual decline of the orbit due to friction losses in the residual upper atmosphere, and subsequent reboosts to maintain altitude. The decline of the orbit during the last two years presented in the graph is due to changed operational circumstances following the tragic loss of the Columbia Space Shuttle on 1 February 2003. The design certification of the Zvezda module limits the ISS maximum altitude to about 460 km. The lower altitude limit is about 280 km, based on friction with the upper atmosphere.

The ISS orbit type and altitude determines the incident radiation environment. This is further discussed in chapters 2 and 3.

1.3 Author's contribution

As noted above, chapters 1, 2, 3 and 4 are introductions to human spaceflight, ISS and radiation related issues as well as the space radiation environment and the Monte Carlo particle transport toolkit Geant4 [4] [5]. The remaining chapters 5, 6, 7, and 8 detail the results of the Author's research.

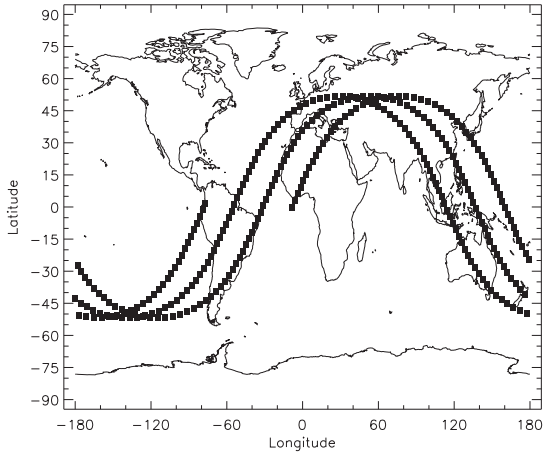


Figure 1.2: ISS ground track for three consecutive orbits.

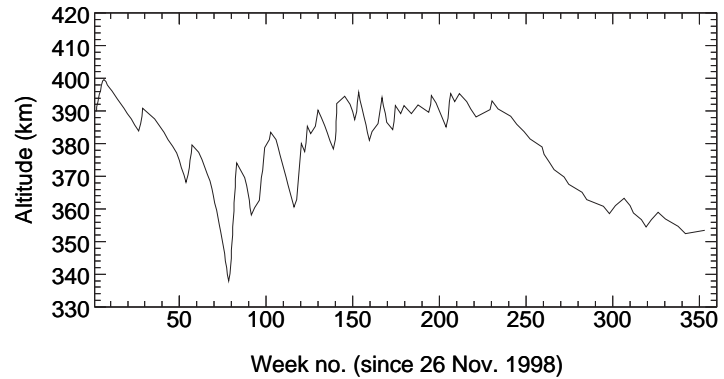


Figure 1.3: ISS altitude history since launch. The most recent data in the plot are from 5 August 2005 (altitude data courtesy of NASA).

The Author was solely responsible for the Geant4-based simulation results in chapter 5. This involved development of C++ simulation and analysis applications for the Geant4 and ROOT [6] libraries under Linux. Also the BRYNTRN simulation results were produced by the Author. Furthermore, most of the evaluation of the simulation results was made by the Author. The Geant4 geometry models of chapter 6 were developed solely by the Author. The simulation results presented in chapter 7 are the product of C++ simulation and analysis applications for the Geant4 and ROOT libraries developed solely by the Author.

Furthermore, results of the Authors research are published [7] or submitted for

publication [8] in refereed scientific journals. Further publications based on the results in sections 7.3–7.6 are in preparation. During the course of the DESIRE project the Author has been actively involved in the space and particle physics community around Geant4. This has included proposing requirements for space radiation studies to Geant4-developers and alerting them of software bugs as well as physics model deficiencies. The major software issues found and reported by the Author were: 1) A serious bug in coordinate-transformations in the Geant4 General Particle Source (GPS) module. The bug was present in Geant4 versions prior to 7.0 and corrected by the Author. Later versions of Geant4 features a re-engineered GPS, and are thus unaffected. 2) The first released versions of the Geant4 Binary Cascade and Bertini Cascade models of hadronic physics were discovered to have serious software stability problems. A consequence of this is the absence of Bertini Cascade-based simulation results in [7]. Simulations involving the element hydrogen were especially affected.

Chapter 2

Space radiation

This chapter offers a conceptual overview of the radiation environment in Low-Earth Orbit. Models of the space radiation environment and resulting predictions are presented in chapter 3.

The radiation environment close to Earth consists of three main components: Trapped particles, Galactic Cosmic Rays (GCRs) and Solar Particle Events (SPEs). None of the components are constant in time, mainly due to variations in the activity of the Sun. Solar activity influences the Earth's magnetosphere, which in turn determines the extent of the trapped particle radiation belts. The variation of incident GCR fluxes are determined by both the magnetosphere and the solar wind. SPEs are the result of acceleration of energetic particles in the Sun's outer layers. These particles are transported to the Earth under influence of the solar wind.

2.1 The Sun

There is a flow of nearly completely ionized plasma into space from the outer part of the Sun's corona. The plasma flow is called the solar wind and consists mainly of hydrogen with a small component of He (4%) and other ions. The particles in the solar wind have energies much higher than the energy in the magnetic field at the point of origin. This and the very high conductivity of the plasma results in the solar wind carrying a "frozen in" magnetic field out into space, forming the Interplanetary Magnetic Field (IMF). Because of the rotation of the Sun the field forms an Archimedean spiral, see Fig. 2.1. The IMF and the solar wind permeates the entire solar system all the way through the heliosphere out to the heliopause where the charged component of the interstellar gas starts to dominate. The distance to the heliopause in the direction of the Voyager 1 probe is estimated to be about 155 AU.

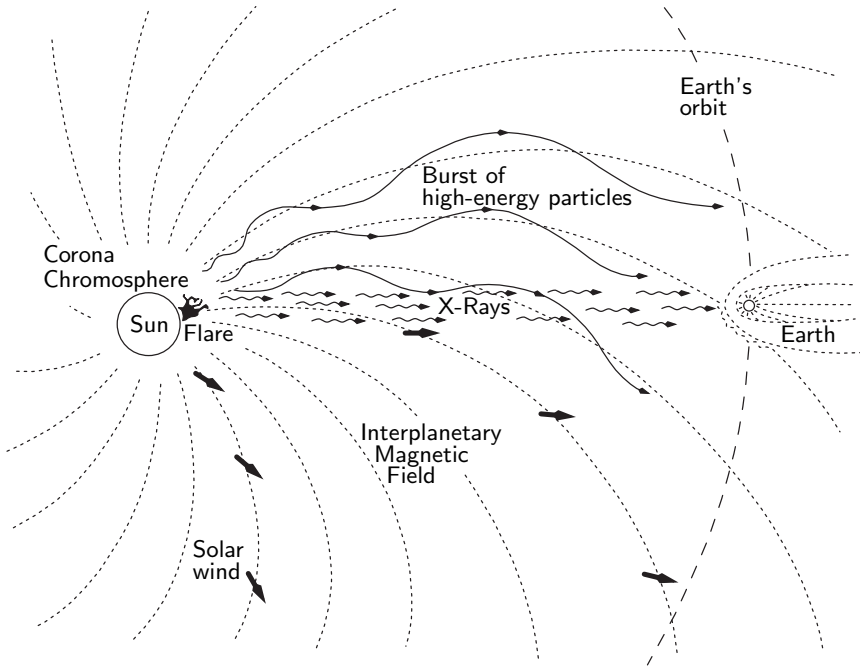


Figure 2.1: The IMF and propagation of energetic particles from the Sun (adapted from [9]).

Many features of the dynamic Sun are periodic. The main cycle, the solar cycle, has a period of 11 years and is defined by the reversal of the Sun's magnetic poles. The solar cycle starts by convention at solar minimum with the Sun in a state with a well defined dipole-like magnetic field. During the following 11 years the field first breaks down to a disorganized state (solar maximum) and is later restored to a dipole-like field again with opposite polarity compared to the previous configuration¹. The most easily detected feature of solar activity are the sunspots, which are areas of lower temperature than the surrounding surface. The difference is due to increased magnetic activity, which limits convective equalization of the temperature. The Sunspot Numbers (SSNs) have been recorded since 1610 with daily observations starting in 1749. Fig. 2.2 shows the monthly smoothed sunspot number, demonstrating the 11 year solar cycle. Also the solar wind and the IMF follows the solar cycle and thus exerts a larger influence at solar maximum than at solar minimum.

¹The proper 22 year periodic cycle between configurations with identical polarity is called the double solar cycle. The most prominent dynamic features of the Sun are not sensitive to the polarity of the magnetic field and thus exhibit a 11 year cycle

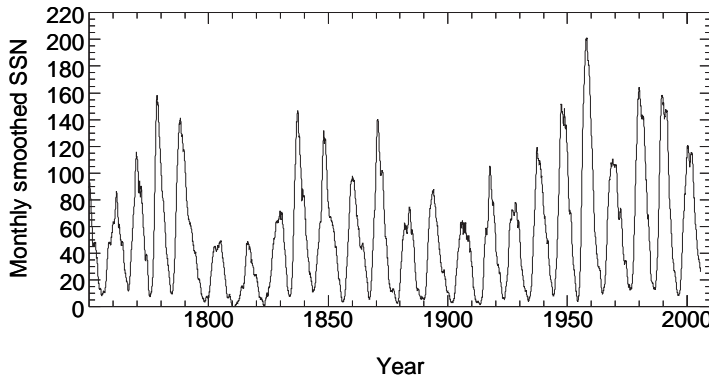


Figure 2.2: The SSNs from 1750 until today (according to [10]).

2.2 The Earth's magnetosphere and radiation belts

The solar wind is interrupted by the Earth's geomagnetic field at approximately 10.5 Earth radii on the sunward side, see Fig. 2.3. The exact distance varies by several Earth radii with the variation of the solar wind pressure. The interface is called the magnetopause and is the outer boundary of the Earth's magnetosphere. Ahead of the magnetopause there is a termination shock front ("bow shock") and inside it is the magnetosheath where the solar wind flows around the magnetosphere. Inside the magnetosphere, shielded from the solar wind there are several distinct regions, such as the plasmasphere, the cusp, the magnetotail and the two radiation belts.

The radiation belts are the most important regions concerning radiation shielding. They were discovered by the very first U.S. satellite, Explorer 1 in 1958 (later confirmed by Explorer 3) headed by James van Allen, and are thus sometimes referred to as Van Allen belts. The detector on Explorer 1 (based on a Geiger-Müller tube) was designed for measuring the increasing intensity of cosmic radiation as a function of altitude. In the belt the detector was saturated due to the strong radiation.

In the vicinity of Earth the geomagnetic field is well approximated by a dipole. In such a field charged particles can (theoretically) stay indefinitely trapped because of magnetic mirroring, see Fig. 2.4. The motion of trapped particles consists of three periodic components: 1) Gyration around a magnetic field line; 2) Movement along the field line with magnetic mirroring at the end-points; 3) Longitudinal drift (west for positive particles, east for electrons). This results in stable belts of trapped radiation around Earth, forming a potential hazard for spacecrafts. Also Jupiter and Saturn are known to possess radiation belts. Fig. 2.5 shows a sketch of the spatial distribution of trapped particles around Earth. Two radiation belts are traditionally recognized, with a slot of lower radiation intensities in between. The

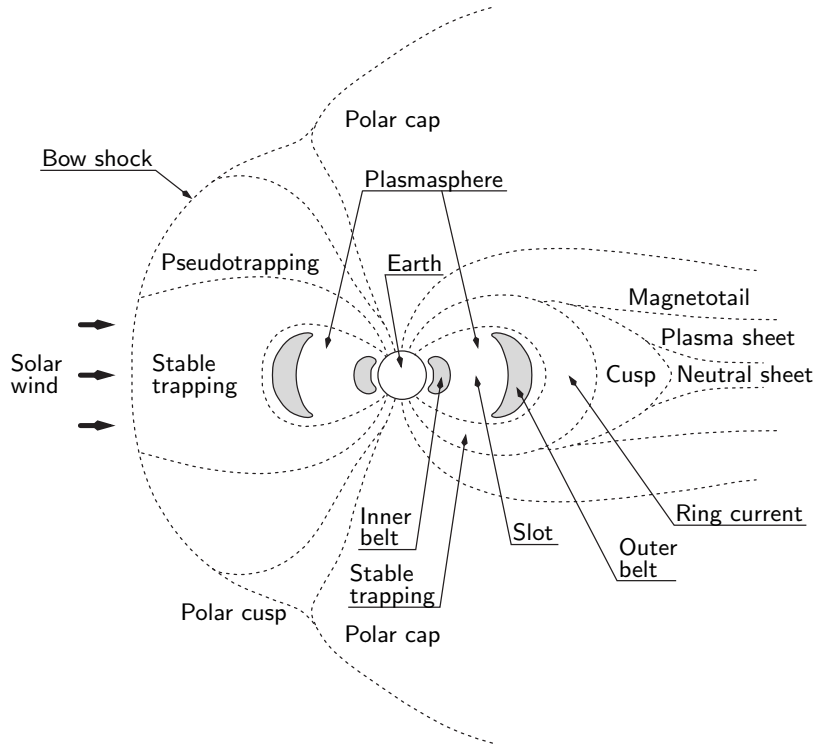


Figure 2.3: The magnetosphere viewed in the Earth's orbital plane (adapted from [11]).

trapped particle belts consist of electrons, protons as well as a minor population of ions. Out of these, only the protons of the inner belt are important for effects inside the ISS.

2.2.1 The outer belt

The outer radiation belt consists actually of trapped plasma, with the higher-energy distribution of the plasma being referred to as a radiation belt. The maximum electron energy in the outer belt is about 10 MeV. While the electron flux may cause problems for components located outside a spacecraft (e.g., solar cell degradation) they are unimportant for effects inside a heavily shielded spacecraft such as ISS.

From Fig. 2.5 it should be apparent that not only the altitude of a spacecraft affects the incident radiation flux, but also the orbital inclination (the angle between the orbital and equatorial planes). The northern and southern regions where the outer radiation belt goes down to very low altitudes, are called the polar horns and pose a possible hazard to spacecraft in high-inclination orbits. The outer belt is

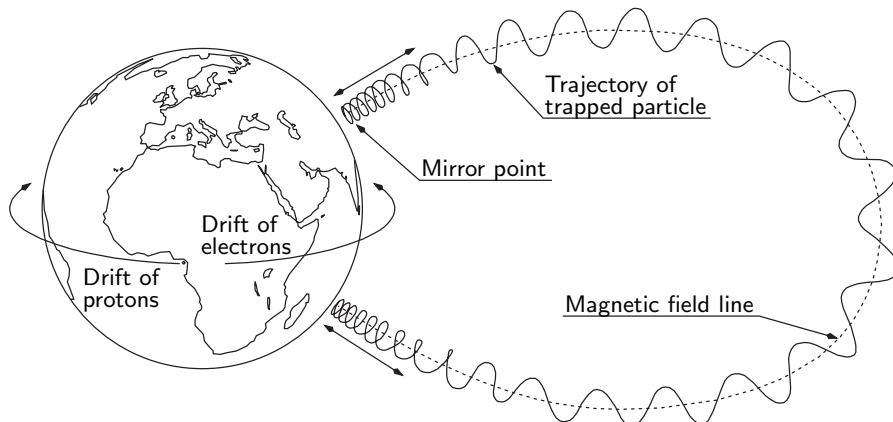


Figure 2.4: Motion of trapped particles in the geomagnetic field (adapted from [11]).

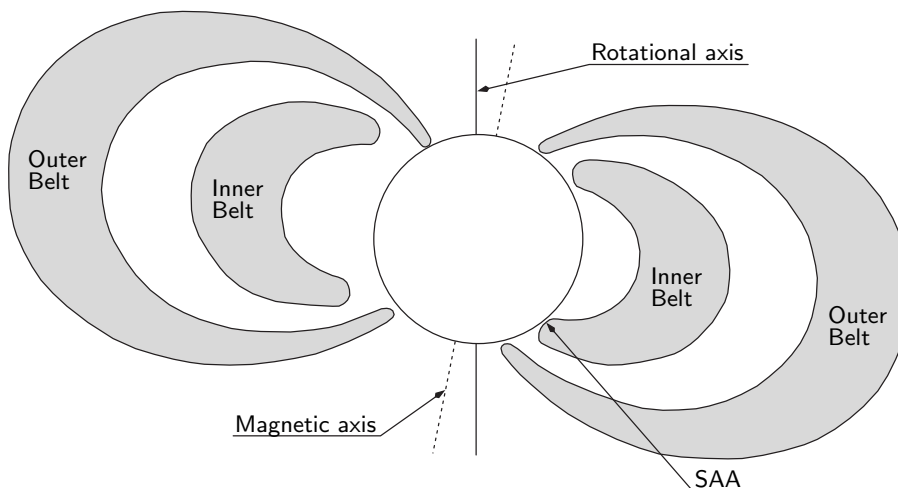


Figure 2.5: The Earth's radiation belts and the SAA.

easily influenced by solar activity and the Earth's polar regions are less shielded by the geomagnetic field from solar disturbances. Because of this the radiation intensity in the polar horns, as well as their exact geographical extent, are subject to large fluctuations at times of increased solar activity. The ISS orbit barely touches the polar horns at low solar activity, but may spend a non-negligible part of the orbit in them during magnetic storms.

2.2.2 The inner belt

The inner belt consists mainly of protons with energies up to a few hundred MeV. There is also a minor number of electrons and ions present. The proton belt is located at low altitude, extending out to about four Earth radii at the equator. As such, it is in general well shielded from the solar wind and therefore very stable. Protons are injected into the belt through decay of neutrons in the belt region as well as by diffusion from outer regions [12]. The neutrons are created as secondary particles in cosmic ray interactions with the atmosphere, and then scattered back into space, see section 2.5. This mechanism is known as Cosmic Ray Albedo Neutron Decay (CRAND). Protons can be lost at the outer edge of the belt during disturbances caused by geomagnetic storms and by interaction in the upper atmosphere.

Temporal variation of trapped proton fluxes at low altitudes is also induced by the solar cycle. At solar maximum the insolation is greater, leading to expansion of the upper atmosphere and enhanced trapped proton losses at low altitudes. Therefore, the radiation hazard associated with trapped particles is less at solar maximum. The dependence on solar activity also induces cycle-to-cycle variations of trapped proton fluxes due to differences in activity between different solar maxima.

The South Atlantic Anomaly

An important feature of the inner belt is the South Atlantic Anomaly (SAA). While the geomagnetic field at low altitudes is well approximated by a dipole field, this field is however not symmetric around the Earth. The axis joining the Earth's north and south poles is not parallel to the Earth's rotational axis, but tilted 11°. Furthermore, the center of the geomagnetic field is currently offset from the center of the Earth by more than 500 km. A consequence of this is the presence of trapped particles in the inner belt down to very low altitudes above the south Atlantic ocean, off the coast of Brazil. A spacecraft in LEO (such as ISS) will encounter trapped protons only in this region and with increasing fluxes at higher altitudes.

The east-west anisotropy

The trapped proton flux is strongly anisotropic in the SAA. In studies of an orbit-stabilized spacecraft, such as the ISS, it is important to take this effect into account. The anisotropy is caused by the non-negligible increase in atmospheric density for altitude differences comparable to the proton gyro-radii. Protons arriving from the east must gyrate around a field line at a lower altitude than those arriving from the west. Therefore, due to increased proton interaction probability with the residual upper atmosphere at lower altitudes, the flux from the east is thus less than that from the west. High-energy proton fluxes exhibit a more pronounced anisotropy than the low-energy component due to the greater gyro-radii and thus the greater difference in atmospheric density. Furthermore, at higher altitudes the atmospheric density differences are smaller and the anisotropy thus smaller. Another source of

anisotropy is caused by the protons in the SAA being near their mirror points and thus have pitch-angles close to 90° , as shown in Fig. 2.4.

2.3 Galactic Cosmic Rays

At the beginning of the 20th century it was found that the amount of measured background radiation exceeded that which could be attributed to natural sources. During a pioneering balloon flight in 1912, Victor Hess established the existence of cosmic radiation by measuring the increase of radiation intensity with altitude. The radiation intensity increases with altitude because of decreasing atmospheric shielding. After reaching the altitude with highest radiation intensity (the Pforzheim maximum), the intensity decreases because of a decreasing number of secondary particles generated in the cosmic ray showers. A small part of the cosmic radiation are the (incorrectly named) low-energy solar cosmic rays. The by-far dominant part is of galactic origin and is believed to result from Fermi acceleration of particles in supernova remnants to near the speed of light. The GCRs stay trapped inside the galaxy by the galactic magnetic field, and have in general traversed the galaxy several times before arriving at Earth. The GCR flux consists of 90% protons, 9% alpha particles and 1% ions.

Not taking into account the effect of the geomagnetic field, the GCR intensity monotonically decreases with increasing energy. The energies of the GCRs span a wide range up to at least 10^{19} GeV/nuc. The nature of the high-energy GCRs is a very interesting subject in astrophysics. However, for the purpose of radiation protection for manned space missions it is adequate to only consider particles with energies below tens of GeV/nuc because of the low fluxes at high energies.

The GCRs are, as all charged particles, influenced by the magnetic fields they traverse. For GCRs in near-earth space these are the IMF and the geomagnetic field. The variation of the IMF with the solar cycle (which increases at solar maximum) modulates the GCR intensity resulting in lower fluxes at solar maximum. Furthermore, the geomagnetic field removes the lowest energy particles, decreasing the particle flux below about 1 GeV/nuc. This effect is latitude dependent, being most effective at the magnetic equator and not relevant at all for particles incident exactly along the geomagnetic axis. The GCR radiation hazard is thus dependent both on altitude and orbital inclination.

2.3.1 Anomalous Cosmic Rays

Anomalous Cosmic Rays (ACRs) are singly or multiply-ionized ions that have their origin in the interstellar neutral atomic medium. When entering the heliosphere such atoms may get singly ionized by ultra-violet radiation from the Sun, or from charge-exchange reactions with solar wind protons. They are then carried with the solar wind out to the termination shock at the edge of the heliosphere and accelerated to tens of MeV/nuc. Stripping of further electrons at the shock may result in multiply charged ACRs with energies up to about 100 MeV/nuc. Because of

their low ionization, ACRs can penetrate much deeper into Earth's magnetosphere than ordinary GCRs. In the past, it was thought that if ACRs had a hard spectra they would be significant part of the LEO environment. Today their energies and multiplicities are known to be too low for that.

2.4 SPEs

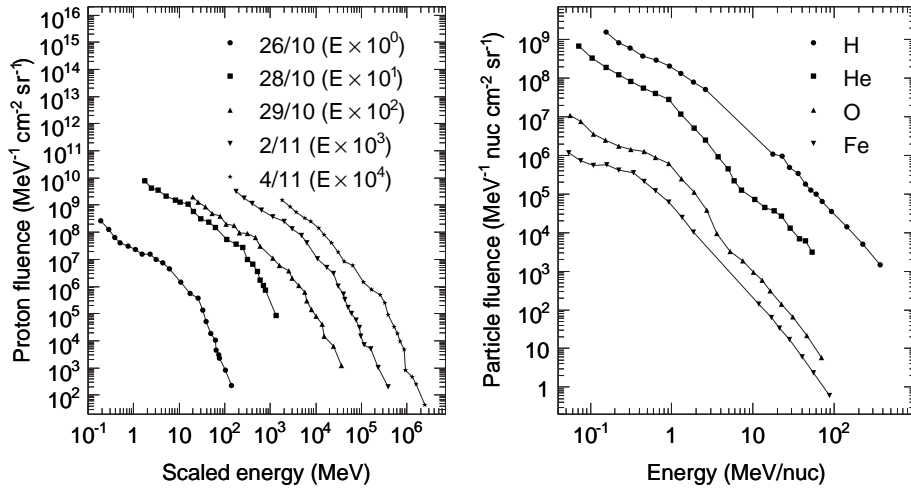
Solar Particle Events (SPEs) are associated with so-called solar flares, which are thought to be the result of great magnetic disturbances on the Sun. Such energetic events are common only to the period of solar maximum, though small events may occasionally occur during solar minimum. During the events it is thought that the magnetic field lines extending out from the Sun are tied off and reconnected to the surface. This produces an acceleration of protons to hundreds of MeV as well as an associated X-ray flare, see Fig. 2.1.

The flux of solar particles (protons and ions) at the Earth is dependent on the IMF connection between the Earth and the location of the event at the Sun and can persist for several days. The geomagnetic field decreases the ability of low-energy particles to penetrate to low altitudes, especially at lower latitudes, thus providing some protection from SPE particles (like for GCRs). However, solar events are usually associated with increased solar activity, which influences the stability of the geomagnetic field (so-called magnetic storms). It is well known that during such storms, charged particles can penetrate deeper into the magnetosphere than at other times.

Fig. 2.6 shows experimental data from the ACE, SAMPEX and GOES-11 space-crafts published in [13]. Note that particles with energies above and below the minimum and maximum displayed energies also exist, but have not been measured in this case. The rise and decline of the proton fluence during the course of the October-November 2003 SPE is shown in Fig. 2.6(a). Fig. 2.6(b) shows the contribution of different ions relative to protons for the January 2005 SPE particle fluences.

2.5 Cosmic ray albedo neutrons

In addition to the three previously mentioned LEO radiation environment components, there is a minor contribution from so-called cosmic ray albedo neutrons [12]. When high-energy GCRs hit the atmosphere of a planet and interact, they start a particle shower where successive generations of secondary particles give rise to their own secondaries thus resulting in a great number of particles propagating through the atmosphere. Some of these, most notably neutrons, can be backscattered and escape the atmosphere. Escaping charged albedo particles will propagate according to the geomagnetic field and be absorbed by the atmosphere at about the same latitude where they were created. If the albedo neutrons decay in the belt-region, the decay protons can be trapped and replenish the radiation belts



(a) Proton fluences at different dates during the October-November 2003 SPE. The data for the different dates have been separated using the indicated scale factors.

(b) Proton and ion fluences from the 20 January 2005 SPE.

Figure 2.6: SPE particle fluences for the October-November 2003 and January 2005 events according to [13]. Data are from the ACE, SAMPEX and GOES-11 spacecrafts. The data for the different dates have been separated using the indicated scale factors.

(CRAND-mechanism). However, it is clear that there is a contribution from cosmic ray albedo particles to the space radiation environment close to a planet. This contribution decreases approximately with the inverse of the radial distance squared (ignoring possible particle decay). In contrast to the previously discussed charged particles, neutrons are difficult to shield against since they are uncharged and do not interact electromagnetically in the hull of a spacecraft.

2.6 Radiation biology and the space radiation environment

In contrast to commonly studied radiation environments posing a hazard to humans, such as medical treatment facilities and nuclear reactors, space offers an unusually complex radiation environment. The relevant energy range up to several tens of GeV/nuc for GCRs. Secondary particles such as neutrons, leptons, photons and mesons resulting from interactions of high-energy particles in the spacecraft hull need to be taken into consideration, as well as the primary particles themselves,

mostly protons and ions.

Ionizing particles pose a hazard by depositing energy when passing through human tissue. Non-ionizing particles contribute to the hazard by the creation or spallation of ionizing particles upon reaction with tissue medium. The main contribution come from primary trapped protons and GCRs, as well as secondary protons and neutrons, while e.g., X-rays are negligible. The presence of the space-craft hull, or indeed any kind of shielding material, decreases the internal radiation environment caused by the low-energy component of the primary ionizing radiation. Increasing the shielding thickness may be unfeasible due to launch-mass restrictions. However, the internal radiation environment due to the high-energy component of the primary ionizing radiation may increase with increasing shielding thickness. This effect is due to creation of secondary particles in interactions of the primary radiation in the spacecraft shielding.

2.6.1 Dose, dose equivalent, equivalent dose

The absorbed dose, D , is the amount of energy deposited in a volume of material divided by the mass of the volume. It is well known that the radiation risk is not only dependent on the absorbed dose. Factors such as particle species, energy, and rate of energy loss are also relevant. Such factors are combined in calculations which turn the absorbed dose into quantities more suitable for risk assessment. Two common quantities are the dose equivalent and the equivalent dose, which are calculated with the radiation quality factor (Q) and the radiation weighting factor (w_R) respectively.

The dose equivalent can according to [14] be calculated as the sum of all track energy depositions, weighted by Q ,

$$H = \sum_i D_i Q(L_i)$$

where

$$Q(L) = \begin{cases} 1 & L < 10 \text{ keV}/\mu\text{m} \\ 0.32L - 2.2 & L \in [10, 100] \text{ keV}/\mu\text{m} \\ 300/\sqrt{L} & L > 100 \text{ keV}/\mu\text{m} \end{cases}$$

and L is the unrestricted Linear Energy Transfer (LET) in water.

In contrast, the equivalent dose is calculated as

$$H = \sum_R w_R D_R$$

where D_R is the absorbed dose due to radiation of type R and w_R is the radiation weighting factor for radiation R according to table 2.1. Particle types and energies are specified the radiation incident on the body or emitted from a source (for internal sources). Radiation weighting factors not listed in the table can be calculated as the mean radiation quality factor at 10 mm depth in an ICRU sphere [15].

Table 2.1: The radiation weighting factor w_R according to particle type and energy (adapted from [16]).

Particle type and energy	w_R
Photons, all energies	1
Electrons and muons, all energies (excluding Auger electrons emitted from nuclei bound to DNA)	1
Neutrons, <10 keV	5
10 keV to 100 keV	10
>100 keV to 2 MeV	20
>2 MeV to 20 MeV	10
>20 MeV (a continuous function is also available [16])	5
Protons, other than recoil protons, >2 MeV	5
Alpha particles, fission fragments, heavy nuclei	20

In this thesis the method of dose equivalents have been used. For a more extensive account of the biological effects of space radiation see e.g., [11] [17].

2.6.2 Heavy ions

As indicated by Table 2.1 (bottom row), particles with a high charge number are especially harmful to human tissue. This is reflected in Fig. 2.7, which shows the relative abundance of different GCR ion species compared to the resulting doses and dose equivalents. Iron only constitutes about 0.02% of the total GCR flux, but contributes more than 20% of the total GCR dose equivalent. The opposite is true for protons, which are only 92% abundant but contribute only 8% to the dose equivalent. The effect is due to much denser distributions of secondary charged particles around the heavy-ion trajectories in the tissue, and production of a multitude of secondary particles in nuclear reactions in the spacecraft hull.

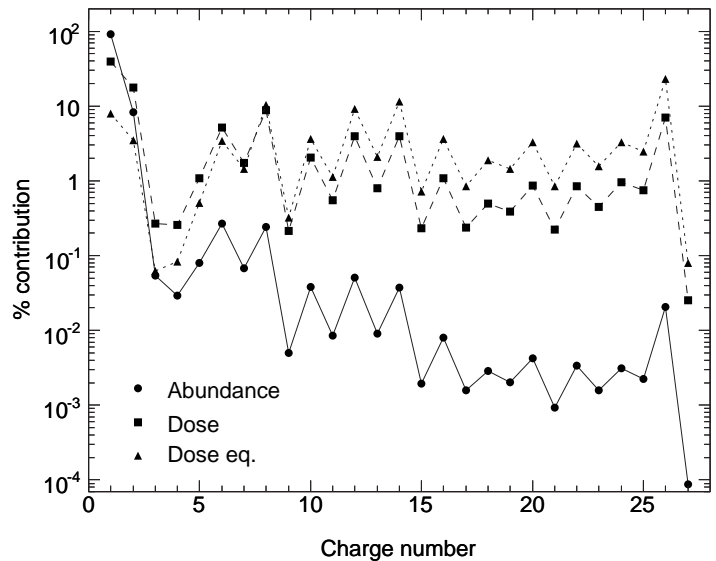


Figure 2.7: Contribution to fluence, dose and dose equivalent from the different ion species at solar minimum according to [18]. The lines are only intended to improve the clarity of the plot.

Chapter 3

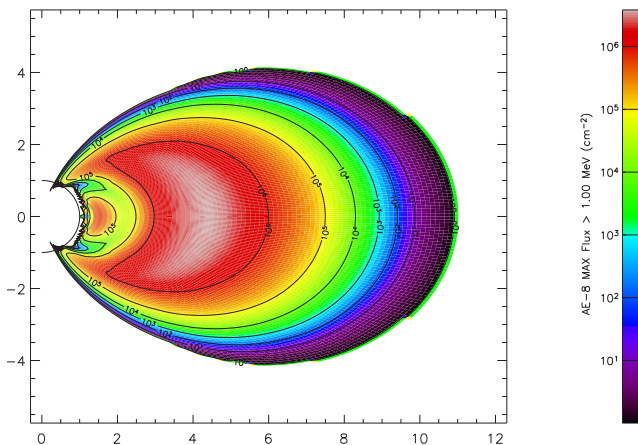
Models of the Low-Earth Orbit radiation environment

This chapter introduces model predictions of the radiation environment components found in the ISS orbit. The provided spectra are used for the full simulations of the radiation environment inside Columbus/ISS in chapter 7.

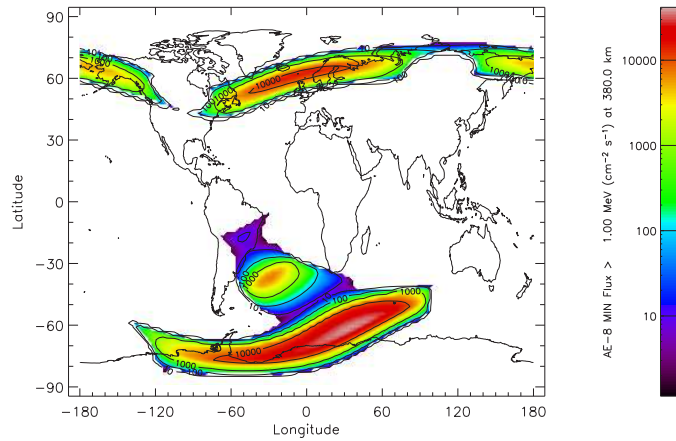
During the years, several models of the space radiation environment have been developed. Due to their complexity several web-interfaces such as SPENVIS [2], CREME96 [3] and Space Ionizing Radiation Environments and Shielding Tools (SIREST) [19] have been developed, from which it is possible to directly obtain e.g., orbit-averaged spectra. The ISS orbit is discussed in section 1.2. For the purpose of radiation simulations an altitude of 380 km has been used, unless otherwise noted. To demonstrate the effects of how the radiation environment depends on altitude, 330 km and 430 km have also been used.

3.1 Trapped electron belt models

While the trapped electron environment is unimportant for effects inside the ISS, it is an important part of the radiation environment in space. The NASA AE8 models [20] is the de facto standard model, and access is available through SPENVIS. An AE8 electron flux profile >1 MeV at solar minimum is shown in Fig. 3.1(a), demonstrating the presence of electrons in two distinct belts extending out to about 8 Earth radii. Fig. 3.1(b) shows the electron flux at 380 km superimposed on a world map. The existence of the SAA is evident. Furthermore, it is obvious that the trapped electron fluxes at high latitudes (the polar horns) increase.



(a) Trapped electron flux profile. The ordinate is aligned with the geomagnetic field and the half-circle represents Earth's surface, should the center of the geomagnetic field have been aligned with the center of the Earth. Units are in Earth radii.



(b) Trapped electron flux map at 380 km altitude. The polar horns and SAA are evident.

Figure 3.1: Trapped electron fluxes >1 MeV for the AE8 model at solar minimum.

3.2 Trapped proton belt models

There are several models of the trapped proton radiation environment available. Most of them are omni-directional models, meaning that they provide only the scalar integral of the flux over all directions (i.e., they provide no information on the anisotropy). The models of the trapped proton anisotropy in SPENVIS take AP8 omni-directional fluxes as input and reconstruct the anisotropy. Fig. 3.2 shows an AP8 model prediction of the trapped proton flux profile >50 MeV for solar minimum conditions, as well as the flux at 380 km superimposed on a world map.

3.2.1 Omni-directional models

Common omni-directional models include the NASA AP8 model [20], the PSB97 model [21] and the CRRESPRO model [22]. Orbit averaged spectra for all these models are available from SPENVIS. Additionally, AP8 spectra are also available from the CREME96 and SIREST websites. SIREST can provide spectra based on the AP8 model incorporating NOAAAPRO [23] data for arbitrary times in the solar cycle.

AP8

The NASA AP8 model is based on measurements by several spacecrafts during the 1960s-70s. It comes in two versions, one for solar minimum and one for solar maximum (AP8-MIN, AP8-MAX) and can predict the trapped proton spectra at all altitudes and orbital inclinations. This model is the de facto standard. However, it has been criticized for underestimating low-altitude high-energy fluxes, as well as for being based on very little data in the high-energy range [21]. Furthermore, at low altitudes the model is based on extrapolation [21].

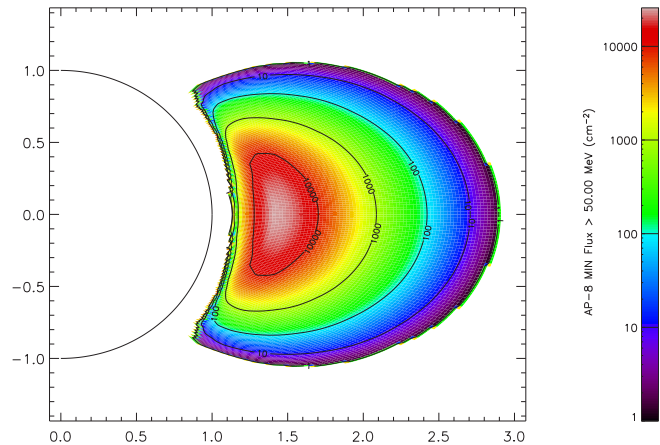
When assessing the error in the model [20] it is commented on that the usual quoted error is “about a factor of 2”. Furthermore, the greatest error is expected to be at locations of large spatial and energy gradients. This would be the case for high-energy protons at low altitudes.

PSB97

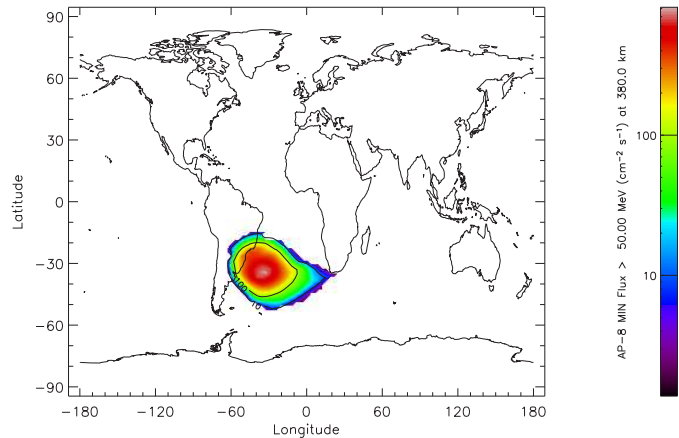
The PSB97 model [21] is based on data from the proton-electron telescope on the SAMPEX spacecraft during 1994–95. The model can predict spectra for orbits below about 600 km at solar minimum.

CRRESPRO

The CRRES spacecraft was flown in a low-inclination geosynchronous transfer orbit (350 km \times 33000 km) during solar maximum conditions in 1990–91. Data from the proton telescope on CRRES has been assembled into the CRRESPRO model [22] covering the proton energy range up to 100 MeV for orbits of any inclination at



(a) Trapped proton flux profile. The ordinate is aligned with the geomagnetic field and the half-circle represent Earth's surface, should the center of the geomagnetic field have been aligned with the center of the Earth. Units are in Earth radii.



(b) Trapped proton flux map at 380 km altitude. The SAA is easily recognizable.

Figure 3.2: Trapped proton fluxes >50 MeV for the AP8 model at solar minimum.

solar maximum. It is best applied to orbits above 1000 km altitude. Because of this, and the low high-energy limit of this model, it is unsuitable for calculations of the radiation fields inside ISS. However, it serves as an interesting illustration of the uncertainties associated with the current trapped proton models.

NOAAPRO

The NOAAPRO model [23] is based on data from the TIROS/NOAA spacecrafts. It predicts integral trapped proton fluxes in three energy bins (>16 MeV, >36 MeV and >80 MeV) for altitudes up to 850 km at arbitrary times in the solar cycle. As the model is not available outside the U.S., it has not been used for studies in the DESIRE project.

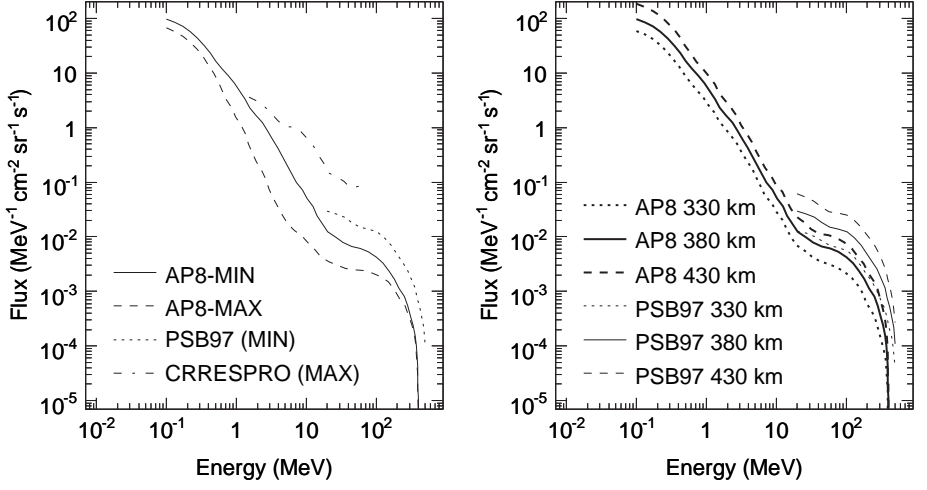
3.2.2 Comparisons of omni-directional trapped proton models

Kinetic energy spectra for the AP8, PSB97 and CRRESPRO models are shown in Fig. 3.3. Note that all spectra are plotted per solid angle, even though they are omni-directional. Spectra for the different models for an ISS orbit of 380 km altitude are compared in Fig. 3.3(a). The solar cycle dependence of trapped proton fluxes is illustrated in a comparison of the AP8-MIN and AP8-MAX models, where the solar maximum model predicts lower fluxes as anticipated. The PSB97 model extends the high-energy range of the AP8 models (400 MeV) to 500 MeV. At the same time it also predicts about a factor of three higher fluxes. Discrepancies between these models regarding increased high-energy protons fluxes have been noted previously, and are believed to result from lack of high-energy data when developing the AP8-MIN model [21]. Another argument for the deficit in AP8-MIN predictions of high-energy fluxes comes from the NOAAPRO model [23]. This model predicts about a factor of 2.5 higher integral fluxes (>80 MeV) as compared to AP8-MIN (and also to AP8-MAX). When comparing models based on data from different solar cycles it is important to keep in mind that the trapped proton flux depends on solar activity, which in its turn may exhibit cycle-to-cycle variations. The altitude limit of the CRRESPRO model renders it unsuitable for prediction of trapped proton fluxes at 380 km altitude. Comparing the CRRESPRO spectrum in Fig. 3.3(a) to the other models illustrates the difficulty in extrapolating data collected at one orbit to other orbits.

Fig. 3.3(b) indicates the altitude dependence of the AP8-MIN and PSB97 models. The trapped proton flux incident on ISS can vary by up to a factor of two, up or down, when deviating from the mean altitude by 50 km.

3.2.3 Models of the trapped proton anisotropy

None of the above models predict the anisotropy in the proton flux. The “Badhwar & Konradi 1990” model [24] (labeled UP in this thesis) available in SPENVIS provide anisotropic fluxes, given omni-directional AP8 model fluxes. Fig. 3.4(a)



(a) Comparison of models of orbit-averaged trapped proton spectra for 380 km altitude. Solar minimum (maximum) models are labeled with MIN (MAX).

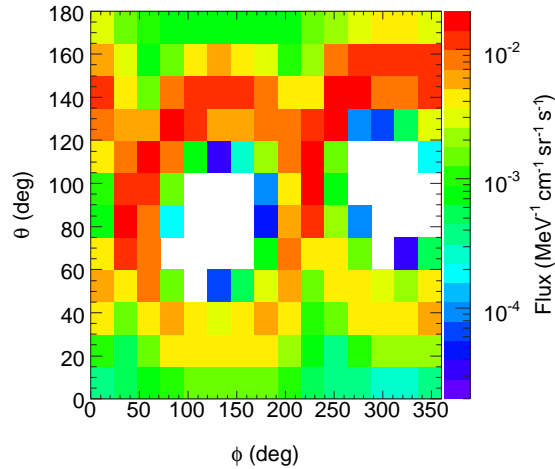
(b) Comparison of trapped proton fluxes at different altitudes for the AP8 and PSB97 models at solar minimum.

Figure 3.3: Kinetic energy spectra of incident trapped protons at ISS altitudes for different models.

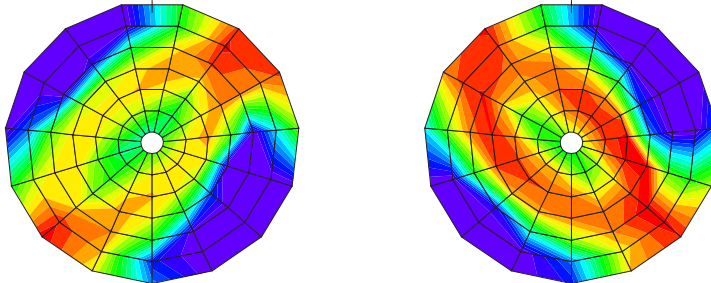
shows the ISS orbit averaged anisotropic trapped proton flux at 380 km altitude and 100 MeV as a function of the reversed primary particle direction in a coordinate system where the polar angle (θ) is measured from the velocity vector and the azimuthal angle (ϕ) from the zenith direction. Fig. 3.4(b) visualizes the flux coming from the forward hemisphere seen from the ISS orbit, facing the direction of the velocity and with the head pointing towards zenith. Fig. 3.4(c) visualizes the flux for the aft hemisphere. It is clear that for optimal use of shielding mass for protection from trapped protons, an anisotropic shielding distribution matching that of the trapped proton flux would be advantageous.

3.3 The GCR environment

Two commonly used models of the GCR environment are the Nymmik model [25] (implemented in CREME96 and thus labeled) and the Badhwar-O'Neill model [26] (implemented in SIREST and thus labeled). Orbit-averaged model predictions for GCR protons for an ISS altitude of 380 km are shown in Fig. 3.5. The SIREST model does not, in contrast to the CREME96 model, automatically take the Earth's



(a) All angles. The white areas are bins with exactly zero particles $\text{MeV}^{-1} \text{cm}^{-1} \text{sr}^{-1} \text{s}^{-1}$.



(b) Polar plot of the data in (a) for $\theta \in [0, 90]$ (i.e., the forward directions).

(c) Polar plot of the data in (a) for $\theta \in [90, 180]$ (i.e., the aft directions).

Figure 3.4: Incident anisotropic trapped proton angle and kinetic energy differential spectrum for an ISS orbit at 380 km altitude at 100 MeV according to the AP8-MIN based UP-MIN model. The flux is plotted by the reversed primary particle direction in a coordinate system where the polar angle (θ) is measured from the velocity vector and the azimuthal angle (ϕ) from the zenith direction.

shadow into account. All SIREST based GCR spectra have been adjusted for this. SIREST predicts about a factor of three greater GCR peak proton fluxes than CREME96 for both solar cycle extremes. The reason for this discrepancy between the models is unclear, but could be partly due to the use of different geomagnetic transmission functions [27].

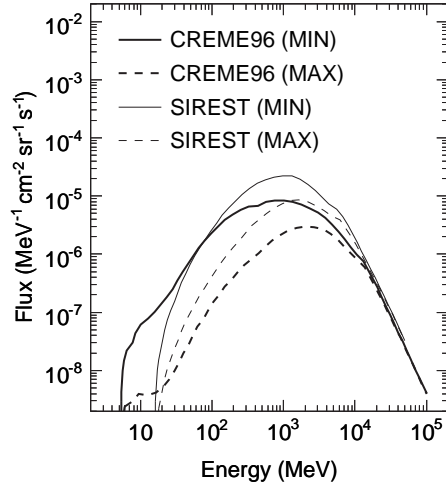


Figure 3.5: Comparison of models of orbit-averaged GCR proton kinetic energy spectra for 380 km altitude. Solar minimum (maximum) models labeled with MIN (MAX).

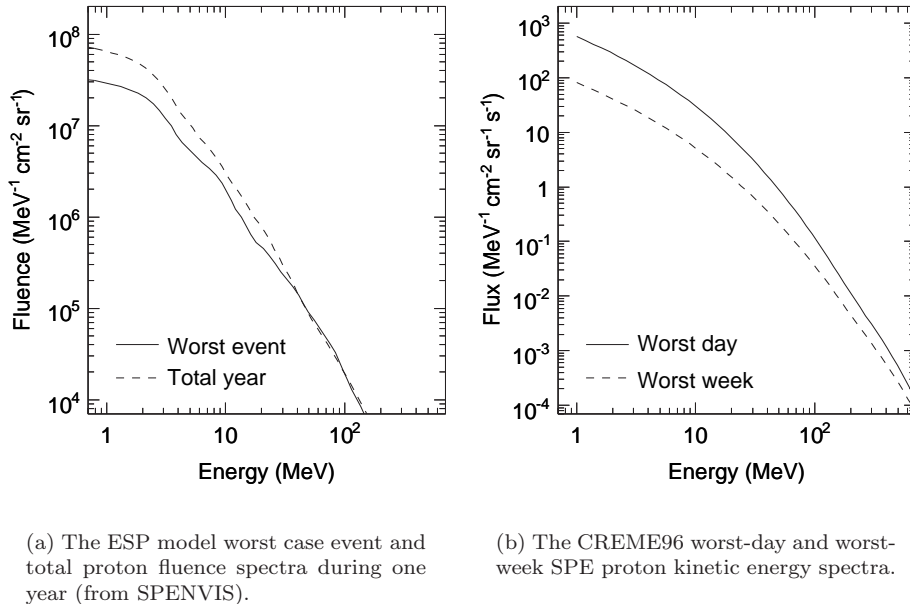
In addition to protons, the GCR environment also consists of ions. See section 2.6 for a description of ion abundances. Ions have a spectral shape similar to that of protons, but are shifted to lower fluxes.

3.4 Solar event particles

Parameterizations of historical SPEs are available in [28]. In general the solar event particle flux is stochastic and has to be treated statistically. Commonly used models available in SPENVIS include the King [29] and JPL-91 [30] models. Given a confidence level and offset from solar maximum, these models can provide spectra of the proton fluence for a selected duration for different confidence levels. As such, these models are suitable for studies of total effects during a time in the order of years (SPENVIS limits the use of the models to at least one year). Another set of models are the ESP models [31] [32] which, while they can provide the same type of fluences as the King and JPL-91 models, they can also provide a worst-case event fluence during the selected duration. A kinetic energy spectrum for a worst case event proton fluence during one year for a confidence level of 95% according to the

ESP model is shown in Fig. 3.6(a). A prediction of a total proton fluence during one year for a confidence level of 95% is also shown. Additionally, CREME96 can provide “worst-day” and “worst-week” spectra based on the 1989 SPE. CREME96-based worst-day and worst-week spectra for a 380 km altitude ISS orbit and stormy magnetic conditions are shown in Fig. 3.6(b).

Both SPENVIS and CREME96 provide spectra properly attenuated by the geomagnetic field. A choice can be made between “quiet” and “stormy” conditions. SPEs are usually (but not always) associated with so-called magnetic storms on Earth, which facilitate the penetration of solar particles deep inside the magnetosphere. The spectra shown in Fig. 3.6 have been calculated according to a disturbed magnetosphere.



(a) The ESP model worst case event and total proton fluence spectra during one year (from SPENVIS).
(b) The CREME96 worst-day and worst-week SPE proton kinetic energy spectra.

Figure 3.6: Kinetic energy spectra of incident SPE protons for an ISS altitude of 380 km altitude and disturbed magnetosphere according to ESP and CREME96 SPE models.

3.5 Cosmic ray albedo neutrons

A 380 km altitude orbit-averaged ISS cosmic ray albedo neutron spectrum from SIREST is shown in Fig. 3.7. The model providing this spectrum is not documented in SIREST, but the general shape of the spectrum is in line with the models described in [33] [34]. In these models one experimental spectrum measured at

the top of the atmosphere is scaled to different altitudes, geomagnetic cut-offs and solar cycle times. The dependence on geomagnetic cutoffs and times in the solar cycle is taken into account by fits to experimental integral neutron fluxes in the 1–10 MeV energy region. Such measurements have been made over the full range of geomagnetic cut-offs for different times in the solar cycle. The time in the solar cycle is parameterized as a function of ground-based neutron monitor data or of SSN data. To extrapolate the model into space it is assumed that the flux decreases as the inverse of the radial distance squared. The spectra returned by SIREST however seem to be independent of time in the solar cycle. Nevertheless, due to lack of other easily accessible orbit averaged cosmic ray albedo neutron model sources, this spectrum has been used for studies within the DESIRE project.

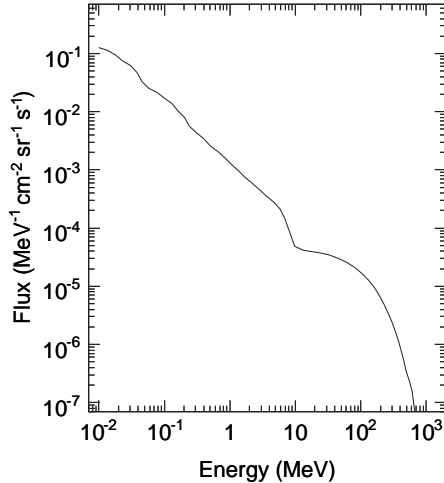


Figure 3.7: The cosmic ray albedo neutron kinetic energy spectrum for a 380 km altitude ISS orbit according to SIREST.

3.6 Angular distribution of primary particles

The trapped proton environment in the ISS orbit is anisotropic, and will be evaluated with both omni-directional models and anisotropic models. In the omni-directional version the primary particles are assumed to be distributed isotropically. However, also the other radiation environment components are to an extent anisotropic.

The charged particles of the GCR and SPE environment are influenced anisotropically by the Earth's magnetic field. The effect is decreasing with increasing particle energy and have been ignored in this thesis. However, assuming all particles travel in straight lines, no particles can come out of the solid angle obstructed by the Earth. The reverse situation is true for cosmic ray albedo neutrons.

The relative solid angle is about 33.5% at 380 km altitude and varies with $\pm 1\%$ at 330 km and 430 km altitudes. Unless otherwise noted, all spectra discussed in this thesis are solid angle averaged omni-directional spectra (i.e., omni-directional spectra divided by 4π). This means in the case of e.g., Figs 3.5 and 3.6 that the flux from solid angles not obstructed by the Earth is greater than the (average) flux shown in the figures.

Chapter 4

Geant4

This chapter discusses the Geant4 Monte Carlo particle transport toolkit in the context of the DESIRE project. A short description of the main physics models in Geant4 used for the results in this thesis is offered.

Geant4 [4] [5] is a well established general purpose Monte Carlo particle transport toolkit that is being developed by a large international collaboration including ESA, CERN, and many other institutes and universities. It is the latest incarnation in the Geant-series of particle transport tools emanating from the high-energy physics community around CERN. The previous Geant3 tool [35] enjoyed a long and successful use by e.g., the Large Electron-Positron Collider (LEP) experiments at CERN. The applications of Geant4 range from space physics to high-energy physics, to medical physics. The name Geant4 stands for “GEometry ANd Tracking”, two cornerstones of a detailed radiation transport calculation. In addition to be able to follow individual particles in an advanced 3-D geometry, it is of course also necessary to calculate their interaction probabilities with the constituent atoms and nuclei in the geometry medium. Facilities for handling detector responses and evaluation of simulation properties such as total deposited energy is available, as well as visualization and user interfaces.

At present, some commonly used particle transport programs for manned space applications (such as the NASA BRYNTRN [36] and HZETRN codes [28]) are not Monte Carlo based. Instead, they solve 1-D Boltzmann transport equations that describe how radiation fields are transformed when passing through a given mass thickness. This approach is much faster computationally than Monte Carlo based solutions, but requires several additional approximations. Particle fluxes and dose rates can in this case be calculated for a location in an ISS 3-D geometry by evaluating the individual contributions from different directions [37]. On the Russian side the Monte Carlo program SHIELD [38] has been used for calculations of parts of the ISS radiation environment [39].

4.1 General properties of Geant4

The general term “Monte Carlo method” refers to the solution of a numerical problem using probability statistics and random numbers. In the case of Geant4 this method is used to let different possible particle interactions with different interaction probabilities compete against each other to determine how far a particle can travel in a heterogeneous material before an interaction occurs. The traveled distance is called a “step”. Since some types of interactions occur very frequently these are condensed into “continuous” processes in order to prevent them from imposing considerable limitations on the scope of possible applications within given computational resources. Such processes continuously modify the particle energy, and thus the cross-section, during a step. Therefore a limitation on the step size has to be introduced. The limit has to be small enough for all relevant cross-sections to be approximately constant during the step, but not so small that computation time is greatly increased.

The geometry in which particles are propagating in Geant4 is constructed by placing Constructive Solid Geometry (CSG) geometry primitives, such as boxes or cylinders, with associated material information and geometry transformations inside each other. The result is a geometry tree originating from a “world”-volume. The geometry primitives can be combined with Boolean operations. In addition to CSG primitives, geometries constructed from their boundary surfaces can also be used. Logical movement of a particle in the simulation from one volume to another requires evaluation of if the particle trajectory intersects another volume; a computationally expensive operation if done naively. In general, various optimization techniques are used. Geant4 uses a voxelization algorithm which allows it to perform well, even with a flat (i.e., non-hierarchical) geometry tree. This is in contrast to other particle transport tools, e.g., Geant3.

Design requirement of Geant4 include maintainability during the approximately 20 years of Large Hadron Collider (LHC) operation at CERN, as well as transparency of the physics implementation to allow for end-user validation. This has led to an object oriented code implementation using the C++ programming language and a well designed API.

4.2 Geant4 physics models

To allow for maximum flexibility, Geant4 lets the user make a selection of models of particle interactions relevant for the simulation scenario. This physics configuration is done in the C++ code of a users application (called a “physics list”). There, processes can be assigned to particles and models to processes until all relevant interactions for all relevant particles in a simulation have been defined. This approach allows for e.g., multiple models of an interaction to exist in Geant4 and for being easily replaceable in user code depending on the desired application.

Within the DESIRE project different configurations of the hadronic physics have been used, while electromagnetic interactions have in all cases been treated with the “standard” electromagnetic process. In the case of hadronic interactions, the physics configuration can be highly complex. Therefore physics lists suitable for the various types of simulation scenarios are distributed together with Geant4. The physics lists used for the studies presented in this thesis are (labels used in this thesis in parenthesis): LHEP_BERT_HP (G4BERT), LHEP_BIC_HP¹ (G4BIC), LHEP_LEAD_HP (G4LEAD) and LHEP_PRECO_HP (G4LEPPC).

The first part of the physics list names (LHEP) stands for Low- and High-Energy Parameterized model. It is the same for all four physics lists and refers to the model of high-energy hadronic interactions, typically used from 5 or 10 GeV and up. The second part of the name refers to intermediate energy hadronic interactions. The underlying model of the LHEP_BERT_HP physics list is the Bertini Cascade model [40], which covers energies up to a 10 GeV. Low energy coverage of the model is provided by its own implementation of a pre-equilibrium decay model for energies below the cascade regime. The same is true for the Binary Cascade model [41] used in the LHEP_BIC_HP physics list, though it uses the native Geant4 pre-compound model [4] at low-energies, where the cascade model can not work. The LHEP_LEAD_HP physics list uses the G4Mars5GeV model, a partial rewrite of the MARS code system [42] in Geant4. In the LHEP_PRECO_HP physics list, no proper intermediate energy hadronic interaction model is used. Instead the LHEP model is used down to 170 MeV, where the Geant4 pre-compound model takes over. The last part of the physics list names refers to the use of data driven High-Precision low-energy neutron models used below 20 MeV. All of these models are discussed in more detail in section 4.2.2.

4.2.1 Electromagnetic interaction models

The physics lists used for simulations in the DESIRE project make use of the standard Geant4 electromagnetic physics processes described in [4] and [43], in contrast to the set of electromagnetic physics processes engineered specifically for low-energy applications in Geant4. Models of the photo effect, Compton effect and pair production discrete processes are used for photons. Electrons interact via the discrete bremsstrahlung process and continuous multiple Coulomb scattering and ionization processes. Positrons are associated with the same kinds of processes, as well as the discrete annihilation process. Charged hadrons and ions interact according to models of multiple Coulomb scattering and ionization. The ionization process also simulates straggling effects and the discrete emission of δ -rays (and if applicable, Möller and Bhabha scattering processes).

¹Prior to the availability of a native LHEP_BIC_HP physics list, an equivalent physics list based on the LHEP_BIC physics list with added data driven low-energy neutron transport process was used. The modified physics list was used for the studies in chapter 5 while the native physics list was used for the studies in chapter 7.

4.2.2 Hadronic interaction models

This section is based on information from [4] and [43], as well as general information from [44].

Parameterization Driven models (LHEP)

The Geant4 parameterized models are based on the Geant3 GHEISHA package [45] and include fission, capture, inelastic and elastic scattering processes. The energy regimes of the models extend up to 25 GeV for the low-energy version, and from 10-20 GeV up to 10 TeV for the high-energy version. The assumptions of the parameterized model do not hold in the sub-GeV energy regime [43]. Nevertheless, the model was used for benchmarking studies of Geant4 in the beginning of the DESIRE project since no other model was available at that time.

Leading particle biased model (LEAD)

G4Mars5GeV is a partial rewrite of the MARS code system [42] in Geant4. MARS is a fast Monte Carlo program, which uses an inclusive approach to multi-particle reactions and thus generates only a fixed number of statistically weighted secondaries per reaction. It is suggested for energies up to 5 GeV [46]. It was released in Geant4 prior to the availability of the cascade models, when only the Parameterization Driven models were available. At that time, it was an interesting addition to Geant4 due to the discrepancy between experimental data and LHEP-based simulations.

Intra-Nuclear Cascade models (BERT, BIC) and lower energy models

The general foundation of an Intra-Nuclear Cascade (INC) model is that the wavelength of a projectile incident on a nucleus is shorter than the average distance between the constituent nucleons, and also shorter than the mean free path inside the nucleus. For projectile energies which fulfil this, particle-nuclei reactions can be viewed as a sequence of particle-nucleon reactions. The resulting reaction tree is a cascade of particles inside the nucleus, thus the name. The limitation on the minimum incident particle energy according to the criteria above is estimated [44] to be roughly about 1 GeV and 200 MeV, respectively. This severely limits the applicability of the model, especially since any secondary particles created in the cascade would also have to obey these restrictions. The impact of the limitations is reduced due to most of the reactions taking place close to the surface of the nucleus, where the density is lower (longer mean-free paths). Additionally, Pauli-blocking of secondary particles can occur, limiting the creation of low-energy particles. In practice, INC models are used for particle energies down to about a hundred MeV.

Two INC models are available in Geant4: the Bertini Cascade model [40] (BERT) and the Binary Cascade model [41] (BIC). In general the Geant4 INC models propagate particles inside a nuclear model. The model used differs for

the BERT and BIC models. In the BERT model the nucleus is described with three concentric spherical regions, approximating the nuclear matter density distribution and Fermi energy. The BIC model is based on a more advanced 3-D model of the nucleus containing individual nucleons, making it an Intra-Nuclear Cascade-Quantum Molecular Dynamics model hybrid. Here each nucleon has its own Fermi momentum. At the beginning of a reaction an impact parameter selection is made, and an initial interaction point is determined. If the projectile crosses the nucleus without interacting, a new selection is made. Interactions are then calculated between cascade particles and nucleons, or the nuclear medium, according to free-space cross sections modified with respect to Fermi motion. The nuclear potential is taken into account. Reactions generating secondaries violating the Pauli principle (i.e., if the secondary particle has a momentum below the local Fermi momentum) are suppressed. The cascade progresses until various limitations on remaining energy in the nucleus is reached.

Modeling of the remaining nucleus after the cascade, is done according to the sequence of pre-equilibrium calculations, evaporation/break-up and final nucleus de-excitation. The BERT model contains its own implementations of these models, while the BIC model uses the default Geant4 implementations described below.

At the end of the cascade, several cascade particles are in general still propagating through the nucleus. These are pre-dominantly of a lower energy than what is suitable according to INC assumptions. The nucleus is therefore handed over to the pre-compound model [43], which provides an exciton-based statistical model of the emission of nucleons and fragments. At the end of this stage the remaining excitation energy is shared by a large number of nucleons. Nucleons and light fragments can “evaporate” from the nucleus at this stage, or the nucleus might undergo fission. The remaining nucleus is then de-excited by emission of gamma-rays.

Ion-nuclei interactions

While not yet used for studies within the DESIRE project, the recent availability of Geant4-models of ion-nuclei interactions deserves to be noted. An extension of the Binary Cascade model, originally developed for light ions only, has proved to reproduce features of secondary particle spectra also in heavy ion interactions. The model works by propagating the incident nucleons through the target nucleus one at a time, while keeping track of the state of the “wounded” nucleus. As such, it is reasonable to expect it to fail for heavier ions where interactions between projectile nucleons become more relevant. However, preliminary studies for e.g., Iron-Aluminum reactions [47] indicates a performance comparable to the competing Monte Carlo tools Fluka [48] and Phits [49]. A tentative upper energy-limit for this model is currently given as 10 GeV/nuc [46]. Additionally, an abrasion-ablation model has recently been implemented in Geant4 [50]. The abrasion part of the model is, in contrast to the individual nucleon-nucleon interactions of the cascade models, based on geometric considerations, where the nucleons in the overlapping parts of the nuclei get abraded. The residual pre-fragments are then de-excited

by detailed statistical processes or by an ablation-type process. The model offers a better description of fragment yields from ion-nuclei reactions than the Binary Cascade based model [41]. Another possibility for treating ion-nuclei reactions using Geant4 is through an interface [51] to the JQMD code [52].

Low-energy neutron interactions

Geant4 provides a high-precision data-driven description of low-energy neutron interactions from thermal kinetic energies up to about 20 MeV. Radiative capture, elastic scattering, fission and inelastic scattering are considered according to cross-section data from several evaluated neutron data libraries [4]. In case information on a specific element is not available, parameterized models [43] are used instead of the high-precision models.

Chapter 5

Tests and validation studies of Geant4

This chapter is based on the paper “Status of the DESIRE Project: Geant4 Physics Validation Studies and First Results From Columbus/ISS Radiation Simulations” by the author [7]. Those results are here complemented by an evaluation of the performance of the Geant4 physics models with several additional target materials and sizes, as well as results from simulations using the LHEP_BERT_HP physics list. Earlier results, reflecting the performance of Geant4 prior to the release of the cascade models, are available in [53].

Geant4 has previously not been used for evaluation of radiation risks for astronauts, so it is important to verify that it models the relevant physics correctly. Electromagnetic interactions are better understood and modeled than nuclear interactions in simulation software. The validation efforts have thus been concentrated on the hadronic reactions. Secondary neutrons from such reactions escape the target easily, in contrast to protons and charged fragments, and are thus suitable for probing effects of such reactions. For comparisons of Geant4 electromagnetic physics models, see e.g., [4] [54] [55].

Results are presented on comparisons to experimental data, the SHIELD-HIT Monte Carlo code [38] [56] and the BRYNTRN code [36]. The comparisons to the codes are motivated by the fact that they have been extensively used for studies of space radiation effects in the past. In each comparison four Geant4 models of inelastic nucleon interactions have been studied. These are denoted G4BERT, G4BIC, G4LEAD and G4LEPPC, respectively and are described in section 4.2. Geant4 version 6.1 (released 25 March 2004) has been used for the validation against experimental data (section 5.1) and Geant4 version 5.2+p02 (released 3 October 2003) has been used for the comparison against BRYNTRN and SHIELD (sections 5.2 and 5.3).

5.1 Validation by comparison to Los Alamos experimental data

In the experiments described in [57] and [58] the spectra of neutrons leaving extended targets irradiated by 113 MeV and 256 MeV protons were studied. The experiments included measurements of the neutron distribution at multiple angles and for multiple target materials.

Since the main material used for the construction of the space station is aluminum it is especially important to verify the correctness of radiation transport in this material. Fig. 5.1 shows the neutron yield in different directions from an aluminum cylinder irradiated by 113 MeV protons. Angles are measured from the target cylinder axis, starting at 0° in the beam direction. The G4BIC, G4BERT and G4LEPPC models perform well in this case, showing a miss-estimation of the neutron yield by at most a factor of two except for the highest neutron energies and a few isolated energy points. The G4LEAD model reproduces the neutron yields quite well at high energies but is lacking an order of magnitude in the yield at lower energies. Neutron yields at 256 MeV are shown in Fig. 5.2. G4BIC performs well also at this energy, while G4LEAD has only some agreement with the data for high-energy neutrons (>30 MeV) in the forward directions ($30^\circ, 60^\circ$). For G4LEPPC the primary proton reactions are outside the energy regime of the pre-equilibrium model and the behavior is thus a lot worse than at the lower energy. The parameterized model does not take double-differential cross-sections into account, resulting in an isotropic neutron yield (slightly peaked in the forward direction due to the momentum of the primary proton). This is incorrect and the discrepancies in the fluences ranges all the way up to two orders of magnitude in the case of the high-energy neutron fluence in the backward direction (150°).

Comparisons for other target materials (beryllium, carbon, iron, uranium) and sizes have also been performed. These show model dependent behavior similar to that seen for aluminum. The G4BIC and G4BERT models agrees well with data in all performed studies, see Figs. 5.3–5.13. The errors in the experimental data are comparable to the size of the markers in the plots.

5.2 Comparisons to SHIELD-HIT

The SHIELD Monte Carlo code [38] has been used for particle transport calculations since the past 30 years. Its results are found to be in good agreement with experimental data for various phenomena studied, including space radiation shielding applications. SHIELD-HIT [56] is a recent improvement of SHIELD, that extends the transport of hadron cascades from standard targets to that of ions in arbitrary tissue-like materials, taking into account ionization, energy-loss straggling and multiple Coulomb scattering effects.

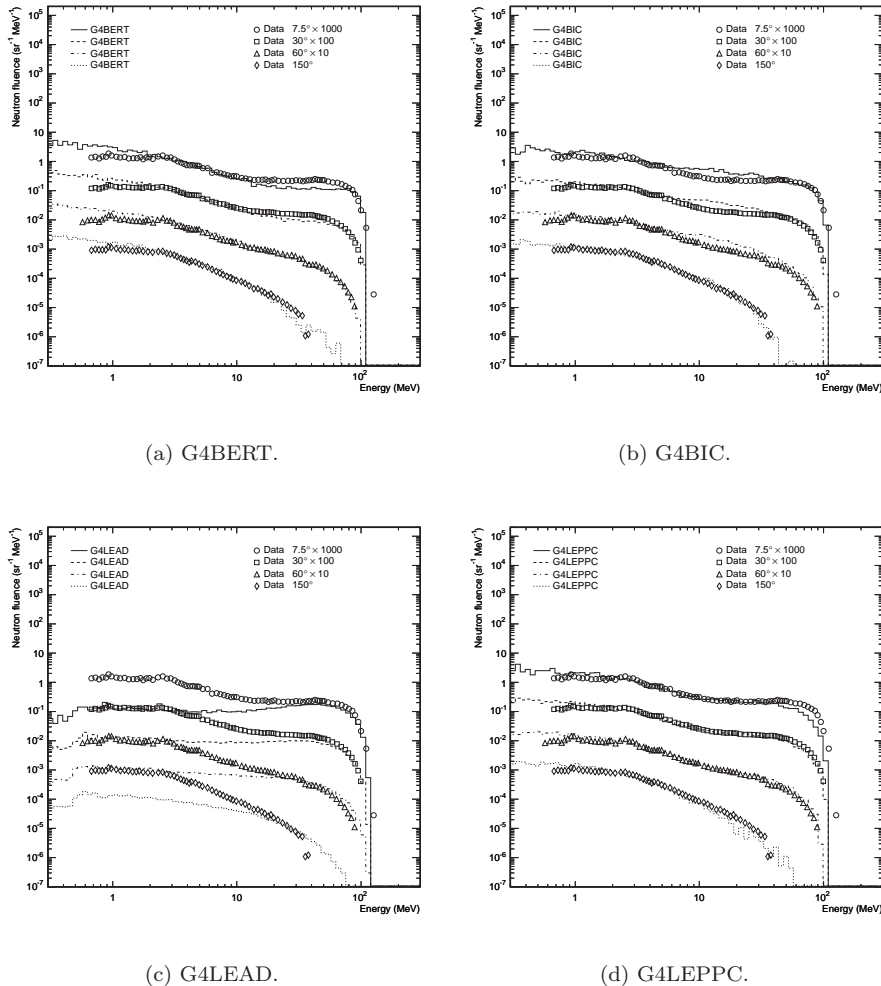


Figure 5.1: Directional neutron spectra comparisons. 113 MeV protons incident on stopping length aluminum target cylinder (radius 3.65 cm, length 4.03 cm). The data for the different angles have been separated using the indicated scale factors.

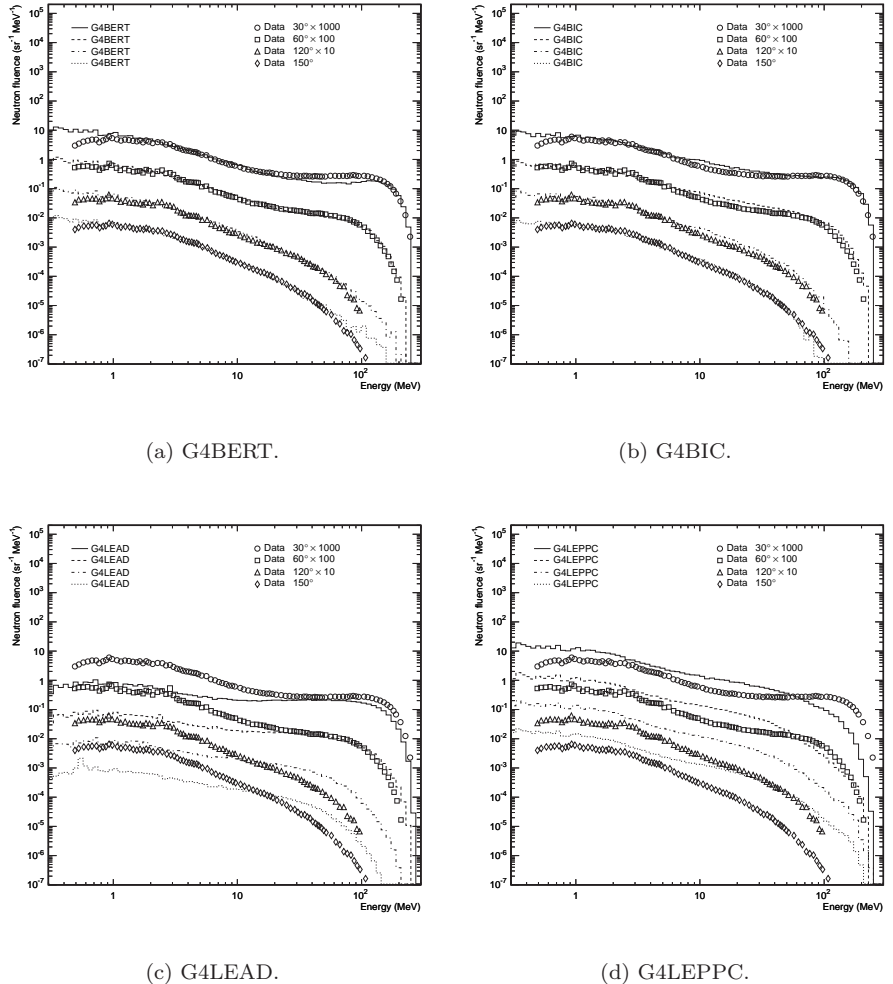


Figure 5.2: Directional neutron spectra comparisons. 256 MeV protons incident on near stopping length aluminum target cylinder (radius 8.00 cm, length 12.15 cm). The data for the different angles have been separated using the indicated scale factors.

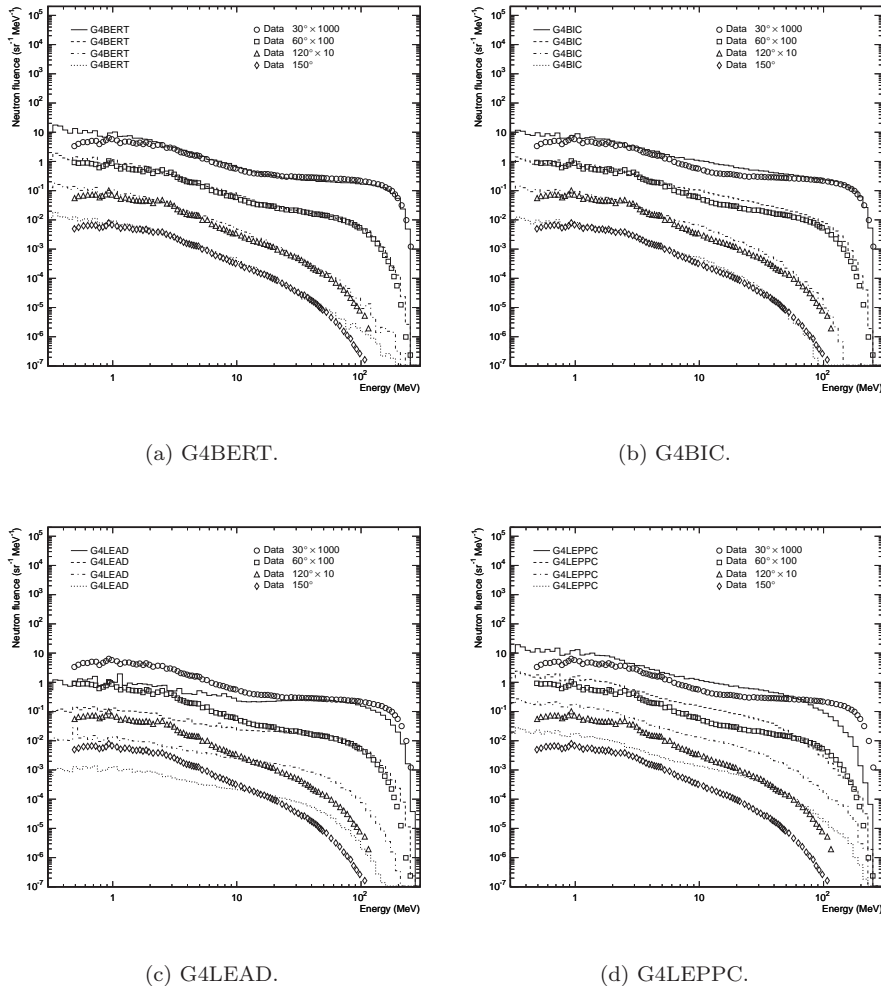


Figure 5.3: Directional neutron spectra comparisons. 256 MeV protons incident on stopping length aluminum target cylinder (radius 8.00 cm, length 20.0 cm). The data for the different angles have been separated using the indicated scale factors.

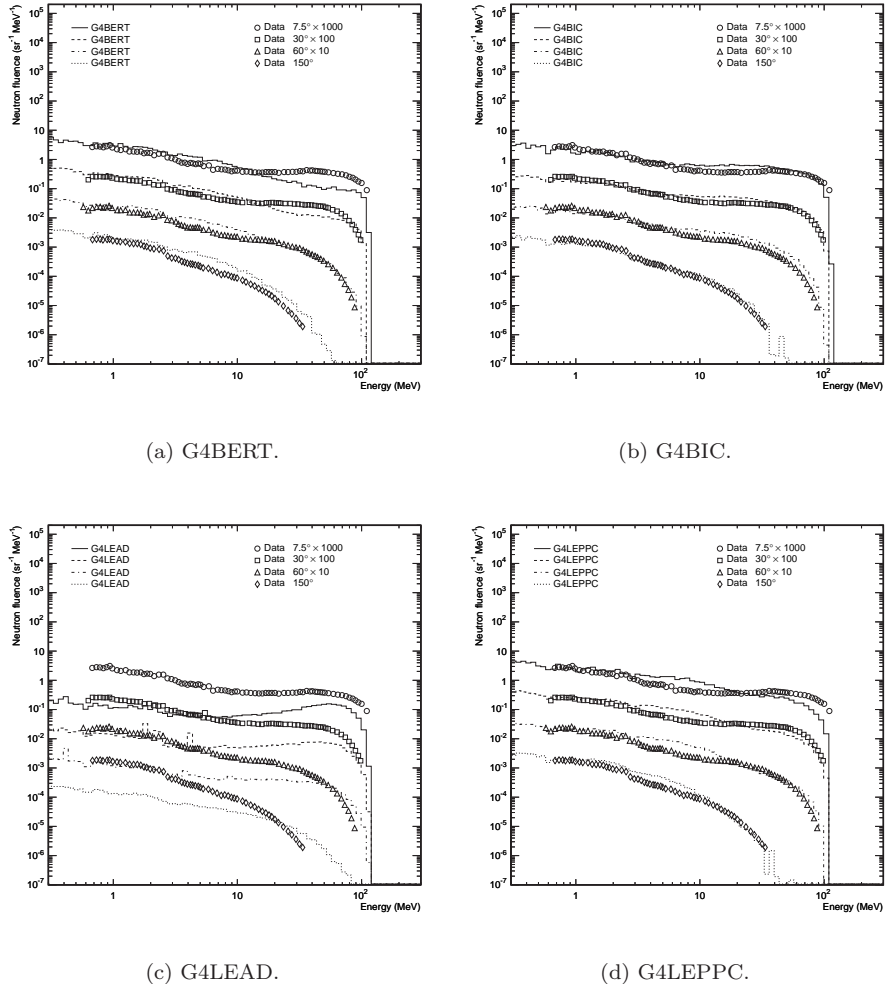


Figure 5.4: Directional neutron spectra comparisons. 113 MeV protons incident on stopping length beryllium target cylinder (radius 3.65 cm, length 5.70 cm). The data for the different angles have been separated using the indicated scale factors.

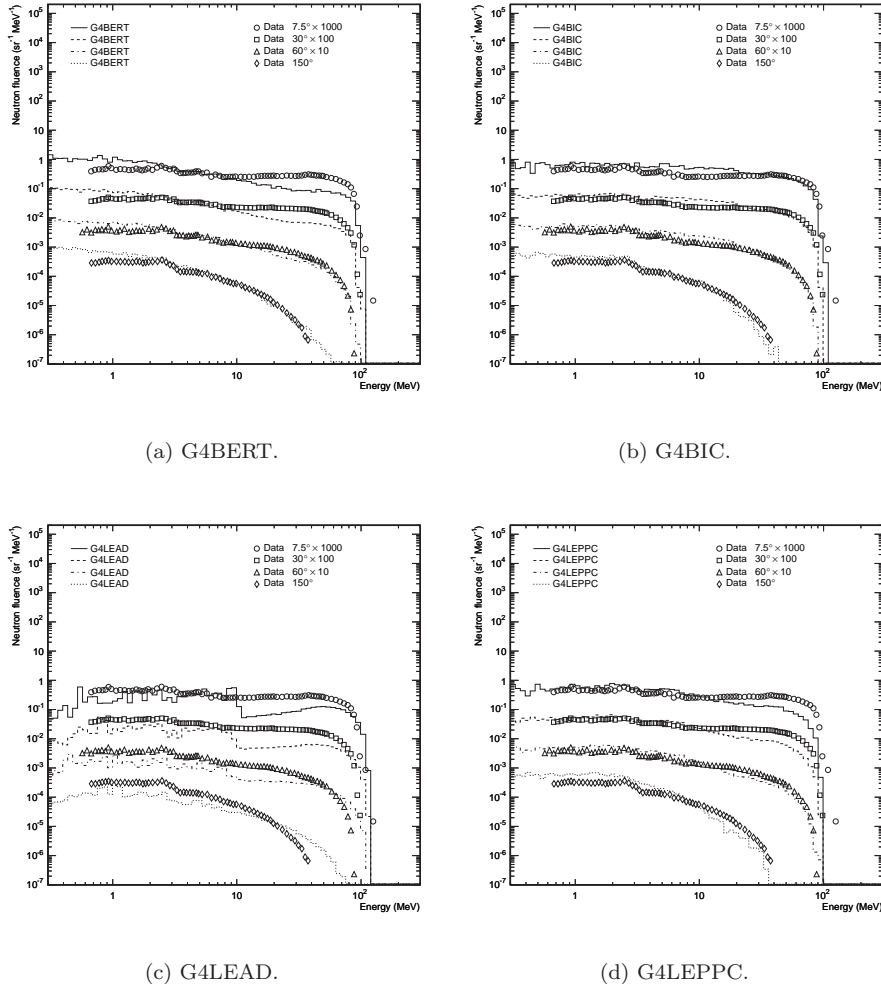


Figure 5.5: Directional neutron spectra comparisons. 113 MeV protons incident on stopping length carbon target cylinder (radius 3.65 cm, length 5.83 cm). The data for the different angles have been separated using the indicated scale factors.

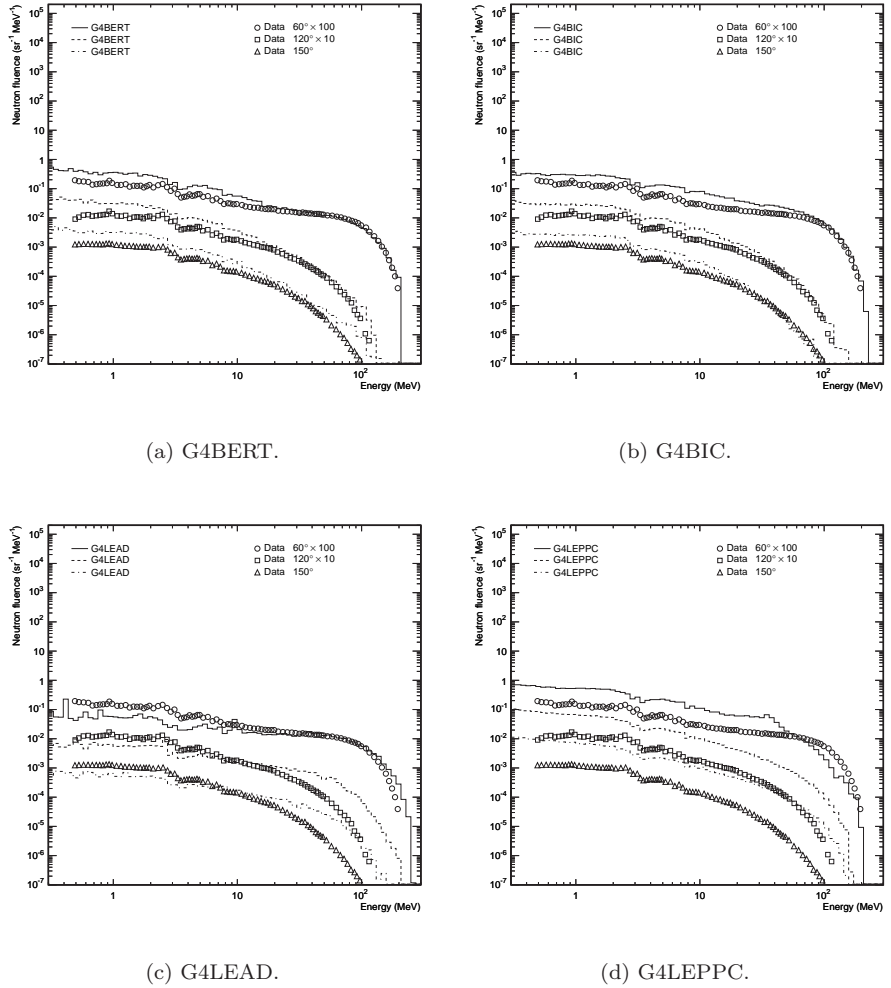


Figure 5.6: Directional neutron spectra comparisons. 256 MeV protons incident on near stopping length carbon target cylinder (radius 8.00 cm, length 17.45 cm). The data for the different angles have been separated using the indicated scale factors.

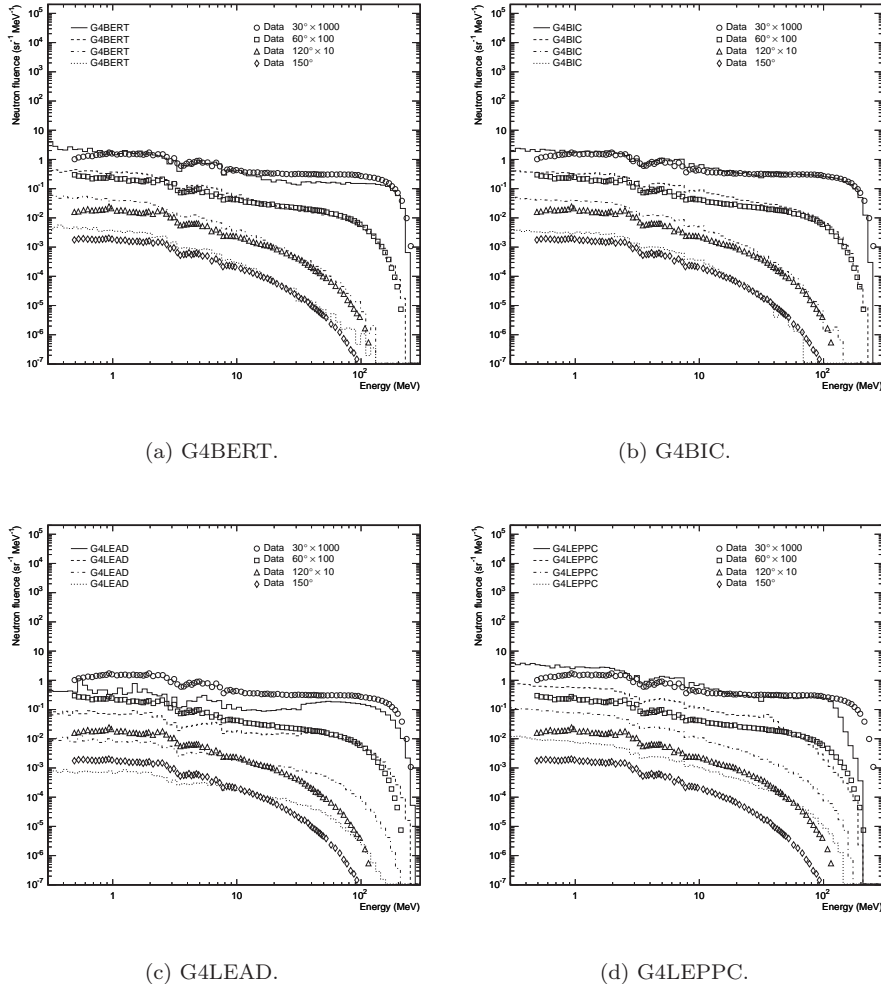


Figure 5.7: Directional neutron spectra comparisons. 256 MeV protons incident on stopping length carbon target cylinder (radius 8.00 cm, length 30.0 cm). The data for the different angles have been separated using the indicated scale factors.

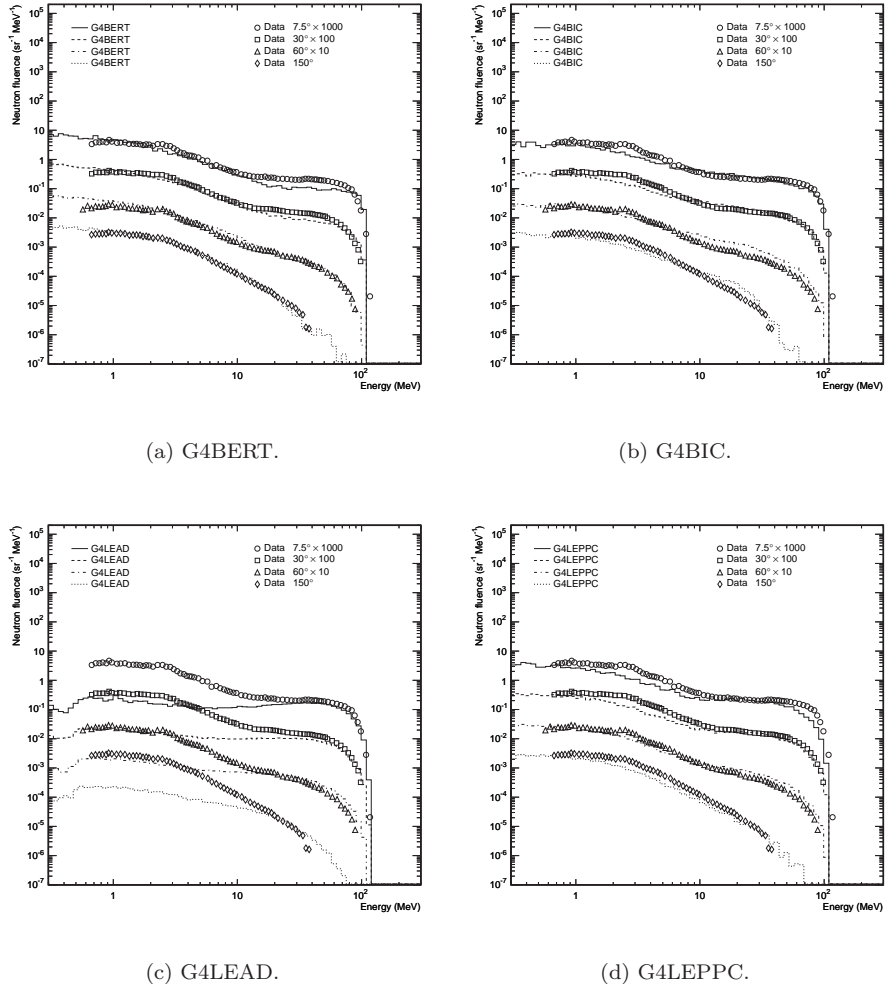


Figure 5.8: Directional neutron spectra comparisons. 113 MeV protons incident on stopping length iron target cylinder (radius 3.65 cm, length 1.57 cm). The data for the different angles have been separated using the indicated scale factors.

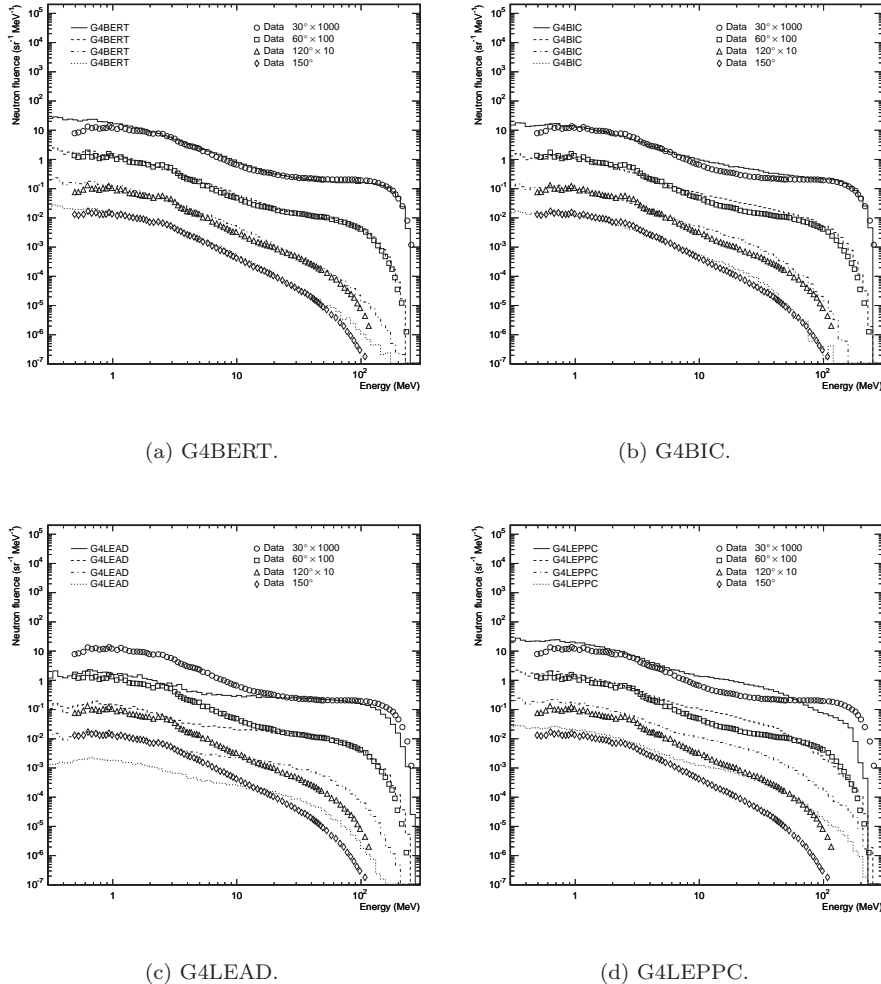


Figure 5.9: Directional neutron spectra comparisons. 256 MeV protons incident on near stopping length iron target cylinder (radius 8.00 cm, length 4.70 cm). The data for the different angles have been separated using the indicated scale factors.

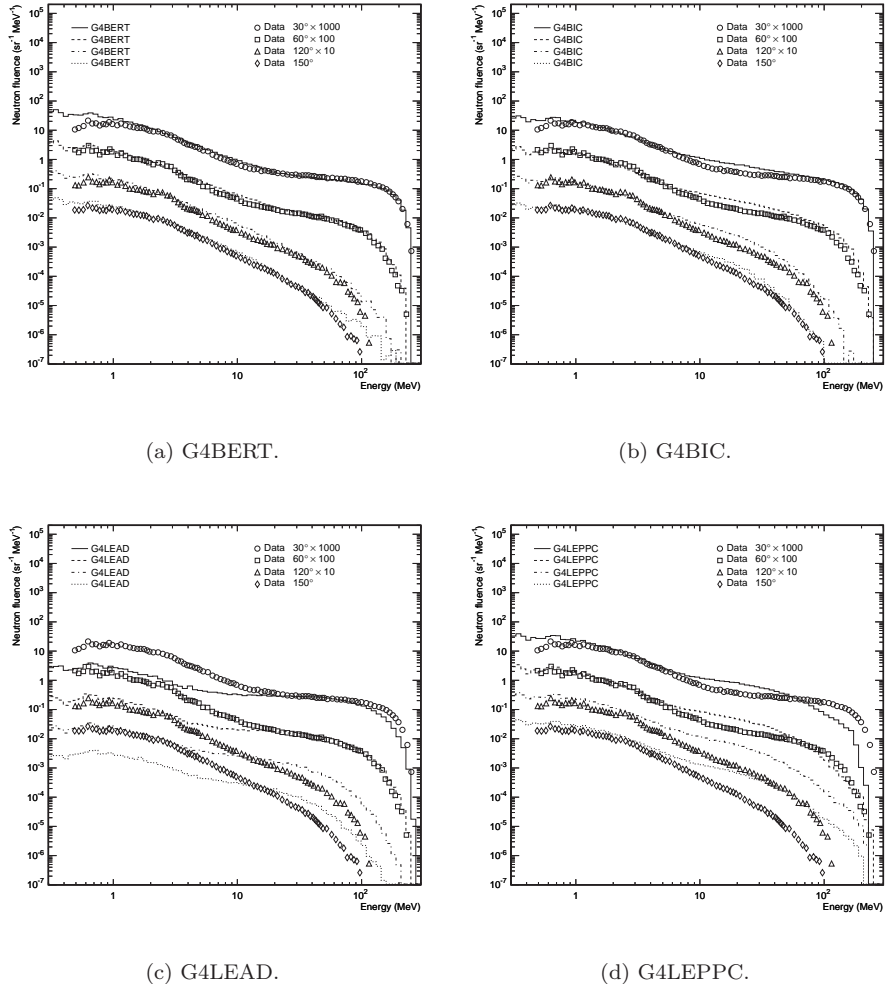


Figure 5.10: Directional neutron spectra comparisons. 256 MeV protons incident on stopping length iron target cylinder (radius 8.00 cm, length 8.00 cm). The data for the different angles have been separated using the indicated scale factors.

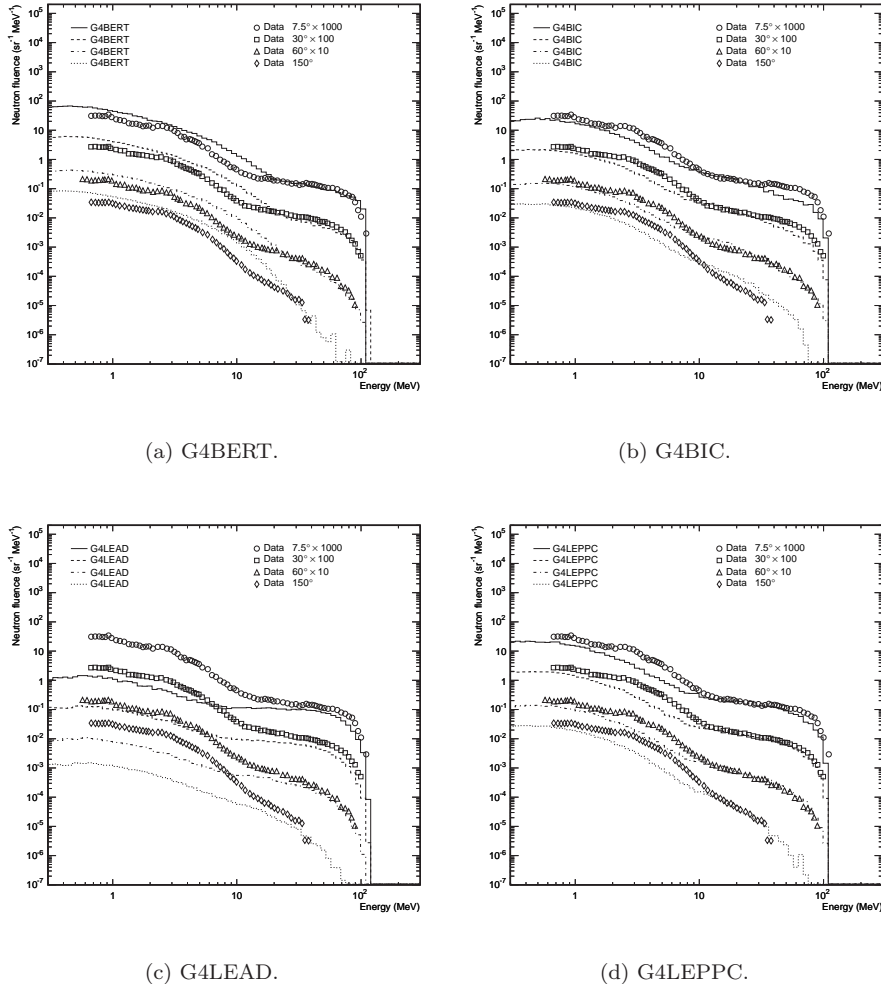


Figure 5.11: Directional neutron spectra comparisons. 113 MeV protons incident on stopping length U-238 target cylinder (radius 4.00 cm, length 3.00 cm). The data for the different angles have been separated using the indicated scale factors.

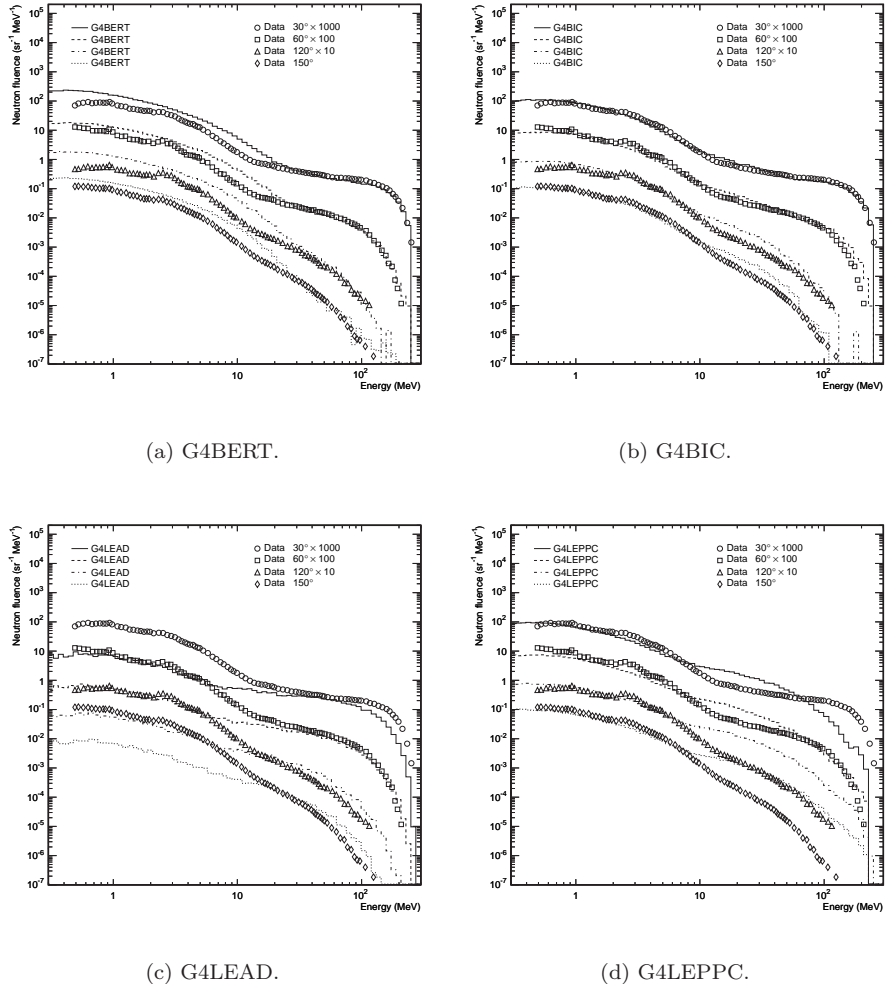


Figure 5.12: Directional neutron spectra comparisons. 256 MeV protons incident on near stopping length U-238 target cylinder (radius 4.00 cm, length 3.00 cm). The data for the different angles have been separated using the indicated scale factors.

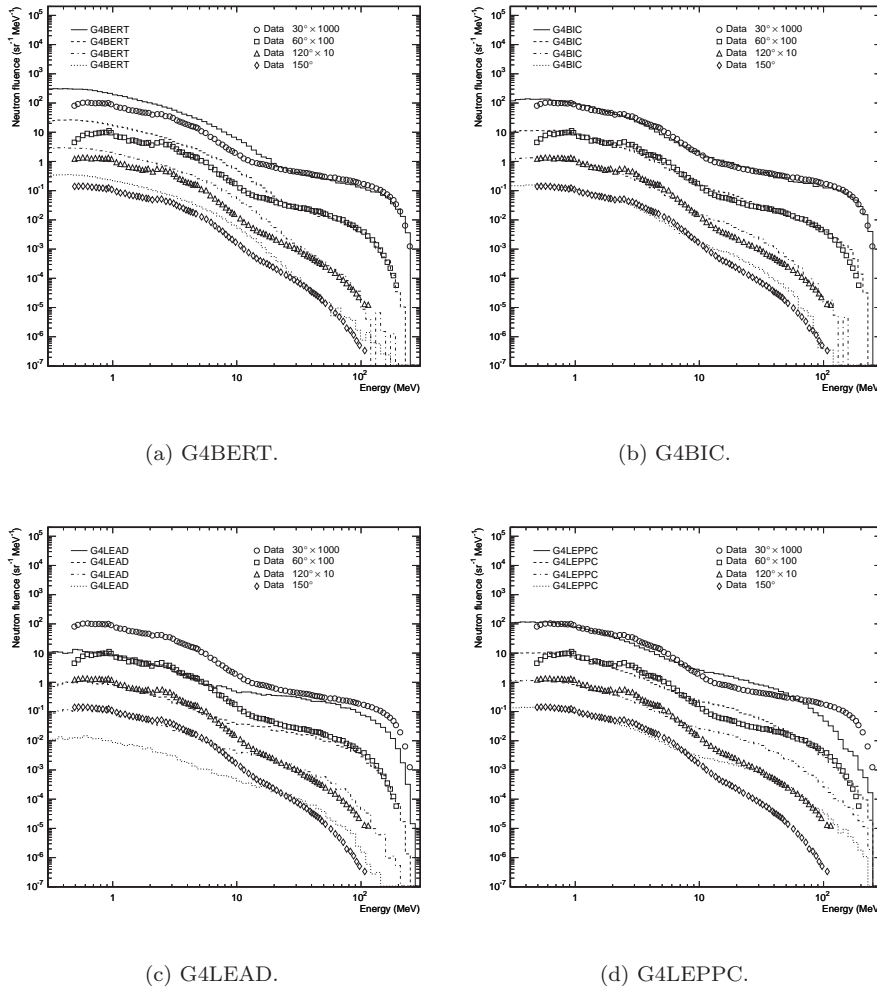


Figure 5.13: Directional neutron spectra comparisons. 256 MeV protons incident on stopping length U-238 target cylinder (radius 4.00 cm, length 5.00 cm). The data for the different angles have been separated using the indicated scale factors.

5.2.1 Longitudinal and radial energy depositions

Energy deposition of particles in water are important because water is a good approximation of human tissue. Figs. 5.14(a) and 5.14(b) show the Bragg curve for a 202 MeV proton pencil beam incident on a water cylinder (radius 10 cm, length 30 cm) along the axis of the cylinder. The cylinder was sliced in 1 mm segments and the energy deposition in each segment was recorded. Fig. 5.14(c) shows the radial energy deposition in a 1 mm segment centered at the Bragg peak.

These types of comparisons are sensitive to the electromagnetic interactions of the different codes. The Geant4 models all use the same module for these interactions and can thus be expected to behave similarly. The Binary Cascade model compares best with SHIELD-HIT, see Fig. 5.14(a). However, the small difference between the Geant4 models in this case does not imply a preference of either model for space radiation shielding studies when considering the uncertainties of the incident radiation fields in that application. It should also be noted that the position of the Bragg peak is extremely sensitive to the mean-ionization potentials for the target material used in the code. For a comparison of the stopping powers of protons see [59], the differences between various measurements/calculations are about 10%. Considering this the agreement shown in Fig. 5.14(b) is very good. It is also comparable to the segmentation distance mentioned above.

Important processes influencing the result apart from ionization are multiple Coulomb scattering and energy-loss straggling. Multiple Coulomb scattering in Geant4 [4] is based on a new model and not on the standard Molière formalism, which SHIELD-HIT uses. These approaches are not equivalent [43] and differences in simulation results such as Fig. 5.14(c) can be expected.

5.2.2 Neutron spectra

In Fig. 5.15 the neutron fluences per boundary surface of the water cylinder are compared. For the back of the cylinder, Fig. 5.15(a), the G4BIC model predicts a neutron fluence approximately a factor of two higher than SHIELD-HIT. This type of comparison, with a target containing light elements, is highly sensitive to the transport of low-energy neutrons and the cross-sections used in the models for elastic scattering. These are different in Geant4 and SHIELD-HIT. In Geant4 a selection of several evaluated nuclear data libraries is used (see [4] and references therein), while in SHIELD-HIT the transport is based on a 28-group neutron data system.

The agreement for the side of the cylinder is better, here G4BIC is within 50% of SHIELD-HIT, see Fig. 5.15(b). For the forward face, Fig. 5.15(c), there is a very good agreement at low energies. At higher energies, starting at about 7 MeV there is an edge in the SHIELD-HIT spectrum. This is due to a known imperfection of some nuclear models in SHIELD-HIT which will be eliminated in the next version of the code.

Similar deficiencies to what was observed for G4LEAD in the comparisons with experimental data can be seen for backward and side-going neutrons. For forward-going neutrons an obviously artificial structure can be seen at about 10 MeV. The behavior of G4LEPPC is similar to what is seen in Fig. 5.2(d).

5.3 Comparisons to BRYNTRN

Codes similar to BRYNTRN [36] are actively used in the NASA manned space program. It is therefore very interesting to compare Geant4 to this code since the ultimate goal is to study radiation effects on humans in space. BRYNTRN is not a Monte Carlo based code. Instead, it solves 1-D Boltzmann transport equations that describe how radiation fields are transformed when passing through a given mass thickness. To be able to compare Geant4 to the BRYNTRN results, the 1-D BRYNTRN geometry was modeled as a cylinder with a large radius compared to the thickness of the slab/cylinder. The cylinder was then irradiated with a wide uniform beam and the particle fluence measured over a small area (compared to the beam area) directly behind the slab. Fig. 5.16 shows the particle fluence behind a semi-infinite slab irradiated with protons with energies same as in the frequently-used 1956 solar particle event (integral spectra parameterization available in [28]).

For the proton fluence behind 10 g/cm² of aluminum there is a good agreement between the Geant4 models and BRYNTRN, see Fig. 5.16(a). For the proton fluence behind 15 g/cm² of water there is similar agreement. Considering the radically different methods of particle transport the neutron fluences behind the aluminum and water slabs, Figs. 5.16(b) and 5.16(c), agree well for the G4BIC and G4LEPPC models and BRYNTRN, with the exception of the fluence at lower energies for water. Unfortunately, an older version of BRYNTRN was used for this comparison. Modern versions of BRYNTRN/HZETRN using a multigroup method and backwards scattered neutrons predict higher low-energy neutron fluences, see [60] for BRYNTRN results for a simulation configuration similar to the one presented here. G4LEAD performs similarly to the studies above, lacking neutrons at lower energies and giving better agreement at higher energies. Comparisons made for slabs with twice the thickness show similar results.

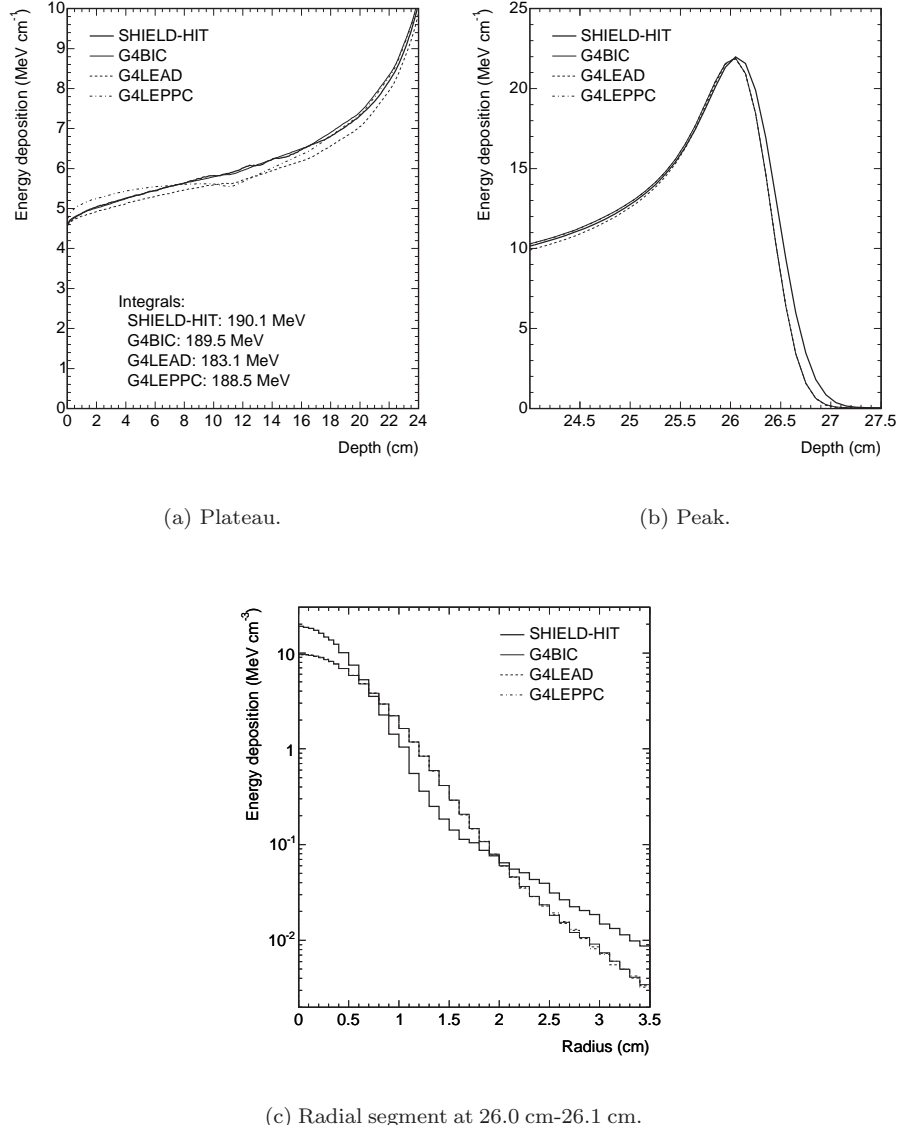


Figure 5.14: Energy deposition comparisons to SHIELD-HIT. 202 MeV protons incident on a water cylinder (radius 10 cm, length 30 cm). The simulation results obtained with the different Geant4 models overlap in Figs.(b) and(c).

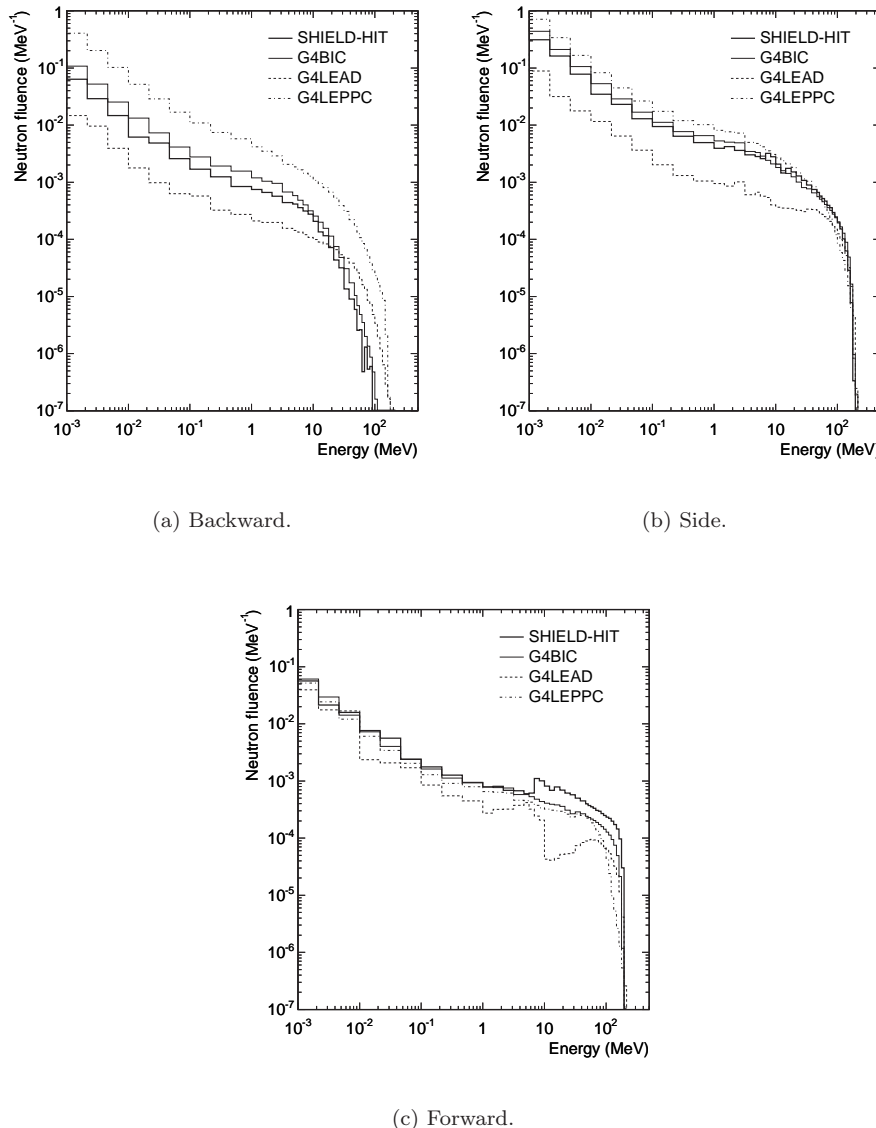


Figure 5.15: Neutron spectra comparisons to SHIELD-HIT for neutrons leaving boundary surfaces of target water cylinder.

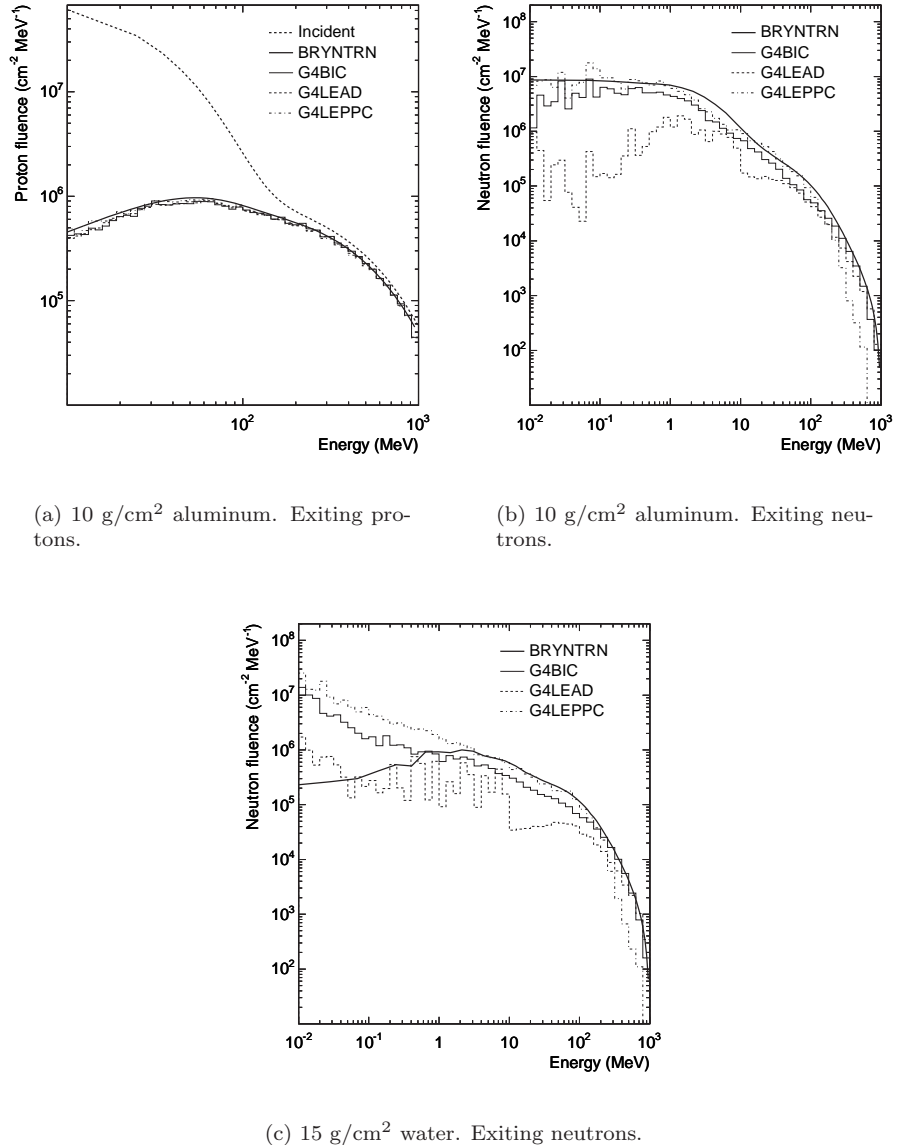


Figure 5.16: Particle spectra comparisons to BRYNTRN for particles exiting the slab in the forward direction.

Chapter 6

Geant4 geometry models of ISS and Columbus

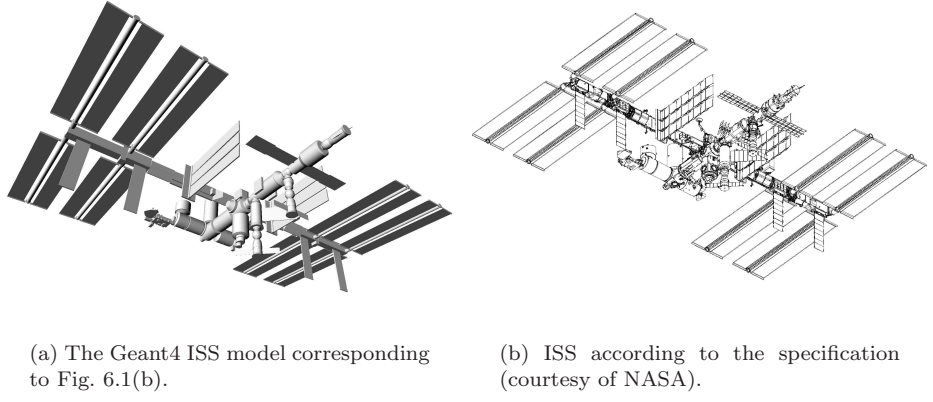
This chapter is based on the paper “Implementation of a detailed Geant4 geometry model of the International Space Station and the Columbus module” by the author [8]. A more technical description of previous versions of the models and the process of developing them is available in [61]. Additionally, a truncated ISS model suitable for faster calculations is presented in section 6.1.4.

Correct transport of incident radiation into the Columbus cabin requires a detailed implementation of models of Columbus and ISS in a Geant4-application. This section describes such an implementation in the context of the DESIRE project.

6.1 ISS model

The DESIRE Geant4 ISS model corresponds to ISS in the so-called 14A configuration. The mass of ISS (excluding Columbus) in this configuration is 352 metric tons and the model consists of about 350 volumes. Figs. 6.1(a) and 6.2 shows the Geant4 ISS model and Fig. 6.1(b) is ISS according to the specification [62]. A detailed view of the forward ISS modules is shown in Fig. 6.2. The (general) ISS velocity direction is marked “forward”. Other directions used for description of ISS are: aft, zenith, nadir (opposite of zenith), starboard and port. The main visible features of ISS in Fig. 6.1 are the main solar panels and the 108.4 m long truss structure. The Columbus module is included in Fig. 6.2 and has a length of 6.6 m (excluding external payloads). The present configuration of ISS is shown in Fig. 1.1.

The specification used for the ISS geometry contains the mass of individual ISS modules (e.g., Columbus, the U.S. laboratory, the S0 truss section) and in some cases parts of such modules. Each module and module part in the implementation has been assigned the correct mass. Since no material specifications for the



(a) The Geant4 ISS model corresponding to Fig. 6.1(b).

(b) ISS according to the specification (courtesy of NASA).

Figure 6.1: Comparison of the DESIRE Geant4 ISS model to the model in the specification [62].

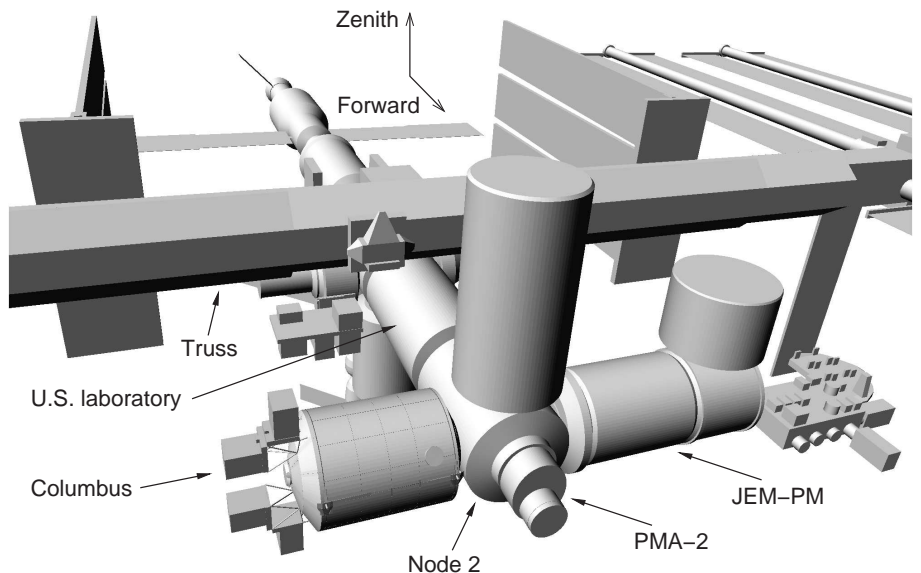


Figure 6.2: The forward part of ISS.

modules were available at the time of the implementation all ISS modules were constructed from pure aluminum. The total module mass was distributed in the

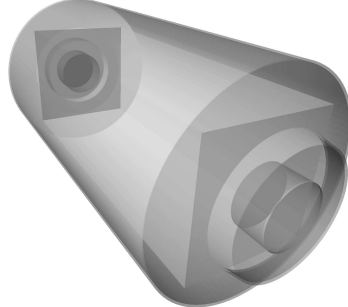


Figure 6.3: Transparent view of the U.S. laboratory in the Geant4 ISS model.

module geometry in different ways depending on the type of module.

6.1.1 Habitable modules

The habitable ISS modules and their interiors have been modeled using a set of approximations. The starting-point was to assume the external module surfaces to be cylindrically symmetric. Fig. 6.3 shows the U.S. laboratory as an example of the modules discussed here. The mass of the module is divided equally between an approximation of the hull and the module interior. The hull thickness is calculated from the available hull mass, assuming a pure aluminum hull material.

Inside the hull of each habitable module there is an interior and a cabin filled with air. The cabin is built from one or a few boxes with a diagonal which is 50 cm less than the module diameter at the position of the box. For modules connecting to other modules, a cylindrical opening is added at the appropriate place only if the opening is parallel to the module axis. While Geant4 supports boolean solids, which would allow for hatches also in other directions, this possibility was not used to simplify the geometry implementation. For example the Node 2 model (see Fig. 6.2) has hatches only at the connections to the U.S laboratory and PMA-2. At the location in the model where the hatches leading to Columbus and the Japanese laboratory (JEM-PM) should be there is only solid interior and hull. After determining the dimensions of the cabin the remaining volume can be used to calculate the average density of the aluminum used for the interior.

The above description holds for all habitable modules except the Soyuzes, Progress, the Airlock and the Cupola. The Cupola and the Airlock are modeled with a cylindrically symmetric cabin inside the hull and do not contain any interior. The Soyuzes and Progress contain a cylindrically symmetric cabin without any interior in the capsule part of the spacecraft. The non-capsule parts of these modules are instead completely filled with the interior material.

In some cases, a habitable module may contain some separate parts, for example solar panels or payload platforms. Here, the mass of the separate part of the module

was in general not available in the specification and had to be estimated.

6.1.2 Pressurized Mating Adapters

There are three PMAs (Pressurized Mating Adapters) on the station. These are not cylindrically symmetric, but have a quite complex geometry. In the implementation this geometry has been greatly simplified. The PMAs do not contain any interior and are implemented as an aluminum hull with a thickness fitted to the mass of the PMA. PMA-2 can be seen in Fig. 6.2 connected to Node 2.

6.1.3 Other modules

All non-habitable modules (e.g., solar panels, radiators, truss segments) have been modeled by approximating their boundary surfaces and assigned an aluminum-type material with a density adjusted to the total module mass. The geometry of certain parts of ISS is very complex (e.g., the truss sections). In general, complex geometries have been simplified to consist of only a few volumes.

6.1.4 Truncated ISS model

As the Monte Carlo calculation speed is strongly dependent on the size of the geometry model used, a smaller, truncated version of the ISS has been developed. The model is shown in Fig. 6.4 and contains only the ISS modules located closest to Columbus. A module that is included in the specification for ISS configuration 14A is the Centrifuge Accommodation Module (CAM), which is shown in Fig. 6.2 on top of Node 2. It is now certain that this module will not be launched, and as such it has been removed from the truncated ISS model. The modules included in the truncated ISS model are PMA-1, Node 1, the Airlock, the U.S. laboratory, Node 2, PMA-2, JEM-PM, JEM-PS, the Cupola, External Stowage Platform-2 and Z1 as well as the truss segments S0, S1 and P1, and the MSC. This results in a mass (excluding Columbus) of 136.5 metric tons.

6.2 Columbus models

Three models of Columbus have been implemented. The “Columbus1” model was developed first from the short specifications at the ESA Columbus web page [63]. The more detailed “Columbus3” model was later developed according to a set of drawings [64] acquired via the ESA office in Houston. These drawings are only an excerpt from a significantly larger document [65] received later. Most of the implementation was already completed by that time and the larger document had only a limited impact on the final implementation. An intermediate “Columbus2” model has been developed to investigate whether the detail of the “Columbus3” model is adequate (i.e., how dependent the simulation results are on the level of

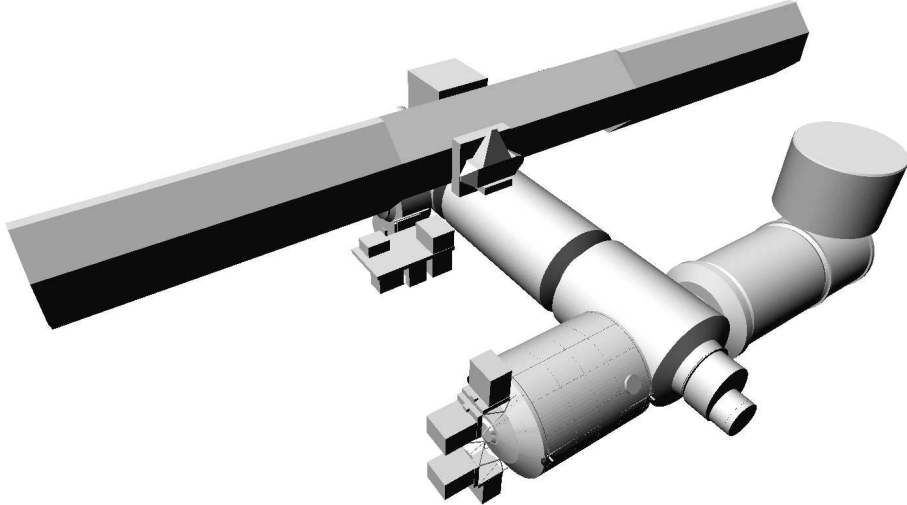


Figure 6.4: The truncated ISS model.

detail of the model). Since it is a simplification of the “Columbus3” model it is described after that model.

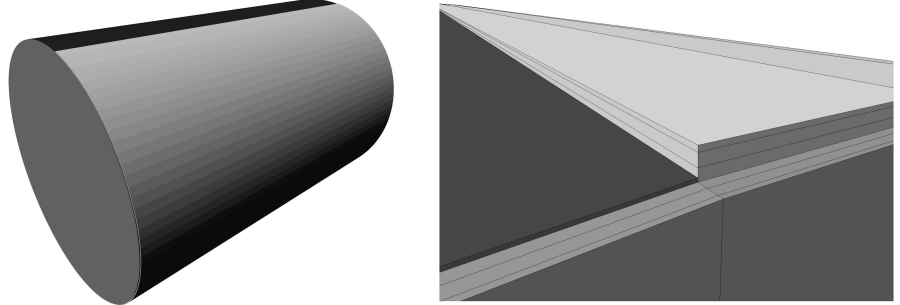
6.2.1 Columbus1

The Columbus1 model consists of 10 volumes with a total mass of 4386 kg. The geometry is shown in Fig. 6.5(a). It is purely cylindrical with a length of 6.9 m and a radius of 4.5 m. This model provides a baseline to which more refined models can be compared, although both the geometry of the model and the total weight are not representative of the real Columbus geometry.

Columbus1 is modeled as an aluminum 2219 (aluminum with 5% copper) hull shaped like a closed barrel, with the barrel-part being slightly thicker than the end-caps. The Columbus hull is protected from breaches by a Meteoroid and Debris Protection System (MDPS) enveloping the entire module. Both the Columbus hull and the MDPS provide a significant part of the radiation shielding capability for onboard astronauts.

The probability of hull damage is greater for the parts of Columbus facing the direction of travel. The forward part thus has a thicker and more complex MDPS than the aft part. Similarly, because the port side faces ISS (Node 2) it has less need for additional protection due to the intrinsic protection already provided by the bulk material of Node 2. Thus, the starboard MDPS provides more protection than the port MDPS.

The MDPS consists of up to three layers of panels, as shown in Fig. 6.5(b). The primary MDPS panels are made of aluminum 6061T6 (pure aluminum with density



(a) Columbus1 viewed from the forward-starboard-zenith direction. The forward, aft and starboard hull parts are visible.

(b) The layering of the forward and starboard MDPS and their thickness compared to the aft MDPS layer.

Figure 6.5: The Columbus1 model.

2.71 g/cm³), the secondary panels of Kevlar and the tertiary panels of NextTel 650 (a ceramic fiber material). The cylindrical Columbus1 model contains the amount of material described in Table 6.1 in the discussed directions. No other components are included in this model.

Table 6.1: The MDPS and hull thicknesses for different surfaces of Columbus.

Module surface	Primary MDPS (mm)	Secondary MDPS (mm)	Tertiary MDPS (mm)	Hull (mm)
Forward	2.57	5.6	5.3	4.8
Aft	1.6	n/a	n/a	4.8
Port	1.6	n/a	n/a	3.8
Starboard	2.57	5.6	5.3	3.8

6.2.2 Columbus3

The Columbus3 model is far more detailed and realistic than the Columbus1 model. It consists of about 750 volumes and has the correct total mass of 16750 kg [62].

Outside Columbus, visible to the left in Fig. 6.6, is the External Payload Facility (EPF). Four experiments mounted on the EPF are modeled as bounding-boxes with a mass of 290 kg each. The EPF itself was assigned a mass of 150 kg from the total module mass. Other details on the outside of Columbus3 are the Power and Data Grapple Fixture (PDGF) and the port cone forward and aft feedthroughs (PFF, PFA). These are modeled as discs of appropriate size and thickness. The discs are

made out of half-density aluminum, creating a small additional mass contribution at the location of these structures. The main visible structure in Fig. 6.6 is the primary MDPS layer. It has the thickness and mass properties shown in Table 6.1, apart from a few regions around the mounting points of the structure where the thickness is increased to 5 mm. Fig. 6.7 shows the port side of the Columbus3 model with most structures except the MDPS removed. In addition to the primary MDPS, the PFF and PFA feedthroughs are visible, as is the inside of the tertiary MDPS panels (the secondary panels are located right outside these). The structures used for mounting the end-cone MDPS panels are also shown. No information on the material used for these structures was available and the implementation uses aluminum with a density one-fifth of that of normal aluminum. The implemented structure is fairly coarse compared to the more detailed drawings in [64].

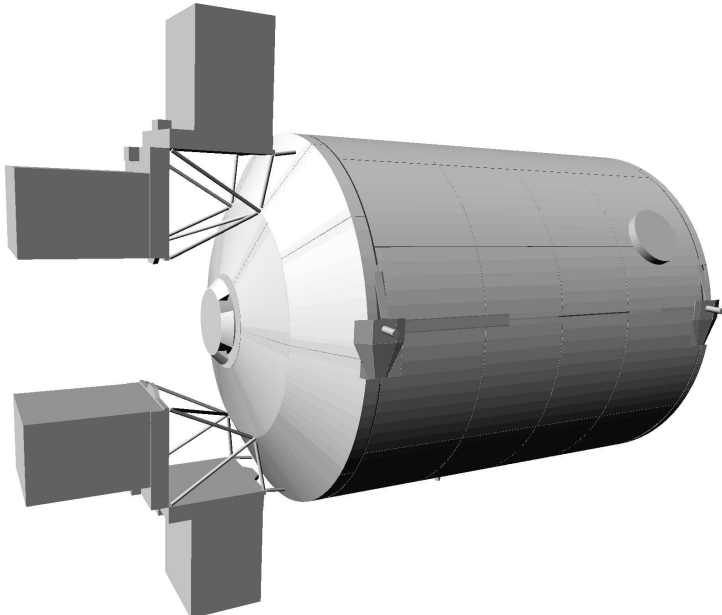


Figure 6.6: The full Columbus3 model and the external experiments viewed from the forward-starboard direction.

Removing the MDPS structures leaves only the hull and its support visible, see Fig. 6.8(a). The fittings are built from aluminum with a density half of that of normal aluminum, the other parts are made of the hull material aluminum 2219 discussed in section 6.2.1. The total hull mass of Columbus, including certain support structures, is 3004 kg according to [66]. Using the hull thicknesses from Table 6.1 the hull mass is however only about 2250 kg. The difference is due to lack of structural thickening of the hull around interfaces between the main hull parts and lack of hull details in general. Therefore the Columbus3 hull thicknesses have

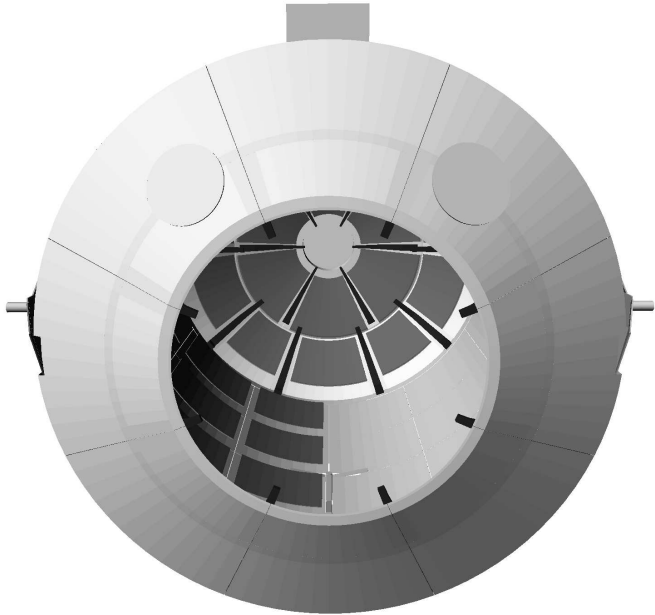
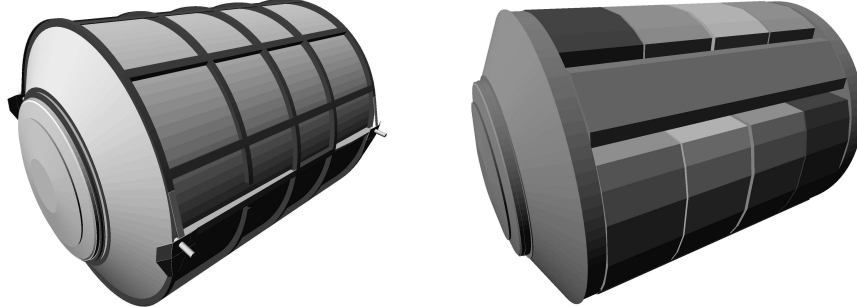


Figure 6.7: The Columbus3 MDPS panels and support structures viewed from the port direction.

been scaled with a factor 1.51 to 7.25 mm (forward and aft) and 5.74 mm (port and starboard), resulting in a correct total hull mass.

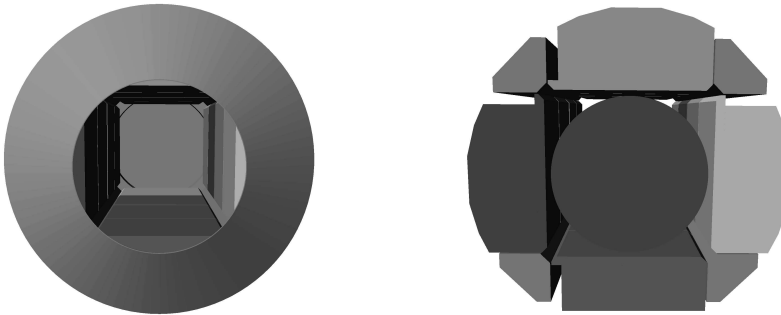
If the hull is removed, the interior shown in Fig. 6.8(b) becomes visible. The Columbus interior consists of 16 racks, four stand-offs and the interiors of the port- and starboard cones. In Fig. 6.8(c), it is possible to view a part of the cabin. Racks and the port cone interior are visible, as well as the starboard cone interior at the far end.

The masses of the stand-offs and port- and starboard cone interiors have been estimated to 4×323.5 kg, 307.3 kg and 473.5 kg respectively according to [67]. The corresponding materials are mixtures of aluminum, copper, steel and traces of water. The Columbus specification [64] gives the approximate general shape of a rack but does not contain any information about the actual hardware in the racks. It does, however, give the maximum allowed rack masses for three types of International Standard Payload Racks (ISPRs): ISPR 1, 997.9 kg; ISPR 08, 804.2 kg; ISPR 06, 600.0 kg. Since the mass of all other components of the Columbus are either available from specifications or could be estimated, the mass used for these racks were 67% of the maximum masses, achieving a correct total mass for the implemented model. The material of the racks were estimated to be 70% aluminum, 10% steel, 10% plastics and traces of copper, nickel, glass and carbon composite according to information obtained from [68]. In addition to the three ISPR types



(a) Hull, support structures and stabilizer fittings.

(b) Columbus3 interior from the outside. Racks, stand-offs and cone interiors are shown.



(c) Columbus3 cabin surrounded by the port- and starboard cone interiors and racks.

(d) Profiles of racks and stand-offs. Detector surface visible in the cabin (central part of figure).

Figure 6.8: Details and interior of the Columbus3 model.

in the specification there is one type of sub-system rack whose maximum mass was not available in the specification, it was determined to be 473.5 kg according to information obtained from [67]. The material used in this case was estimated to be similar to those used for the stand-offs and cone interiors.

According to the specification, the racks can be arranged in three different configurations. This possibility has been added to the implementation. The implementation also allows for run-time definition of racks with arbitrary materials. Rack and standoff profiles are shown in Fig. 6.8(d). The surface at which particles are recorded when entering the Columbus cabin is also shown in the central part of the figure.

6.2.3 Columbus2

The Columbus2 model is a less detailed model of Columbus than Columbus3, consisting of only 23 volumes. However, like Columbus3 it implements the correct total Columbus mass.

The external appearance of Columbus2 is very similar to that of Columbus3 (see Fig. 6.6), with the main cylinder, slanted end-cones and the EPF being present. The MDPS layers described in Table 6.1 are implemented. The hull, consisting of aluminum 2219 (aluminum with 5% copper), is present, with a thickness scaled to achieve a total hull mass of 3004 kg [66]. Inside Columbus2 there is a rectangularly shaped cabin surrounded by an interior consisting of the rack-material described in section 6.2.2. The EPF, consisting of four boxes of 290 kg each, is also implemented.

6.2.4 The Columbus models with/without ISS

All Columbus models can be used for simulations with or without the ISS model. In the case of Columbus1 this is not a problem because of the simple closed-barrel shape. Columbus3 and Columbus2 however have hatches that would, if used without the ISS model, be open to space and the incident primary radiation. Therefore, if such a simulation without ISS is initiated, the model is automatically closed with the normal port hull covering the hatch, as well as an additional panel of the normal port MDPS.

6.3 Limitations of implemented models

Ideally, a particle transport tool such as Geant4 should be able to read CAD files (suitably refined with respect to material data and hierarchical geometry). In Geant4 versions prior to version 6.0 there was functionality for importing CAD geometries in the standardized STEP format [4]. This functionality has since been removed due to incompatibilities between the Geant4 STEP reader and the STEP files generated by various CAD tools. Indeed, correct export of the Columbus geometry to STEP-files from the CAD-system used by ESA (CATIA) could not be verified by another CAD-system (I-DEAS). Both the Columbus and the ISS Geant4 geometries have thus been implemented from hardcopy drawings. As such, they are far less detailed than the corresponding CAD geometries.

Some limitations of the implemented models have been noted in previous sections. Additionally, lack of information about both materials and masses of parts of Columbus has in some cases led to the assignment of only very roughly estimated materials for these components. The materials are aluminum with a density one half, one fifth, or one tenth that of the normal aluminum density. The assignments are compatible with the specified total mass (or total hull mass).

The effect of inadequately detailed models depends on their mass, distance and apparent solid angle from the Columbus cabin. The Columbus3 racks are located next to the Columbus cabin and constitute a large fraction of the total Columbus

mass. However, due to limited information on the design of the individual racks and the time required to implement complex rack geometries as a Geant4 model, the racks are not the most geometrically detailed parts of Columbus3. The impact of this on general purpose calculations, though, is decreased by the fact that the rack configuration will change over time with rearrangements and availability of new experiments.

Chapter 7

Simulations of the Columbus/ISS radiation environment

This chapter presents simulation studies of the trapped proton, GCR proton, SPE proton, and albedo neutron induced radiation environment inside Columbus. Results for various geometry configurations, models of the incident radiation environment and locations inside Columbus are compared against each other, as well as to experimental measurements.

An initial study, comparing results for different geometries are presented in 7.2. Final studies are then presented in sections 7.3–7.6, using only the Columbus3 with the truncated ISS geometry configuration. All studies have been performed using the G4BIC physics list discussed in chapter 4, and validated in chapter 5. The incident radiation environment used as input for the simulations is discussed in chapters 2 and 3. Except where noted, models of the incident radiation environment are based on an ISS altitude of 380 km.

7.1 Computational details

The Geant4 Monte Carlo simulations were performed by generating incident particles on a source sphere enveloping the entire geometry model using the Geant4 General Particle Source module. The starting positions and directions of the particles are generated to create an isotropic flux of particles inside the sphere. Therefore, in the full ISS model (corresponding to a 150 m diameter source sphere), most of the particles fail to hit any part of the ISS or Columbus at all.

Particles entering the Columbus cabin are recorded when they pass the cylindrical surface shown in the central part of Fig. 6.8(d). This surface is chosen as large as possible with respect to the cabin in the Columbus3 geometry (4.3 m length, 2.0 m diameter). The size and location of the surface with respect to the port side of Columbus are the same also in the Columbus1 and Columbus2 models. Dose

rates have been calculated using a 30 cm diameter ICRU sphere [15], placed at the center of the Columbus cabin (i.e., at the center of the cylindrical detector surface). For the Columbus3 with the truncated ISS geometry configuration, 15 ICRU spheres were placed inside the Columbus cabin. Five of these were centered longitudinally in the cabin, with one placed at the center and the other four at the zenith, nadir, forward and aft positions in the cabin (directions are explained in section 6.1 and Fig. 6.2). Of the remaining ten spheres, five were placed similarly at the port side of the cabin, and five at the starboard side of the cabin. The dose rates were calculated in 1 mm thick shells at 10 mm depth in the ICRU spheres. Data on the track energy deposition of the individual particles in the shell were recorded.

The incident particles are generated according to an energy spectrum that has similar properties as the incident spectrum being studied. The proton spectrum used was approximately the sum of a typical belt proton spectrum and a typical GCR proton spectrum, but with additional intensity in the 20–500 MeV range to provide additional statistics for trapped protons. The neutron spectrum had roughly the same slope (in log-log scale) as the cosmic ray albedo neutron spectrum. Each time a particle track intersected the sensitive surface in the Columbus cabin or deposit energy in the ICRU sphere, information on the primary particle energy was saved. During analysis, that energy is used to evaluate the relative difference between the simulated spectrum and the space radiation model spectrum. The difference corresponds to a weighting factor used when producing energy spectra of particles entering the Columbus cabin. For dose rate calculations, the track energy deposition is scaled instead. This allows for use of the same data set for multiple incident spectra. A computer program to merge several data sets and associated metadata, such as primary particle spectra, has been developed and used to create data sets with large amounts of statistics and to improve the statistics in certain important energy ranges.

The required computation time can be decreased in several ways. Most generated particles do not hit the ISS at all. Using a source surface enveloping the ISS and Columbus geometry model more tightly than a sphere would mediate this problem. The dimensions of the full ISS are huge compared to Columbus, and especially the ICRU sphere, and removing remote parts of the ISS would reduce the computation time. Furthermore, to decrease the statistical errors in the reported dose rates, an average from several ICRU spheres placed at various locations inside the Columbus cabin could be calculated. These ideas are realized in the Columbus3 with the truncated ISS geometry configuration (see section 6.1.4). Additionally, various kinds of volume biasing, allowing particles hitting Columbus (or the ICRU sphere) to be transported several times, would decrease statistical fluctuations in this part of the simulation. The results presented in this thesis were simulated on a computing cluster with 10 AMD Athlon 2000+ processors and required a total of 464 CPU-days (itemized by geometry configuration in Table 7.1). 100 days of the CPU-time spent for proton calculations in the Columbus3 with truncated ISS geometry were due to the additional statistics in the 20–500 MeV energy range.

Table 7.1: Labeling of geometry configurations and number of CPU-days required on AMD Athlon 2000+ processors for the results presented in this thesis.

Geometry configuration	Label	CPU-days
Columbus1 without ISS geometry	C1I0	6
Columbus1 with ISS geometry	C1I2	43
Columbus2 without ISS geometry	C2I0	18
Columbus2 with ISS geometry	C2I2	37
Columbus3 without ISS geometry	C3I0	68
Columbus3 with ISS geometry	C3I2	82
Columbus3 with truncated ISS geometry	C3I1	(protons) 190 (neutrons) 20
Total		464

Some further computational details concerning the angular distribution of primary particles are discussed in section 3.6. The errors on the dose rates reported in this thesis are statistical errors on the mean dose rates, estimated by dividing each data set into 10 parts and calculating the RMS of the dose rate deviation of the smaller data sets. All analysis activities were carried out using ROOT [6].

7.2 Comparison of geometry models

Simulations are here performed for seven geometry configurations: Columbus1, Columbus2 and Columbus3, with and without the full ISS geometry, as well as one configuration with Columbus3 with the truncated ISS geometry (labeled according to Table 7.1). This allows the studies of how the bulk ISS structure influences the Columbus radiation environment, as well as of the different shielding capabilities of a very lightly shielded ISS module (Columbus1) compared to the more realistically shielded Columbus3 model. Furthermore, the adequacy of the detail-level of the Columbus3 model as compared to the Columbus2 model is studied. Comparisons are made between the C3I1 and C3I2 models to demonstrate the effect of removing parts of the ISS model located far from Columbus.

7.2.1 Simulated energy spectra

The energy spectra of penetrating primary protons and secondary particles produced in the Columbus and the ISS structure have been calculated. In general, several types of secondary particles are produced in inelastic interactions of space radiation in the hull of Columbus/ISS. Relative effects of those are discussed in section 7.4. This initial study concentrates on the investigation of penetrating protons and neutrons. Fig. 7.1 shows the energy spectra of protons and neutrons entering the Columbus cabin as a result of the incident trapped proton environment.

The incident trapped proton spectrum is also shown. For the purpose of comparison, the same plot axes ranges are used in Fig. 7.1 and Fig. 7.2. The results for Columbus2 deviate only slightly from the Columbus3 results, suggesting that minor improvements to the Columbus3 model would be irrelevant in this case.

In Fig. 7.1(a) the increased trapped proton shielding capability of the more massive Columbus3 model compared to the lighter Columbus1 model is evident. The maximum proton flux is approximately a factor of three lower for Columbus3 than for Columbus1. On the other hand, the neutron production is increased with thicker shielding, see Fig. 7.1(c). This results in almost an order of magnitude greater neutron flux in the radiobiologically most dangerous energy range 100 keV-1 MeV [14] [16]. Introduction of additional mass in the form of the bulk ISS structure is also seen to reduce the proton flux (compare Fig. 7.1(a) and Fig. 7.1(b)) while increasing the neutron flux (compare Fig. 7.1(c) and Fig. 7.1(d)).

Similarly, Fig. 7.2 shows results for incident GCR protons. In this case, the shielding has very little influence on incident protons with energies above 1 GeV. A tail of low-energy protons is present as a result of primary proton interactions. In contrast to Fig. 7.1, the number of low-energy (<1 GeV) protons increases with increasing shielding (Columbus2/3 compared to Columbus1). The increase of the neutron flux in the case of GCR protons is greater than for the trapped protons; the flux in the neutron energy range 100 keV-1 MeV for Columbus3 without ISS is up to a factor 30 greater than for Columbus1 without ISS. As for trapped protons, the neutron flux is greater when ISS is present. No effect on the penetrating particle spectra can be observed for the C3I1 model compared to the C3I2 model, indicating that the effect of removing parts of the ISS model located far from Columbus is very small or negligible.

Artifacts from the energy biasing scheme described in section 7.1 are visible in the low-energy tails of the proton spectra. Histogram bins in this energy range may have a greater statistical error than the associated bin content indicates.

7.2.2 Simulated dose rates

Fig. 7.3 shows the dose rates induced by trapped- and GCR protons for the different geometry configurations. The bars indicate the statistical errors on the mean dose rates. For trapped protons, additional shielding in the form of the more massive Columbus3 model or the presence of ISS is advantageous and reduces the dose rates. The dose rates due to GCR protons exhibit the opposite behavior; increased shielding increases the induced dose rate. This is because the protons in the GCR spectrum have higher energies than those in the trapped proton spectrum. Interactions of these high-energy protons induces a shower of particles in the Columbus/ISS hull, resulting in a greater number of secondary particles entering the Columbus cabin. Consequently, this results in a greater dose rate. Qualitatively similar results for GCRs have been observed in experimental measurements at different shielding depths in aluminum on STS-89 [69].

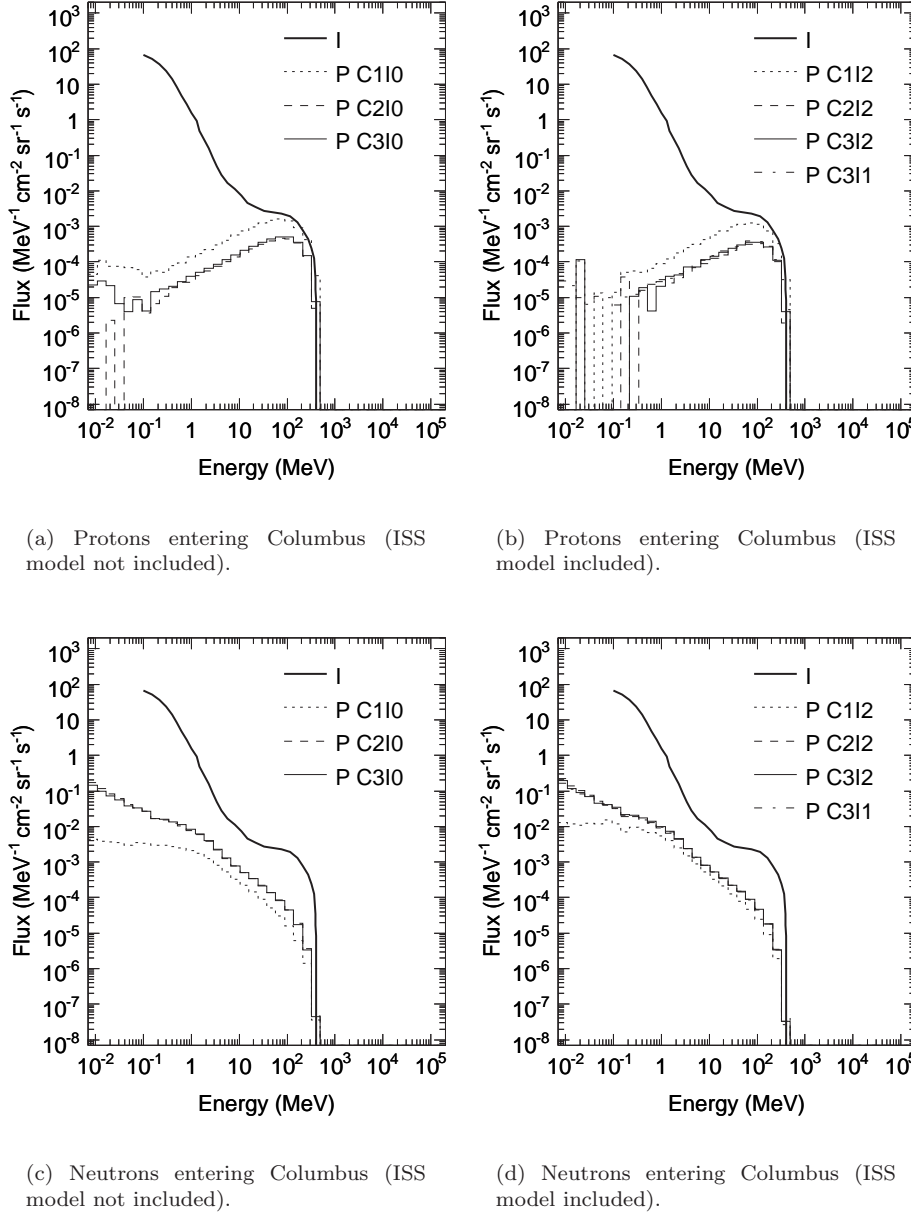


Figure 7.1: Kinetic energy spectra of particles entering the Columbus cabin due to incident belt protons according to the AP8 model for solar maximum. Legend: I – Incident, P – Penetrating.

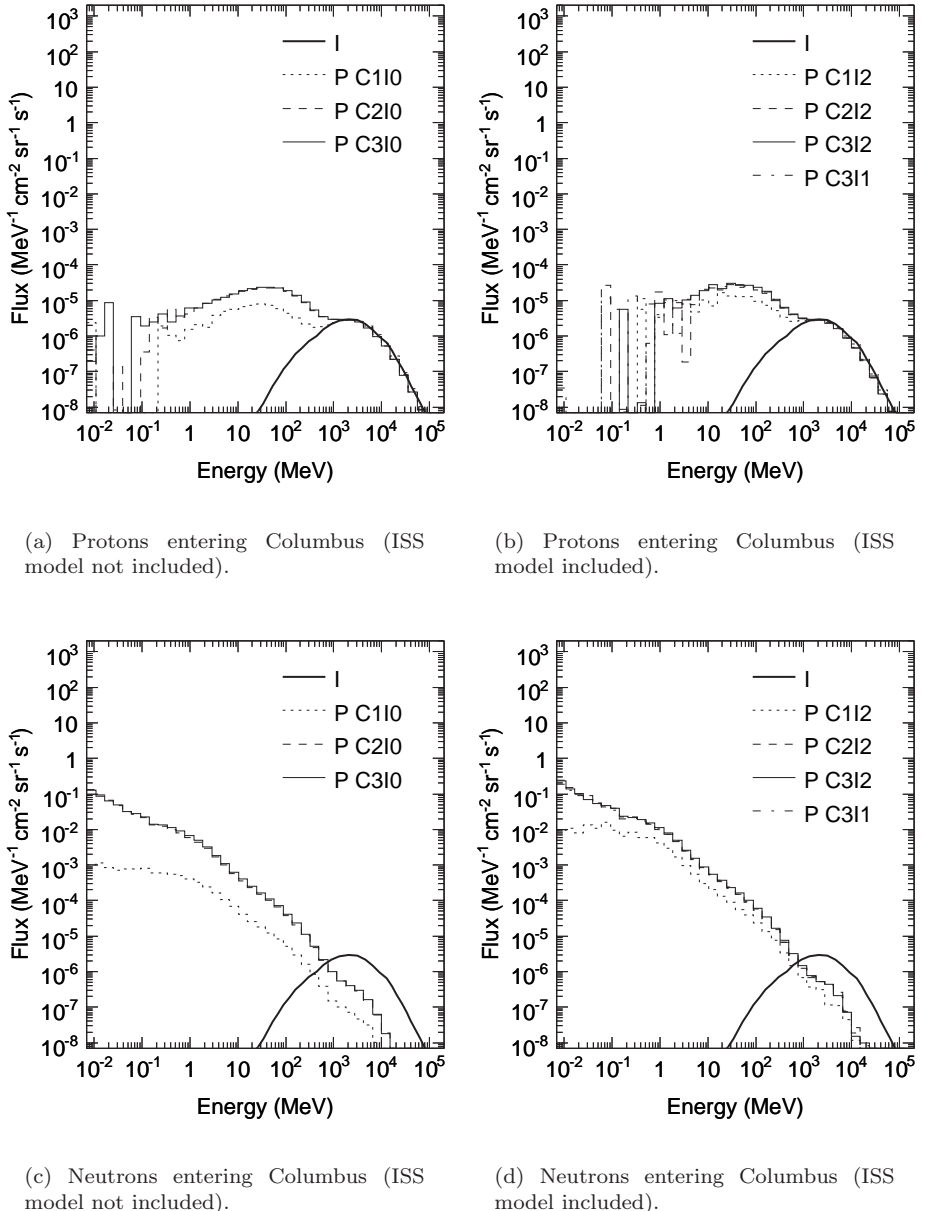


Figure 7.2: Kinetic energy spectra of particles entering the Columbus cabin due to incident GCR protons according to the CREME96 model for solar maximum. Legend: I – Incident, P – Penetrating.

Due to the removal of the CAM in the C3I1 model, an increased trapped proton dose rate compared to the C3I2 model is expected. The CAM module would have had a mass of about 14 metric tons and would have been located next to Columbus, above Node 2. It thus provided additional shielding for a significant solid angle seen from Columbus in the C3I2 model. Fig. 7.3 indicates that the trapped proton dose rate indeed has increased for the C3I1 model, though better statistical significance for the C3I2 result is needed for a conclusive comparison.

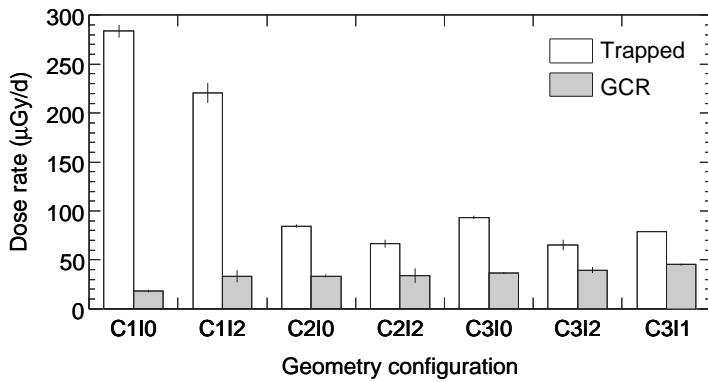


Figure 7.3: Dose rates inside the Columbus cabin for trapped protons and GCR protons for different geometry configurations at solar maximum.

7.3 Radiation belt protons

This section offers a detailed simulation study of the trapped proton induced environment onboard Columbus. For this study, as well as the studies in sections 7.4–7.6, the C3I1 geometry model has been used.

7.3.1 Altitude dependence

The altitude history of the ISS is shown in Fig. 1.3. At higher altitudes, greater trapped proton fluxes are experienced. The incident trapped proton fluxes according to the AP8-MIN model for an ISS orbit of 330 km, 380 km and 430 km is displayed in Fig. 7.4. Fig. 7.4(a) shows the incident fluxes and the resulting penetrating primary and secondary proton fluxes. Similarly, Fig. 7.4(b) shows the incident fluxes and the resulting secondary neutron fluxes. The differences in penetrating particle spectra reflect the differences in the incident trapped proton flux for the different altitudes.

Dose rates for the three altitudes are shown in Fig. 7.5, demonstrating a strong increase in the trapped proton dose rate with increasing altitude. This suggests that, at least from a radiation shielding point-of-view, ISS should operate at an

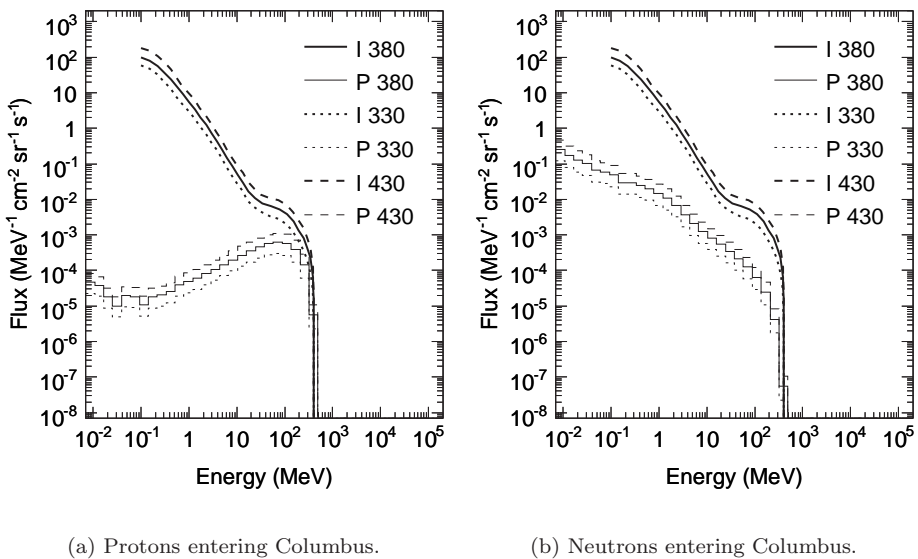


Figure 7.4: Kinetic energy spectra of particles entering the Columbus cabin at different altitudes due to incident trapped protons. The spectra correspond to solar minimum conditions according to the AP8 model. Legend: I 380 – Incident trapped protons at 380 km altitude, P 380 – Penetrating protons or neutrons at 380 km altitude, etc.

altitude as low as possible. The radiation environment is predicted to differ greatly over the wide range of ISS altitudes shown in Fig. 1.3. Furthermore, the dominant part of the dose rate at all three altitudes is seen to be due to penetrating primary trapped protons.

7.3.2 Dependence on model of incident environment and time in solar cycle

Fig. 7.6(a) and 7.6(b) show penetrating proton and neutron spectra for various incident trapped proton models at solar minimum. Fig. 7.6(c) and 7.6(d) show corresponding results for solar maximum. The difference between the AP8 model results and the anisotropic UP model results is quite small. In the range 100–300 MeV the UP-MIN model proton flux entering the Columbus cabin is about 88% of the AP8-MIN flux (Fig. 7.6(a)). In contrast, the much greater incident trapped proton fluxes of the solar minimum PSB97 model result in predictions of penetrating trapped proton fluxes inside Columbus about a factor 3.5–6 greater than the AP8-MIN model in the range 100–300 MeV.

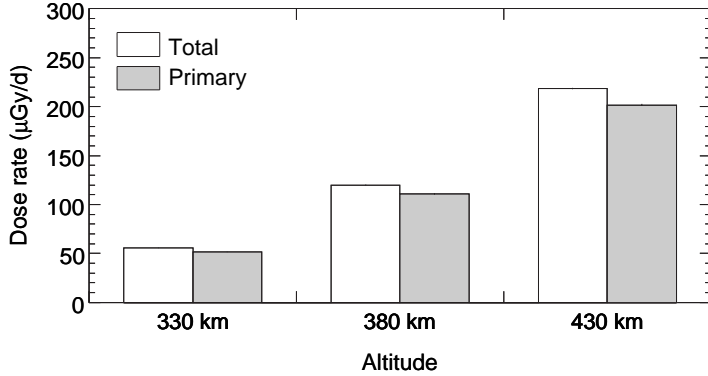


Figure 7.5: Dose rates from all particles as well as only penetrating primary protons inside the Columbus cabin at different altitudes. The dose rates correspond to solar minimum conditions according to the AP8 model.

The average dose rate induced at 10 mm depth in the 15 ICRU spheres in the Columbus cabin by the penetrating particle fluxes in Fig. 7.6 is shown in Fig. 7.7. The solar minimum dose rates are greater than the corresponding solar maximum dose rates. This is due to the decrease in the trapped proton flux at solar maximum for the reasons discussed in section 2.2.2. The AP8-MAX dose rate is thus about 66% of the AP8-MIN dose rate. For the anisotropic UP model the percentage is instead 78%. This is due to the UP model dose rate being 88% of the AP8 model dose rate at solar minimum, while the AP8 and UP models result in approximately the same dose rate at solar maximum. This effect is caused solely by an interplay of the anisotropic incident proton fluxes with the anisotropic shielding distribution since the the omni-directional flux of the UP model is identical to that of the AP8 model.

The solar minimum PSB97 model predicts about a factor of 4 greater dose rate than the AP8-MIN model. This is directly due to the increased trapped proton flux and the greater maximum energy limit of this model, as compared to the AP8-MIN model. The increase in the dose rate is mainly due to the increased trapped proton flux below the AP8 model high energy limit (400 MeV). The contribution to the PSB97 dose rate from incident trapped protons above that energy is about 5% of the total PSB97 dose rate. Discussion on difference between the AP8-MIN and PSB97 incident trapped proton fluxes models is available in section 3.2.2.

The importance of different incident trapped proton energy ranges is assessed in Fig. 7.8. Here the total dose rates for solar minimum models AP8 and PSB97 from Fig. 7.7 shown as a function of primary proton energy. Only primary protons with energies above about 60 MeV contribute. Furthermore, a gradual decrease in the relative importance for different energies is seen when approaching the model high-energy limit (400 MeV for AP8 and 500 MeV for PSB97). This indicates that

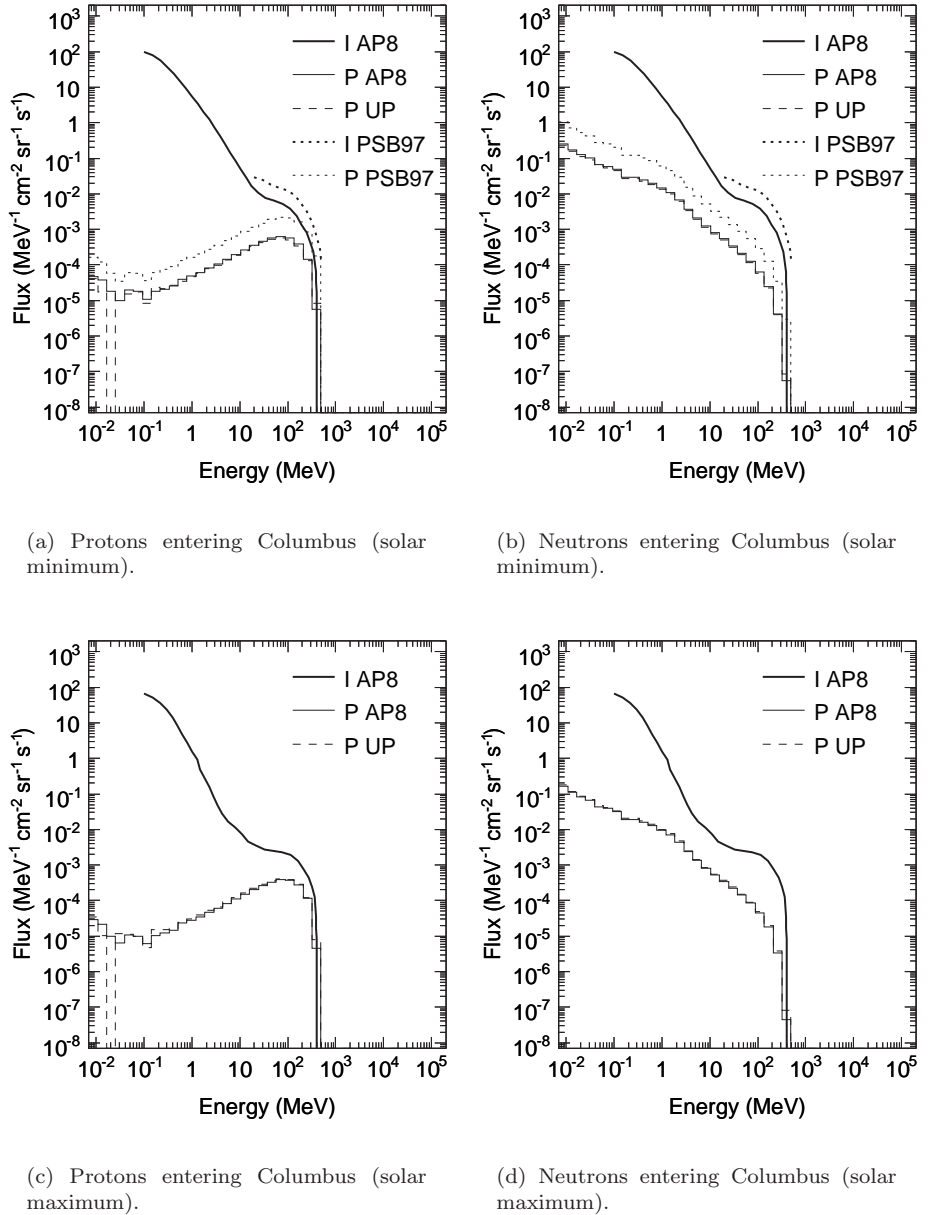


Figure 7.6: Kinetic energy spectra of particles entering the Columbus cabin for different models of the incident trapped proton environment. Legend: I – Incident, P – Penetrating.

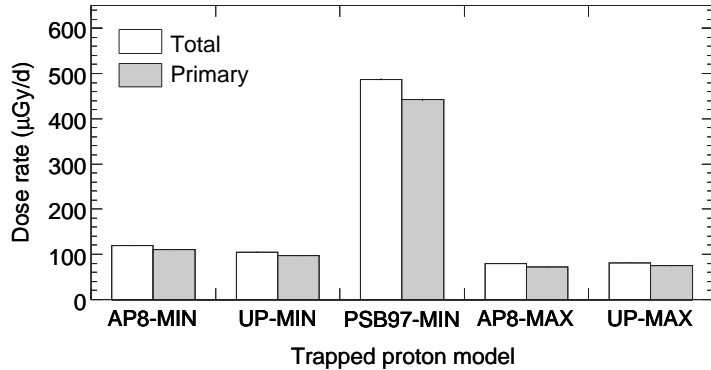


Figure 7.7: Dose rates from all particles as well as only penetrating primary protons inside the Columbus cabin. The dose rates correspond to different trapped proton environment models for solar minimum and maximum conditions.

the models extends to low enough fluxes at high energies. I.e., if the high-energy limit of the model were below the high-energy limit for a non-negligible dose rate in plots such as Fig. 7.8, then a sudden drop in the dose rate would have been visible.

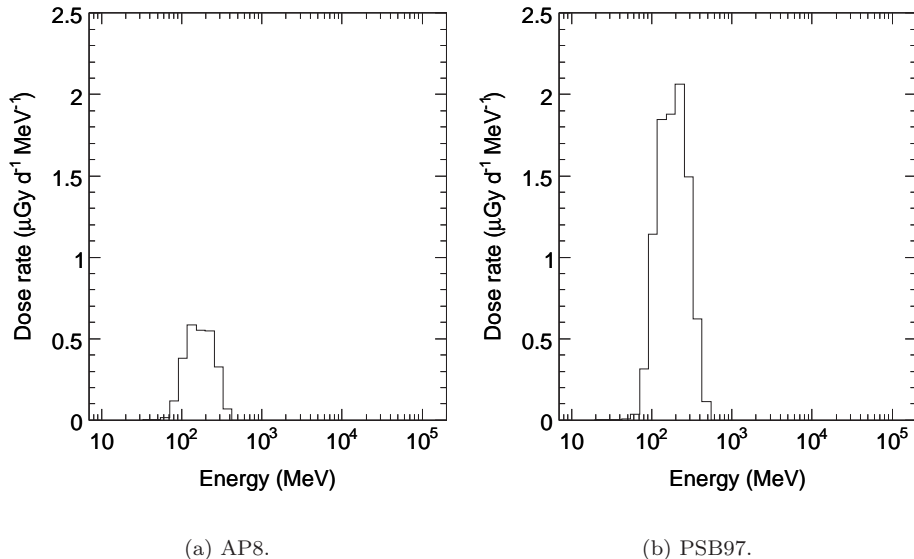


Figure 7.8: Dose rates for the AP8 and PSB97 models at solar minimum as a function of primary proton energy.

Dose equivalent rates for the different models are shown in Fig. 7.9. The relative effect due to secondary particles is higher than in Fig. 7.7. The average quality factors for the total dose equivalent rates are about 1.28–1.30. For primary and secondary particles they are 1.17–1.18 and 2.41–2.67, respectively.

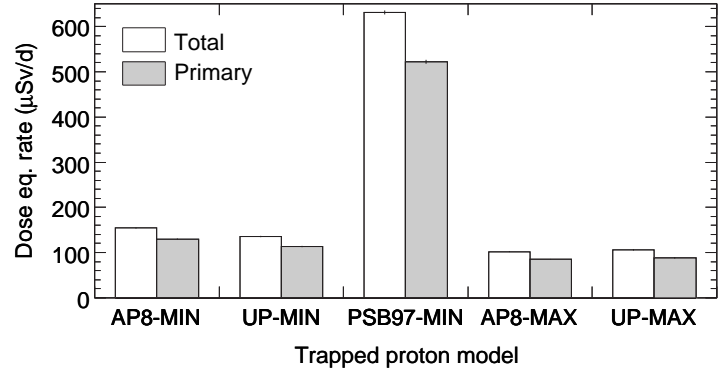


Figure 7.9: Dose equivalent rates from all particles as well as only penetrating primary protons inside the Columbus cabin. The dose rates correspond to different trapped proton environment models for solar minimum and maximum conditions.

7.3.3 Dependence on location inside Columbus and anisotropic effects

Fig. 7.10(a) shows a histogram of the total AP8-MIN dose rate from Fig. 7.7 with respect to the polar angle (θ) and the azimuthal angle (ϕ). The coordinate system is oriented with the polar angle measured from the ISS velocity vector, and the azimuthal angle measured from the zenith direction. The directions are further explained in section 6.1 and Fig. 6.2.

Fig. 7.10(b) visualizes the flux from the forward hemisphere seen from the ISS orbit, facing the direction of the velocity and with the head pointing towards zenith (directions are explained in section 6.1 and Fig. 6.2). Fig. 7.10(c) visualizes the flux for the aft hemisphere. The shadow present to the left in Fig. 7.10(b) and right in Fig. 7.10(c) is due to the increased shielding provided by ISS. The region of higher fluxes to the right in Fig. 7.10(b) and to the left in Fig. 7.10(c) results from the thinner shielding of the starboard cone relative to the main cylinder and racks.

The dose rates shown in Fig. 7.10 are averages over 15 locations inside the Columbus. Plots corresponding to Figs. 7.10(b) and 7.10(c), but for single locations only are shown in Figs. 7.11–7.13. These figures illustrate the anisotropic contribution to the dose rate at three locations along the main axis of Columbus. Fig. 7.11 is for the port-most position inside the Columbus cabin. Similarly, Figs. 7.12 and 7.13 are for the center and the far starboard of the cabin,

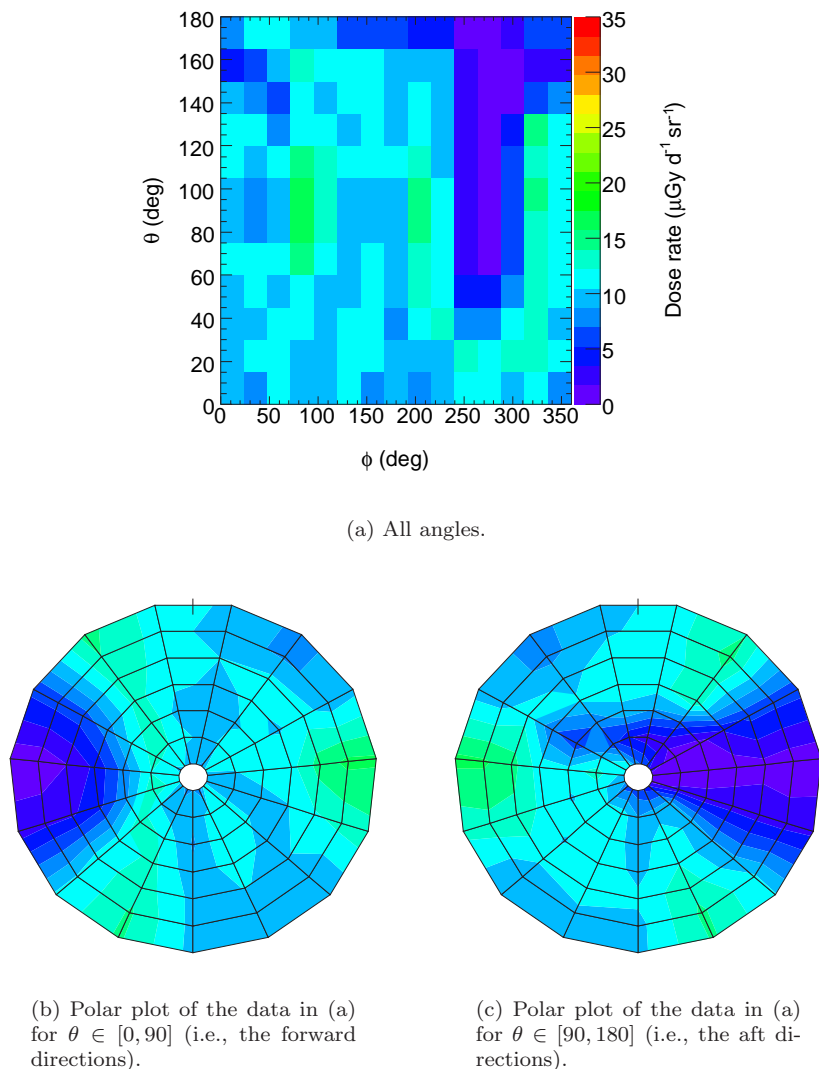


Figure 7.10: The AP8-MIN total dose rate from Fig. 7.7 as a function of the reversed primary proton direction.

respectively. The total dose rates are shown in Fig. 7.14 labeled as “Port-Center”, “Center-Center” and “Starboard-Center” respectively.

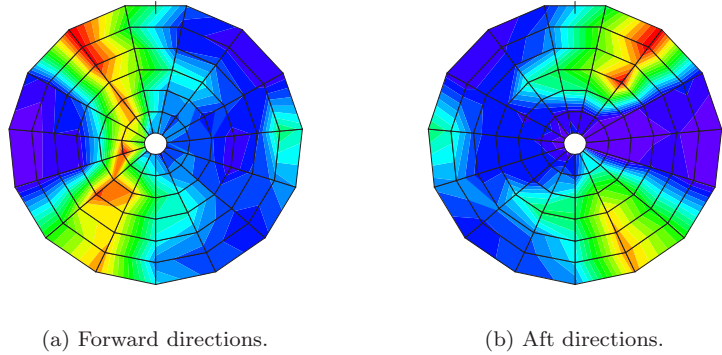


Figure 7.11: The AP8-MIN total dose rate at the port edge of the Columbus cabin as a function of the reversed primary proton direction. The dose rate is shown with the same color scale as in Fig. 7.10. Any off-scale dose rates are shown as the maximum dose rate.

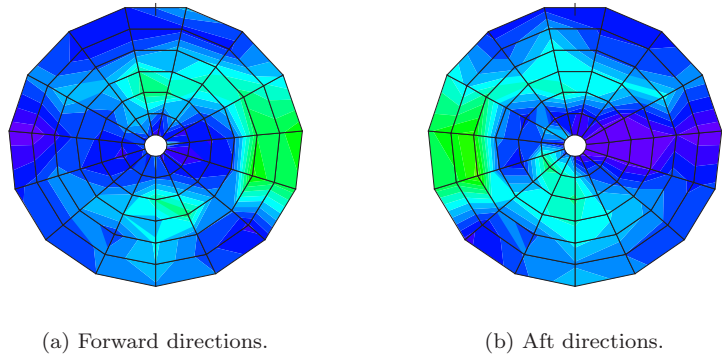


Figure 7.12: The AP8-MIN total dose rate at the center of the Columbus cabin as a function of the reversed primary proton direction. The dose rate is shown with the same color scale as in Fig. 7.10. Any off-scale dose rates are shown as the maximum dose rate.

The arc of greater dose rate just outside the ISS-shadow in Figs. 7.10(b) and Fig. 7.10(c) result from a corresponding arc in Fig. 7.11, which is due to thinner shielding provided by the port cone. At the center of Fig. 7.11(b) the arc is interrupted by additional shielding provided by remote parts of ISS. Fig. 7.13 shows the

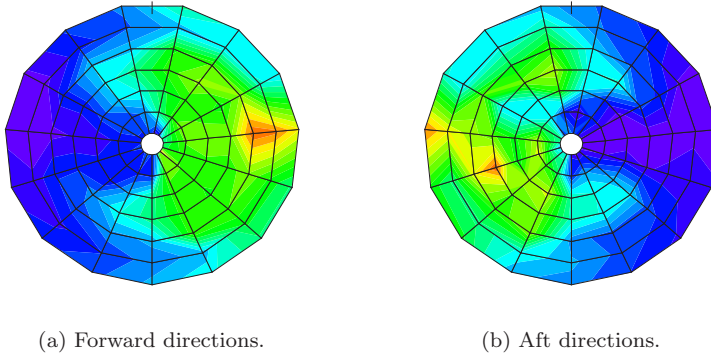


Figure 7.13: The AP8-MIN total dose rate at the starboard edge of the Columbus cabin as a function of the reversed primary proton direction. The dose rate is shown with the same color scale as in Fig. 7.10. Any off-scale dose rates are shown as the maximum dose rate.

increased dose rate close to the relatively lightly shielded starboard cone. The flux through the port cone (Fig. 7.11) is greater than the flux through the starboard cone due to thinner MDPS shielding thickness, see section 6.2.2 and Table 6.1. The shielding thickness of the Columbus interior and hull is smallest when considered at a particle angle of incidence perpendicular to the hull. At other angles, the shielding thickness experienced by the particle grows. This effect is observed for the starboard parts of Fig. 7.11 (the regions bordering the starboard cone). An increased radiation flux can be expected from the regions of the Columbus stand-offs (see Fig. 6.8(d)) due to decreased radial shielding thickness. The effect is visible as horizontal regions of greater dose rate in the middle of the upper and lower parts of Fig. 7.12.

Fig. 7.14 shows the total dose rate at each of the 15 positions inside Columbus. As expected from Figs. 7.11–7.13 the dose rate is lower for the locations at the longitudinal center of Columbus. This is due to the smaller relative solid angle of the cones experienced at the central locations.

Incident trapped proton flux anisotropy

In the studies above the incident trapped proton flux was isotropic, and anisotropies in the flux particles penetrating into the Columbus cabin were caused by an anisotropic shielding distribution. However, as described in sections 2.2.2 and 3.2.3, the incident trapped proton environment in the ISS orbit is strongly anisotropic. The average incident anisotropic trapped proton flux in the ISS orbit according to the AP8-MIN based UP-MIN model at 100 MeV is shown in Fig. 3.4. The resulting dose rate, as well as the corresponding solar maximum dose rate, is shown in Fig. 7.7.

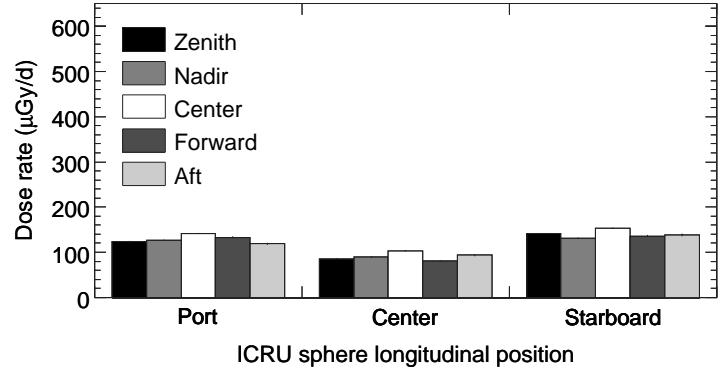


Figure 7.14: Dose rates in all 15 ICRU spheres due to incident belt protons according to the AP8 model for solar minimum. The longitudinal position is listed on the abscissa and the radial position in the legend.

The solar minimum dose rate is shown as a function of the reversed primary proton direction in Fig. 7.15, reproducing the general properties of the primary proton anisotropy as well as illustrating the effects of the ISS shielding capability in the port parts of the figure.

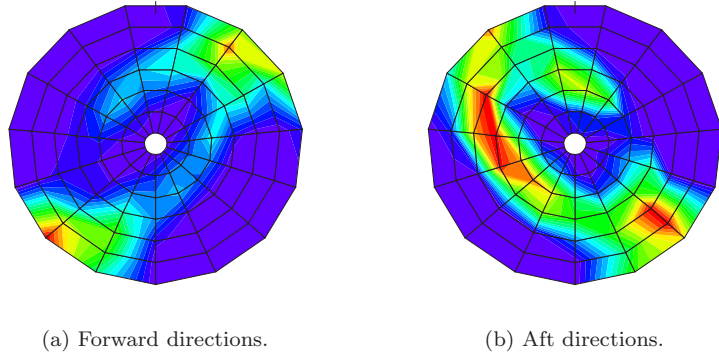


Figure 7.15: The total dose rate (shown in Fig. 7.7) due to a UP-MIN anisotropic trapped proton flux as a function of the reversed primary proton direction. The dose rate is shown with the same color scale as in Fig. 7.10. Any off-scale dose rates are shown as the maximum dose rate.

7.4 Galactic cosmic rays

Kinetic energy spectra of penetrating particles due to incident GCR protons are shown in Fig. 7.16. Results are displayed for the CREME96 and SIREST models of incident GCR protons. A variation due to the solar cycle is also considered. The same observations of penetrating particle spectra as in section 7.2 hold also here. Penetrating high-energy proton fluxes for the CREME96 and SIREST models are separated with respect to the difference in the incident flux. The lower-energy proton tail separation for the two models reflect the separation of the incident spectra in the dominant secondary proton production energy range. The difference in secondary neutron fluxes is about a factor of two, except for the energy region above several GeV, where the primary proton fluxes become similar.

The penetrating particles shown in Fig. 7.16 result in the dose rates in Fig. 7.17. The total dose rates, as well as the dose rates itemized by particle species incident on the ICRU spheres is shown. Compared to the trapped proton dose rates in Fig. 7.7, a much greater relative contribution from secondary particles is demonstrated. Primary and secondary protons account for the major contribution to the dose rate. In addition to secondary photons and leptons, secondary mesons also contribute non-negligibly to the dose rate. Fig. 7.18 shows the corresponding dose equivalent rates. The relative increase in importance of secondary neutrons compared to other particle species is demonstrated. The average quality factors for the total dose equivalent rates are in the range 1.41–1.48. For primary and secondary particles they are 1.33–1.36 and 1.44–1.55 respectively. The average quality factor for secondary neutrons is in the range 4.11–4.50.

Fig. 7.19 shows the solar minimum CREME96 dose rate from Fig. 7.17 as a function of primary proton energy. As for the previously discussed belt proton models in Fig. 7.8, a gradual decrease of the relevance of different energy regions is seen for at lower and upper energy ranges. It is therefore safe to say that the high energy limit 100 GeV of the CREME96 GCR proton model is high enough not to neglect any effect in the dose rate for the present study. Different Geant4 models are used for nucleon-nuclei interactions below and above 10 GeV. Below 10 GeV the Binary Cascade model [41] is used, and above 10 GeV the LHEP model [4] (GHEISHA-like [45]) is used. The increase in dose rate seen at this primary proton energy in Fig. 7.19 is probably due to the transition from one model to the other. The exact reason for the discontinuity is a subject yet to be investigated. Possibly one of the quark-gluon string models available in Geant4 should be used instead of the LHEP model for this type of simulation study.

According to the simulation results about 46% of the total dose rate originates from incident protons above 10 GeV. At present, Geant4 contains no models for ion-nuclei interactions above this energy. GCR ions have a spectral shape similar to that of GCR protons. Assuming the results for protons can be extrapolated to ion-nuclei interactions, this indicates that Geant4 may not yet be suitable for simulation of radiation shielding of all relevant parts of the space radiation environment.

The CREME96 solar minimum dose rate due to primary protons from different

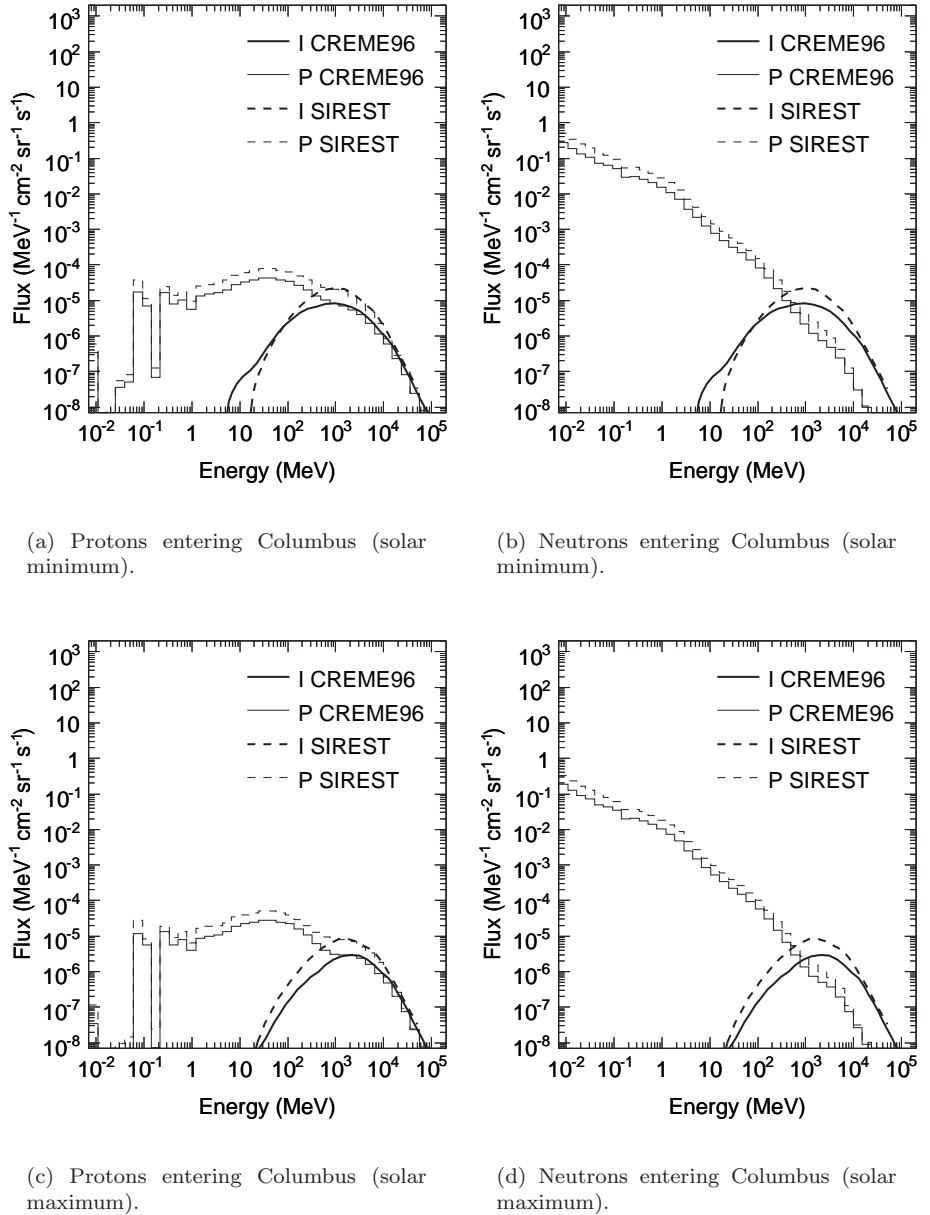


Figure 7.16: Kinetic energy spectra of particles entering the Columbus cabin due to incident GCR protons according to different models. Legend: I – Incident, P – Penetrating.

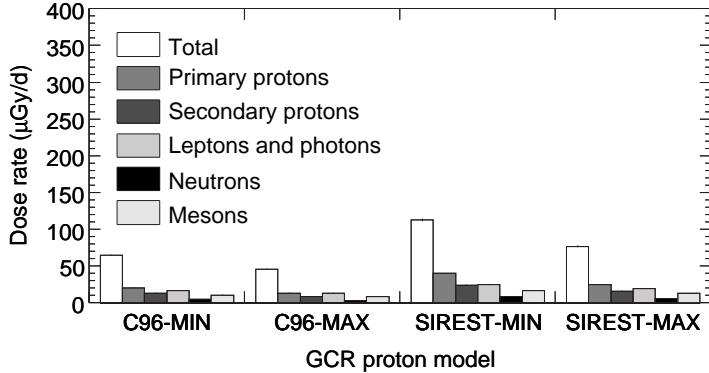


Figure 7.17: Dose rates from all penetrating particles as well as dose rates itemized by particle species inside the Columbus cabin. The dose rates correspond to different GCR proton environment models for solar minimum and maximum conditions. Legend: C96 – CREME96, etc.

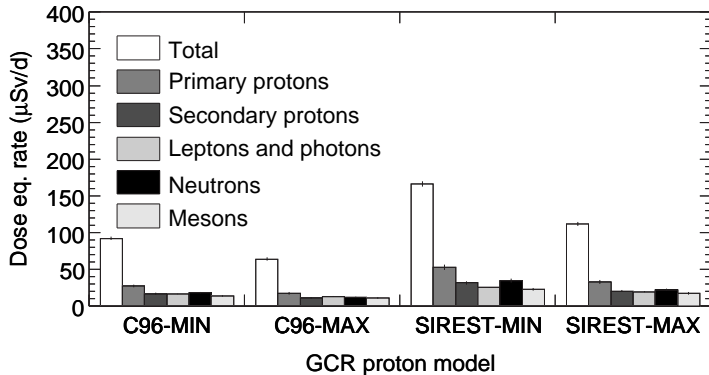


Figure 7.18: Dose equivalent rates from all penetrating particles as well as dose equivalent rates itemized by particle species inside the Columbus cabin. The dose equivalent rates correspond to different GCR proton environment models for solar minimum and maximum conditions. Legend: C96 – CREME96, etc.

directions is visualized in Fig. 7.20. The Earth is visible in the lower part of the figures as a region with zero dose rate. This is due to the assumption in the simulation that no GCR protons are incident from the solid angle obstructed by the Earth (see section 3.6). The presence of the ISS introduces another anisotropic effect due to high-energy GCR proton showering in the material. This introduces a region of higher dose rate in the port side of the figures corresponding to the solid angle of ISS seen from the Columbus cabin. The effect is in contrast to the effect of ISS on belt protons, where the ISS provided additional shielding, see Fig. 7.10.

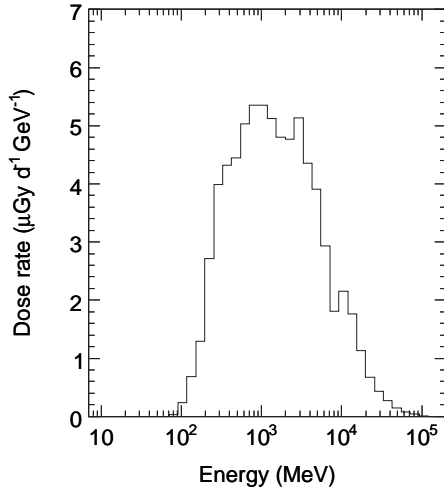


Figure 7.19: Dose rates at solar minimum for incident GCR protons according to the CREME96 model as a function of primary proton energy.

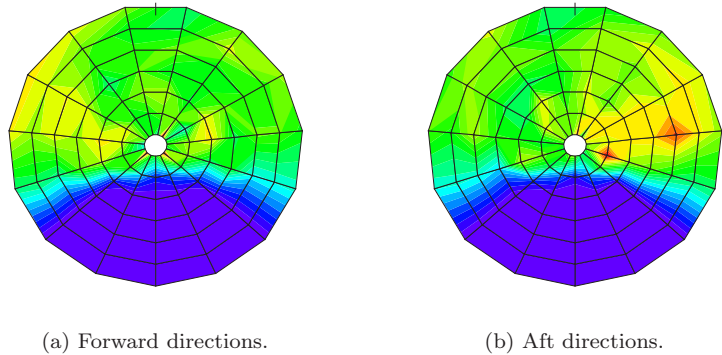


Figure 7.20: The CREME96 total dose rate for solar minimum at all locations in the Columbus cabin as a function of the reversed primary proton direction. The dose rate is shown with the same color scale as in Fig. 7.10. Any off-scale dose rates are shown as the maximum dose rate.

7.5 Solar particle events

SPE proton fluxes and fluences for different scenarios are discussed in section 3.4. Spectra of penetrating protons and neutrons in the Columbus cabin due to the CREME96 worst-day SPE proton fluxes are shown in Fig. 7.21. In contrast to GCR proton fluxes, the shielding of Columbus provides a reduction in the proton

fluxes for all but the highest energies in the model.

Doses for the four scenarios described in section 3.4 are presented in Fig. 7.22. Due to the relatively low energy of SPE protons, the major part of the doses are due to penetrating primary protons. Comparing the doses for the CREME96 worst day and worst week scenarios it is indicated that the major part of the dose due to an SPE is delivered during a shorter time than a week. However, there is an inconsistency between the predictions of the CREME96 worst week and the ESP worst event scenarios. The dose due to the total fluence during an entire event can not possibly be smaller than the dose due to the total fluence during the worst week of an event. A possible reason for the problem is indicated in Fig. 7.23(b).

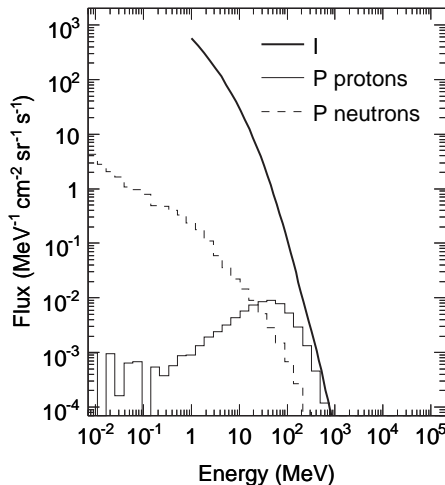


Figure 7.21: Kinetic energy spectra of particles entering the Columbus cabin due to incident SPE protons according to the CREME96 worst-day scenario. Legend: I – Incident SPE protons (P protons) – Penetrating protons (neutrons).

The ESP model in SPENVIS only predicts fluences up to a maximum proton energy of 200 MeV. Assuming that protons above this energy is present in the incident SPE radiation, albeit with a lower relative flux, the dose shown in 7.23(b) should at higher energies approach zero gradually, reflecting the decrease in incident proton flux, like in Fig. 7.23(a). Since this is not the case, the low high-energy limit of the ESP model probably makes it unsuitable for studies of the SPE proton induced dose rate behind thick shielding. Nevertheless, accepting the 95% confidence level cumulative SPE proton fluence of the ESP model, the total dose due to SPEs during one year is estimated to about 2.2 mGy. This results in an average dose rate of about $6 \mu\text{Gy}/\text{d}$, which is very small compared to the GCR and trapped proton dose rates.

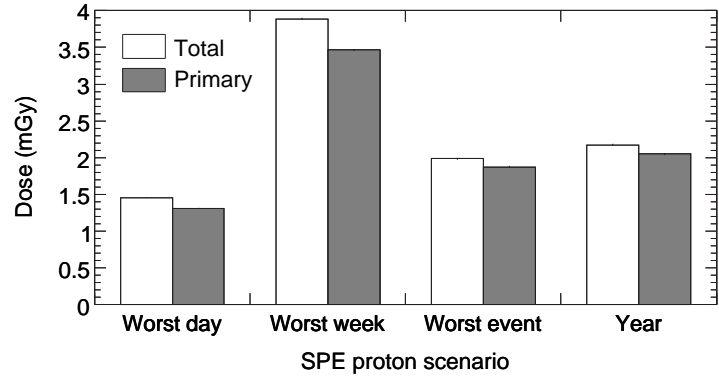


Figure 7.22: Doses inside Columbus due to different SPE proton scenarios for all penetrating particles and for penetrating primary protons only. The “Worst day” and “Worst week” scenarios are according to the CREME96 SPE proton model. The “Worst event” and “Year” scenarios are according to the ESP model for a confidence level of 95%.

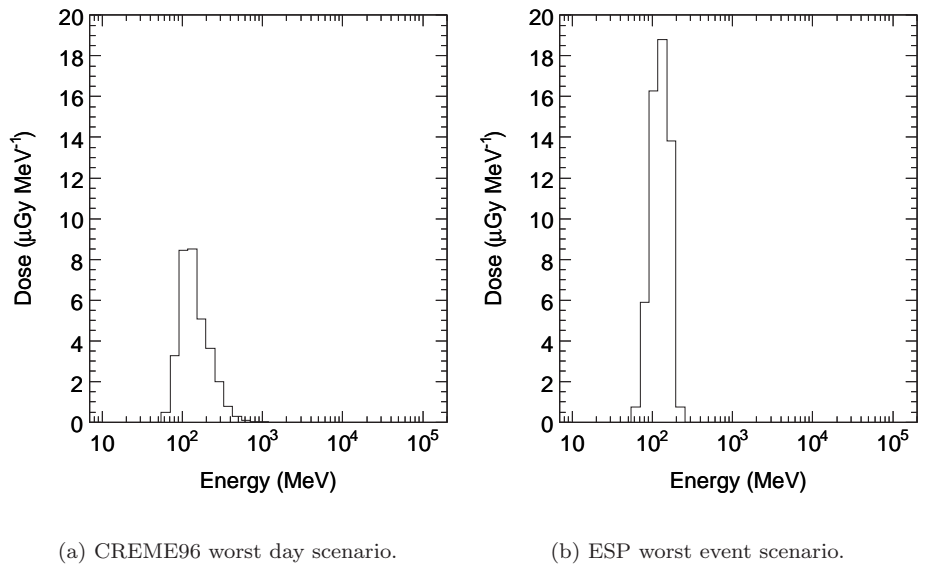


Figure 7.23: Doses for incident solar protons according to the CREME96 worst day and the ESP worst event scenarios as a function of primary proton energy.

7.6 Cosmic ray albedo neutrons

Fig. 7.24 shows penetrating neutrons and protons resulting from incident cosmic ray albedo neutrons. It is evident that this radiation field component is almost unaffected by the shielding provided by Columbus. A much lower flux of protons is present as a result of neutron induced nuclear interactions in the hull. The penetrating particles result in a dose rate of $0.73 \mu\text{Gy/d}$ and in a dose equivalent rate of $0.93 \mu\text{Sv/d}$. This is negligible compared to the trapped proton and GCR proton induced dose and dose equivalent rates, which are at the very least fifty times greater.

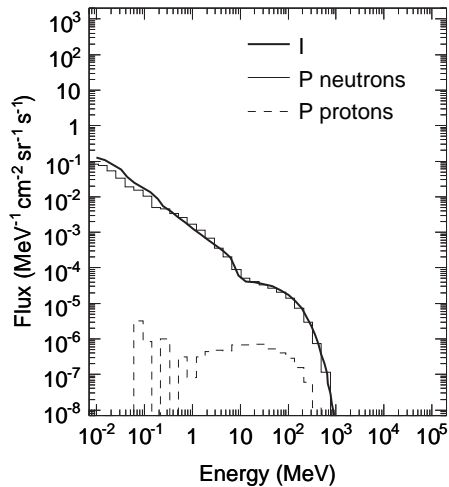


Figure 7.24: Kinetic energy spectra of particles entering the Columbus cabin due to incident cosmic ray albedo neutrons. Legend: I – Incident neutrons, P neutrons (protons) – Penetrating neutrons (protons).

7.7 Conclusions and comparison to experimental data

A direct comparison of the calculated dose rates for Columbus to measurements in the present ISS is difficult. First, the modules of the present ISS offer different shielding capabilities than Columbus. A detailed study of the radiation environment in other modules for a different ISS configuration would need compatible simulation geometry models. The present results can thus only be used for a general comparison. Secondly, dose rates for GCR ions are not negligible and are yet to be calculated. Nevertheless, assuming that the percentages of GCR ion contribution to dose rates and dose equivalent rates in Fig. 2.7 can be applied to the ISS orbit at both solar maximum and minimum, Table 7.2 can be constructed. Another method

to account for total GCR dose rates, could be to assume them to be of about equal size as the trapped proton induced dose rates [70].

Table 7.2: Final average total dose and dose equivalent rates for all locations inside Columbus. GCR total dose rates are scaled according to Fig. 2.7.

Radiation field component	Solar minimum			Solar maximum		
	$\mu\text{Gy/d}$	\bar{Q}	$\mu\text{Sv/d}$	$\mu\text{Gy/d}$	\bar{Q}	$\mu\text{Sv/d}$
Trapped protons (AP8)	120	1.3	154	79	1.3	102
GCR protons (CREME96)	64	1.4	92	45	1.4	64
GCR total (scaled)	161	7.1	1147	114	7.0	798
Total	281	4.6	1301	193	4.7	900

Total dose rates due to ionizing radiation in the range 153–231 $\mu\text{Gy/d}$ have been measured [71] at various locations in the U.S. Lab and Node 1 for altitudes in the range 386–404 km. The measurements were made in 2001, i.e., during a solar maximum and with ISS in a much less massive configuration. The simulation results depend on several parameters, such as type of incident radiation model. In the case of the well established models AP8 and CREME96 for trapped protons and GCR protons, respectively, the total solar maximum dose rate in Table 7.2 compares favorably with this measurement.

Further experimental data from [71] for solar maximum conditions and an ISS altitude of about 380 km are shown in Table 7.3. The variation in the reported data illustrates the uncertainty between different dosimetric techniques. Simulated dose rates due to trapped protons according to the AP8-MAX model agree well with the experimental data, staying within the uncertainty of dosimetric techniques. Also the simulated total (scaled) GCR dose rate agrees reasonably well with the data, differing only by about 25%.

The simulated trapped proton dose equivalent rate is about 30% lower than the experimental dose equivalent rate. However, the quality factor agrees with the one of the DOSTEL dosimeter. The simulated (and scaled) GCR total dose equivalent rate does not agree with the measurements. The simulation estimate is about a factor of two greater than the measurements. As a result of this, the discrepancy is also present in the simulated total dose equivalent rates.

SPE doses measured inside ISS during individual days of the solar events in 2001 and 2003 are reported in [72]. The maximum dose measured with a shielded detector is 3.2 mGy, although most of the measurements are below 1 mGy. This is compatible with the simulated SPE proton dose of 1.3 mGy according to the CREME96 worst-day model.

Table 7.3: Dose and dose equivalent rates inside ISS measured at solar maximum conditions according to [71] .

Dosimeter	Radiation field component	$\mu\text{Gy/d}$	Q	$\mu\text{Sv/d}$
DOSTEL	Trapped protons	102	1.2	126
	GCR	92	4.4	409
	Total	194	2.8	535
CR-39+TLD	Trapped protons	n/a	n/a	n/a
	GCR	n/a	n/a	n/a
	Total	197	2.1	413
TEPC	Trapped protons	74	1.8	130
	GCR	91	3.7	337
	Total	165	2.8	467

Chapter 8

Conclusions

Geant4 Monte Carlo simulations of the proton and neutron induced space radiation environment onboard Columbus/ISS has been carried out. This involves trapped protons, Galactic Cosmic Ray protons, Solar Particle Event protons and cosmic ray albedo neutrons space radiation components. Effects of different models of space radiation components were studied, as well as solar cycle and ISS altitude variations. Dependence on position inside Columbus was also evaluated. Calculated effects include kinetic energy spectra of particles penetrating into the Columbus cabin and resulting doses and dose equivalents inside Columbus. The result is a detailed characterization of the radiation environment inside Columbus and its effects on astronauts. These results have been reached based on several intermediate results, as detailed below.

The Geant4 particle transport toolkit was concluded to be suitable for studies of the effects of space radiation on astronauts inside heavily shielded spacecrafts. The Geant4 Binary Cascade model (BIC) of hadronic reactions is compatible with experimental data in the space radiation energy range. It also performs similarly as other particle transport tools used for space radiation shielding studies. The Binary Cascade model, combined with validated models of other types of particle reactions, was thus used for the simulations of the Columbus radiation environment presented here. Additionally, the Geant4 Bertini Cascade model (BERT) was shown to perform similarly as the Binary Cascade model. However, serious discrepancies between experimental data and the Geant4 leading-particle biased model (LEAD), as well as the parameterized model of hadronic reactions (LHEP) were demonstrated, leading to the conclusion that they are unsuitable for space radiation shielding studies.

In this work Geant4 geometry models of Columbus and ISS were developed and validated. The models are computationally stable. No verified software instabilities due to the geometry models have been experienced during several hundreds of CPU-days of simulation. Results for the most advanced Columbus geometry model (Columbus3) are comparable to a much less detailed Columbus geometry

model (Columbus2). All differences are within the limits set by uncertainties in the incident space radiation environment. This leads to the conclusion that minor improvements to the Columbus3 geometry model would be irrelevant, except possibly for detailed studies of location-dependent doses, and that any modification to the geometry model would need to be comprehensive in order to modify the simulation results significantly. Furthermore, it indicates that depending on application, other projects may not need to expend resources on the development of equivalently detailed models of their simulation geometries. It also deserves to be mentioned that, to date, five projects have expressed interest in using the DESIRE geometry models for other ISS applications.

The trapped proton and GCR proton induced location-averaged dose and dose equivalent rates resulting from Geant4 calculations were compared to experimental dose rates from the latest solar maximum. Dose rates resulting from incident anisotropic trapped protons have been found to be lower, or equal to, those of omnidirectional models. A possible problem using Geant4 for future studies of effects induced by high-energy GCR ions was assessed. Part of the calculation involved scaling GCR proton dose rates according to results presented elsewhere [18], in order to obtain total GCR dose rates. The calculated trapped proton dose rates are $120 \mu\text{Gy/d}$ and $79 \mu\text{Gy/d}$ for solar minimum and maximum conditions, respectively. GCR dose rates are estimated based on calculated GCR proton dose rates to $161 \mu\text{Gy/d}$ and $114 \mu\text{Gy/d}$, respectively. The calculated dose rates were comparable with measurements, deviating by less than the expected uncertainty in the incident radiation environment. However, the similarly calculated dose equivalent rates are about a factor of two greater than the measured dose equivalent rates. The discrepancy is due to the scaling of GCR proton dose equivalent rates made to obtain total GCR dose equivalent rates. Additionally, the dose rate due to cosmic ray albedo neutrons was demonstrated to be negligible and simulated worst-day SPE proton doses in Columbus were comparable to measurements made in other parts of ISS.

Results for the GCR ion induced radiation environment onboard Columbus have not yet been calculated in the DESIRE project. Recent development of Geant4 physics models will allow for this, putting the goal of the DESIRE project within reach: A complete and detailed characterization of the Columbus radiation environment.

Acknowledgments

The work described in this thesis would not have been possible without the help and support, as well as patience, of many people.

First of all, I would like to thank my supervisor Prof. Bengt Lund-Jensen for having given me the opportunity to work in the Particle and Astroparticle Physics group at the Royal Institute of Technology (KTH) and do the research which led to this thesis. I also thank Prof. Em. Per Carlson and Astronaut/Dr. Christer Fuglesang for initiating this project. I am grateful for the enthusiasm you have shown for my research and the efforts you have made to help me make this a good thesis. I hope you too now can rest and allow yourselves some time off.

This work is the result of the DESIRE project, which is financed by ESA and the Swedish National Space Board. ESA has also provided travel support for the DESIRE project. Computing resources made available by a grant from the Göran Gustafsson Foundation are acknowledged.

I am deeply grateful to all my colleagues in the DESIRE group: Per Carlson, Eamonn Daly, Christer Fuglesang, Irena Gudowska, Bengt Lund-Jensen, Ramon Nartallo, Petteri Nieminen, Mark Pearce, Giovanni Santin, Nikolay Sobolevsky. You have all provided an immense amount of help, support and good ideas. Irena Gudowska also provided the SHIELD-HIT results in chapter 5.

I would like to thank Dr. Francis Cucinotta for making my brief visit to NASA Johnson Space Center interesting and enjoyable and for helping me use the BRYN-TRN program. I am grateful to Daniele Laurini of ESA for obtaining the ISS and Columbus geometry specifications. I gratefully acknowledge the efforts of Diego Dellantonio and Don de Wilde of ESA and Michael Louka and Niels-Kristian Mark of IFE to provide STEP and IGES CAD models of Columbus.

To everyone who has been working in my group the past five years: Thanks for making our group such a great place to work! Though sometimes too much... in the words of my office-mate Per Hansson: "Det här är ju heeelt sjuukt!"

I also want to thank my family, and my friends. Especially Rickard Armiento and Jon Jensen for the times we have enjoyed during the last couple of years, and for understanding my frustration over technical details in my research.

...and finally... Thank you ♥Eeva-Liisa♥ for being so wonderful! I love you sweetheart!!! Without your love it would never have been possible for me to complete this work!

List of Abbreviations and Names

ACE	Advanced Composition Explorer spacecraft
ACR	Anomalous Cosmic Ray
AE8	Model of Earth's trapped electron environment
AP8	Model of Earth's trapped proton environment
AP8-MAX	Solar maximum version of the AP8 model
AP8-MIN	Solar minimum version of the AP8 model
API	Application Programming Interface
AU	Astronomical UnitThe mean distance between the Earth and the Sun, about $150 \cdot 10^9$ m
BERT	Geant4 Bertini Cascade model
BIC	Geant4 Binary Cascade model
BRYNTRN	Baryon transport computer code
CAD	Computer-aided design
CAM	Centrifuge Accomodation Module
CATIA	CAD-system
CERN	European Organization for Nuclear Research
CR-39	Type of dosimeter
CRAND	Cosmic Ray Albedo Neutron Decay
CREME96	Cosmic Ray Effects on Micro-Electronics (1996 revision) A NASA supported web-interface to models of the space radiation environment developed by the U.S. Naval Research Laboratory. See also [3].
CRRES	Combined Release and Radiation Effects Satellite

CRRESPRO	Model of Earth's trapped proton environment at solar maximum
CSG	Constructive Solid Geometry
DESIRE	Dose Estimation by Simulation of the ISS Radiation Environment
DOSTEL	Type of dosimeter
EPF	External Payload Facility
ESA	European Space Agency
ESP	Emission of Solar Protons model
G4BERT	Geant4 physics list LHEP_BERT_HP
G4BIC	Geant4 physics list LHEP_BIC_HP
G4LEAD	Geant4 physics list LHEP_LEAD_HP
G4LEPPC	Geant4 physics list LHEP_PRECO_HP
GCR	Galactic Cosmic Ray
GHEISHA	Gamma- Hadron- Electron- Interaction SH(A)ower code
GOES	Geostationary Operational Environmental Satellite
GPS	General Particle Source A Geant4 module that allows the user to generate particles according to energy, angular and spatial distributions.
HZETRN	High-charge-and-energy transport computer program
I-DEAS	CAD-system
ICRU	International Commission on Radiation Units and Measurements
IFE	Norwegian Institute for Energy Technology
IGES	CAD file format
IMF	Interplanetary Magnetic Field
INC	Intra-Nuclear Cascade
ISPR	International Standard Payload Rack
ISS	International Space Station
JEM-PM	Japanese Experiment Module-Pressurized Module

JEM-PS	Japanese Experiment Module (Experiment Logistics Module)-Pressurized Section
JPL-91	Model of SPE protons Named according to originating institute, the U.S. Jet Propulsion Laboratory.
JQMD	Jaeri QMD
LEAD	Geant4 leading particle biased model of hadronic reactions
LEO	Low-Earth Orbit An orbit of less than about 1200 km altitude and with a non-polar inclination.
LEP	Large Electron-Positron Collider
LET	Linear Energy Transfer
LHC	Large Hadron Collider
LHEP	Geant4 Parameterization Driven models of hadronic reactions
MARS	Monte Carlo program for inclusive simulation of particle cascades in matter
MDPS	Meteoroid and Debris Protection System
MSC	Mobile Servicing Center
NASA	U.S. National Aeronautics and Space Administration
NOAA	U.S. National Oceanic and Atmospheric Administration
NOAAPRO	Model of Earth's trapped proton environment
PDGF	Power and Data Grapple Fixture
PFA	Port Feedthrough Aft
PFF	Port Feedthrough Forward
PMA	Pressurized Mating Adapter
PSB97	Model of Earth's trapped proton environment at solar minimum
QMD	Quantum Molecular Dynamics
ROOT	An Object-Oriented Data Analysis Framework
SAA	South Atlantic Anomaly
SAMPEX	Solar Anomalous and Magnetospheric Particle Explorer spacecraft

SHIELD	Monte Carlo hadron transport code
SHIELD-HIT	Extension of SHIELD to heavy-ion transport
SIREST	Space Ionizing Radiation Environments and Shielding Tools A NASA web-interface to models of the space radiation environment. See also [19].
SPE	Solar Particle Event
SPENVIS	Space Environment Information System An ESA supported web-interface to models of the space radiation environment. See also [2].
SSN	Sunspot Number
STEP	Standard for the Exchange of Product model data
STS	Space Transportation System
TEPC	Type of dosimeter
TIROS	Television Infrared Observation Satellite program
TLD	Type of dosimeter
UP	An anisotropic model of Earth's trapped proton environment
UP-MAX	Solar maximum version of the UP model
UP-MIN	Solar minimum version of the UP model
Z1	Zenith 1 Integrated Truss Assembly

List of Figures

1.1	Photo of ISS taken from the space shuttle Discovery in August 2005 (courtesy of NASA).	3
1.2	ISS ground track for three consecutive orbits.	4
1.3	ISS altitude history since launch. The most recent data in the plot are from 5 August 2005 (altitude data courtesy of NASA).	4
2.1	The IMF and propagation of energetic particles from the Sun (adapted from [9]).	8
2.2	The SSNs from 1750 until today (according to [10]).	9
2.3	The magnetosphere viewed in the Earth's orbital plane (adapted from [11]).	10
2.4	Motion of trapped particles in the geomagnetic field (adapted from [11]).	11
2.5	The Earth's radiation belts and the SAA.	11
2.6	SPE particle fluences for the October-November 2003 and January 2005 events according to [13]. Data are from the ACE, SAMPEX and GOES- 11 spacecrafts. The lines are not actual data and are only intended to improve the clarity of the plot.	15
2.7	Contribution to fluence, dose and dose equivalent from the different ion species at solar minimum according to [18]. The lines are only intended to improve the clarity of the plot.	18
3.1	Trapped electron fluxes >1 MeV for the AE8 model at solar minimum.	20
3.2	Trapped proton fluxes >50 MeV for the AP8 model at solar minimum. .	22
3.3	Kinetic energy spectra of incident trapped protons at ISS altitudes for different models.	24
3.4	Incident anisotropic trapped proton angle and kinetic energy differential spectrum for an ISS orbit at 380 km altitude at 100 MeV according to the AP8-MIN based UP-MIN model. The flux is plotted by the reversed primary particle direction in a coordinate system where the polar angle (θ) is measured from the velocity vector and the azimuthal angle (ϕ) from the zenith direction.	25

3.5 Comparison of models of orbit-averaged GCR proton kinetic energy spectra for 380 km altitude. Solar minimum (maximum) models labeled with MIN (MAX).	26
3.6 Kinetic energy spectra of incident SPE protons for an ISS altitude of 380 km altitude and disturbed magnetosphere according to ESP and CREME96 SPE models.	27
3.7 The cosmic ray albedo neutron kinetic energy spectrum for a 380 km altitude ISS orbit according to SIREST.	28
 5.1 Directional neutron spectra comparisons. 113 MeV protons incident on stopping length aluminum target cylinder (radius 3.65 cm, length 4.03 cm). The data for the different angles have been separated using the indicated scale factors.	39
5.2 Directional neutron spectra comparisons. 256 MeV protons incident on near stopping length aluminum target cylinder (radius 8.00 cm, length 12.15 cm). The data for the different angles have been separated using the indicated scale factors.	40
5.3 Directional neutron spectra comparisons. 256 MeV protons incident on stopping length aluminum target cylinder (radius 8.00 cm, length 20.0 cm). The data for the different angles have been separated using the indicated scale factors.	41
5.4 Directional neutron spectra comparisons. 113 MeV protons incident on stopping length beryllium target cylinder (radius 3.65 cm, length 5.70 cm). The data for the different angles have been separated using the indicated scale factors.	42
5.5 Directional neutron spectra comparisons. 113 MeV protons incident on stopping length carbon target cylinder (radius 3.65 cm, length 5.83 cm). The data for the different angles have been separated using the indicated scale factors.	43
5.6 Directional neutron spectra comparisons. 256 MeV protons incident on near stopping length carbon target cylinder (radius 8.00 cm, length 17.45 cm). The data for the different angles have been separated using the indicated scale factors.	44
5.7 Directional neutron spectra comparisons. 256 MeV protons incident on stopping length carbon target cylinder (radius 8.00 cm, length 30.0 cm). The data for the different angles have been separated using the indicated scale factors.	45
5.8 Directional neutron spectra comparisons. 113 MeV protons incident on stopping length iron target cylinder (radius 3.65 cm, length 1.57 cm). The data for the different angles have been separated using the indicated scale factors.	46

5.9 Directional neutron spectra comparisons. 256 MeV protons incident on near stopping length iron target cylinder (radius 8.00 cm, length 4.70 cm). The data for the different angles have been separated using the indicated scale factors.	47
5.10 Directional neutron spectra comparisons. 256 MeV protons incident on stopping length iron target cylinder (radius 8.00 cm, length 8.00 cm). The data for the different angles have been separated using the indicated scale factors.	48
5.11 Directional neutron spectra comparisons. 113 MeV protons incident on stopping length U-238 target cylinder (radius 4.00 cm, length 3.00 cm). The data for the different angles have been separated using the indicated scale factors.	49
5.12 Directional neutron spectra comparisons. 256 MeV protons incident on near stopping length U-238 target cylinder (radius 4.00 cm, length 3.00 cm). The data for the different angles have been separated using the indicated scale factors.	50
5.13 Directional neutron spectra comparisons. 256 MeV protons incident on stopping length U-238 target cylinder (radius 4.00 cm, length 5.00 cm). The data for the different angles have been separated using the indicated scale factors.	51
5.14 Energy deposition comparisons to SHIELD-HIT. 202 MeV protons incident on a water cylinder (radius 10 cm, length 30 cm). The simulation results obtained with the different Geant4 models overlap in Figs.(b) and(c).	54
5.15 Neutron spectra comparisons to SHIELD-HIT for neutrons leaving boundary surfaces of target water cylinder.	55
5.16 Particle spectra comparisons to BRYNTRN for particles exiting the slab in the forward direction.	56
 6.1 Comparison of the DESIRE Geant4 ISS model to the model in the specification [62].	58
6.2 The forward part of ISS.	58
6.3 Transparent view of the U.S. laboratory in the Geant4 ISS model.	59
6.4 The truncated ISS model.	61
6.5 The Columbus1 model.	62
6.6 The full Columbus3 model and the external experiments viewed from the forward-starboard direction.	63
6.7 The Columbus3 MDPS panels and support structures viewed from the port direction.	64
6.8 Details and interior of the Columbus3 model.	65
 7.1 Kinetic energy spectra of particles entering the Columbus cabin due to incident belt protons according to the AP8 model for solar maximum. Legend: I – Incident, P – Penetrating.	73

7.2	Kinetic energy spectra of particles entering the Columbus cabin due to incident GCR protons according to the CREME96 model for solar maximum. Legend: I – Incident, P – Penetrating.	74
7.3	Dose rates inside the Columbus cabin for trapped protons and GCR protons for different geometry configurations at solar maximum.	75
7.4	Kinetic energy spectra of particles entering the Columbus cabin at different altitudes due to incident trapped protons. The spectra correspond to solar minimum conditions according to the AP8 model. Legend: I 380 – Incident trapped protons at 380 km altitude, P 380 – Penetrating protons or neutrons at 380 km altitude, etc.	76
7.5	Dose rates from all particles as well as only penetrating primary protons inside the Columbus cabin at different altitudes. The dose rates correspond to solar minimum conditions according to the AP8 model.	77
7.6	Kinetic energy spectra of particles entering the Columbus cabin for different models of the incident trapped proton environment. Legend: I – Incident, P – Penetrating.	78
7.7	Dose rates from all particles as well as only penetrating primary protons inside the Columbus cabin. The dose rates correspond to different trapped proton environment models for solar minimum and maximum conditions.	79
7.8	Dose rates for the AP8 and PSB97 models at solar minimum as a function of primary proton energy.	79
7.9	Dose equivalent rates from all particles as well as only penetrating primary protons inside the Columbus cabin. The dose rates correspond to different trapped proton environment models for solar minimum and maximum conditions.	80
7.10	The AP8-MIN total dose rate from Fig. 7.7 as a function of the reversed primary proton direction.	81
7.11	The AP8-MIN total dose rate at the port edge of the Columbus cabin as a function of the reversed primary proton direction. The dose rate is shown with the same color scale as in Fig. 7.10. Any off-scale dose rates are shown as the maximum dose rate.	82
7.12	The AP8-MIN total dose rate at the center of the Columbus cabin as a function of the reversed primary proton direction. The dose rate is shown with the same color scale as in Fig. 7.10. Any off-scale dose rates are shown as the maximum dose rate.	82
7.13	The AP8-MIN total dose rate at the starboard edge of the Columbus cabin as a function of the reversed primary proton direction. The dose rate is shown with the same color scale as in Fig. 7.10. Any off-scale dose rates are shown as the maximum dose rate.	83
7.14	Dose rates in all 15 ICRU spheres due to incident belt protons according to the AP8 model for solar minimum. The longitudinal position is listed on the abscissa and the radial position in the legend.	84

7.15 The total dose rate (shown in Fig. 7.7) due to a UP-MIN anisotropic trapped proton flux as a function of the reversed primary proton direction. The dose rate is shown with the same color scale as in Fig. 7.10. Any off-scale dose rates are shown as the maximum dose rate.	84
7.16 Kinetic energy spectra of particles entering the Columbus cabin due to incident GCR protons according to different models. Legend: I – Incident, P – Penetrating.	86
7.17 Dose rates from all penetrating particles as well as dose rates itemized by particle species inside the Columbus cabin. The dose rates correspond to different GCR proton environment models for solar minimum and maximum conditions. Legend: C96 – CREME96, etc.	87
7.18 Dose equivalent rates from all penetrating particles as well as dose equivalent rates itemized by particle species inside the Columbus cabin. The dose equivalent rates correspond to different GCR proton environment models for solar minimum and maximum conditions. Legend: C96 – CREME96, etc.	87
7.19 Dose rates at solar minimum for incident GCR protons according to the CREME96 model as a function of primary proton energy.	88
7.20 The CREME96 total dose rate for solar minimum at all locations in the Columbus cabin as a function of the reversed primary proton direction. The dose rate is shown with the same color scale as in Fig. 7.10. Any off-scale dose rates are shown as the maximum dose rate.	88
7.21 Kinetic energy spectra of particles entering the Columbus cabin due to incident SPE protons according to the CREME96 worst-day scenario. Legend: I – Incident SPE protons, P protons (neutrons) – Penetrating protons (neutrons).	89
7.22 Doses inside Columbus due to different SPE proton scenarios for all penetrating particles and for penetrating primary protons only. The “Worst day” and “Worst week” scenarios are according to the CREME96 SPE proton model. The “Worst event” and “Year” scenarios are according to the ESP model for a confidence level of 95%.	90
7.23 Doses for incident solar protons according to the CREME96 worst day and the ESP worst event scenarios as a function of primary proton energy.	90
7.24 Kinetic energy spectra of particles entering the Columbus cabin due to incident cosmic ray albedo neutrons. Legend: I – Incident neutrons, P neutrons (protons) – Penetrating neutrons (protons).	91

List of Tables

2.1	The radiation weighting factor w_R according to particle type and energy (adapted from [16]).	17
6.1	The MDPS and hull thicknesses for different surfaces of Columbus. . . .	62
7.1	Labeling of geometry configurations and number of CPU-days required on AMD Athlon 2000+ processors for the results presented in this thesis.	71
7.2	Final average total dose and dose equivalent rates for all locations inside Columbus. GCR total dose rates are scaled according to Fig. 2.7. . . .	92
7.3	Dose and dose equivalent rates inside ISS measured at solar maximum conditions according to [71]	93

Bibliography

- [1] J. W. Wilson, et al., NASA TP-3643.
- [2] D. Heynderickx, et al., AIAA-2000-0371 (2000). (See also <http://www.spenvisoma.be/>)
- [3] A. J. Tylka, et al., IEEE Trans. Nucl. Sci. 44 (1997) 2150. (See also <https://creme96.nrl.navy.mil/>)
- [4] S. Agostinelli, et al., Nucl. Instrum. Methods A 506 (2003) 250. (See also <http://geant4.cern.ch/>)
- [5] J. Allison, et al., IEEE Trans. Nucl. Sci. 53 (2006) 270.
- [6] R. Brun and F. Rademakers, Nucl. Instrum. Methods A 389 (1997) 81. (See also <http://root.cern.ch/>)
- [7] T. Eermark, et al., IEEE Trans. Nucl. Sci. 51 (2004) 1378.
- [8] T. Eermark, et al., “Implementation of a detailed Geant4 geometry model of the International Space Station and the Columbus module,” submitted to Rad. Meas.
- [9] D. F. Smart and M. A. Shea, “Solar radiation,” Encyclopedia of Applied Physics 18 393.
- [10] R. A. M. Van der Linden and the SIDC team, “Online catalogue of the sunspot index,” Web page: <http://www.sidc.be/sunspot-data/>.
- [11] National Council on Radiation Protection and Measurements, “Radiation protection guidance for activities in low earth orbit,” NCRP Report 132 (2000).
- [12] T. A. Farley, et al., Phys. Rev. Lett. 25 (1970) 47.
- [13] R. A. Mewaldt, et al., 29th ICRC 1 (2005) 111.
- [14] International Commission on Radiological Protection, “Relative biological effectiveness (RBE), quality factor (Q), and radiation weighting factor (w_R),” ICRP Publication 92 (2003).

- [15] International Commision on Radiation Units and Measurements, "Phantoms and Computational Models in Therapy, Diagnosis and Protection," ICRU Report 48 (1992).
- [16] International Commision on Radiological Protection, "1990 Recommendations of the International Commision on Radiological Protection," ICRP Publication 60 (1990).
- [17] ECSS-E-10-12 Working Group, ECSS-E-10-12 Draft 0.10 (2005).
- [18] F. A. Cucinotta, et al., Gravitational and Space Biology Bulletin 16 (2003) 11.
- [19] R. C. Singleterry, Jr., et al., Phys. Med. 17 (2001) 90. (See also <http://sirest.larc.nasa.gov/>)
- [20] J. I. Vette, "The NASA/National space science data center trapped radiation environment model program (1964-1991)," NSSDC report 91-29 (1991).
- [21] D. Heynderickx, et al., IEEE Trans. Nucl. Sci. 46 (1999) 1475.
- [22] J. D. Meffert and M. S. Gussenhoven, "CRRESPRO documentation," PL-TR-94-2218, Environmental resaerch papers no. 1158 (1994).
- [23] S. L. Huston and K. A. Pfitzer, IEEE Trans. Nucl. Sci. 45 (1998) 2972.
- [24] G. D. Badhwar and A. Konradi, J. Spacecr. Rockets 27 (1990) 350.
- [25] R. A. Nymmik, et al., Nucl. Tracks Radiat. Meas. 20 (1992) 427.
- [26] G. D. Badhwar and P. M. O'Neill, Adv. Space Res. 17 (1996) 7.
- [27] D. Heynderickx of BIRA (private communication).
- [28] J. W. Wilson, et al., NASA TP-3495 (1995).
- [29] J. H. King, J. Spacecr. Rockets 11 (1974) 401.
- [30] J. Feynman, et al., J. Geophys. Res. 98 (1993) 13281.
- [31] M. A. Xapsos, et al., IEEE Trans. Nucl. Sci. 47 (2000) 486.
- [32] M. A. Xapsos, et al., IEEE Trans. Nucl. Sci. 46 (1999) 1481.
- [33] J. W. Wilson, et al., Health Physics 57 (1989) 665.
- [34] J. W. Wilson, et al., NASA TM-2002-211668 (2002).
- [35] R. Brun, et al., "Detector Description and Simulation Tool," CERN Program Library (1993).
- [36] J. W. Wilson, et al., NASA TP-2887 (1989).

- [37] G. D. Qualls, et al., “International Space Station radiation shielding model development,” 31st International Conference on Environmental Systems (2001).
- [38] A. V. Dementyev and N. M. Sobolevsky, Rad. Meas. 30 (1999) 553.
- [39] I. Getselev, et al., Adv. Space Res. 34 (2004) 1429.
- [40] A. Heikkinen and N. Stepanov, arXiv:nucl-th/0306008. (See also [43])
- [41] G. Folger, et al., Eur. Phys. J. A 21 (2004) 407. (See also [43])
- [42] N. V. Mokhov, Fermilab-FN-628.
- [43] “Geant4 7.0 Physics Reference Manual,” Web page: <http://geant4.web.cern.ch/geant4/G4UsersDocuments/UsersGuides/PhysicsReferenceManual/html70/PhysicsReferenceManual.html>.
- [44] A. Ferrari and P. R. Sala, “The Physics of High Energy Reactions,” Proceedings of the Workshop on Nuclear Reaction Data and Nuclear Reactors Physics, Design and Safety (1996).
- [45] H. Fesefeldt, PITHA 85-02 (1985).
- [46] “Geant4 Process/Model Catalog,” Web page: http://geant4.cern.ch/support/proc_mod_catalog/index.shtml.
- [47] T. Koi, “Geant4 ion-ion interaction tests,” Web page: <http://www.slac.stanford.edu/~tkoi/G4IonInteraction.html>.
- [48] V. Andersen, et al., Adv. Space Res. 34 (2004) 1302.
- [49] H. Iwase, et al., J. Nucl. Sci. Tech. 39 (2002) 1142.
- [50] P. Truscott, et al., “Ion-nuclear models for the analysis of radiation shielding and effects (IONMARSE) – contract final report,” ESA contract 17191/03/NL/LvH.
- [51] T. Koi, et al., “Interfacing the JQMD and JAM nuclear reaction codes to Geant4,” arXiv:physics/0306115.
- [52] K. Niita, et al., Phys. Rev. C 52 (1995) 2620.
- [53] T. Ersmark, ESA contract 15613/01/NL/LvH.
- [54] G. A. P. Cirrone, et al., “Precision validation of Geant4 electromagnetic physics,” Conference Record of the 2003 IEEE-NSS, N23-2.
- [55] K. Amako, et al., IEEE Trans. Nucl. Sci. 52 (2005) 910.
- [56] I. Gudowska, et al., Phys. Med. Biol. 49 (2004) 1933.

- [57] M. M. Meier, et al., Nucl. Sci. Eng. 102 (1989) 310.
- [58] M. M. Meier, et al., Nucl. Sci. Eng. 104 (1990) 339.
- [59] International Commission on Radiation Units and Measurements, “Stopping power and ranges for protons and alpha particles,” ICRU Report 49 (1993).
- [60] M. S. Clowdsley, et al., Can. J. Phys. 78 (2000) 45.
- [61] T. Ersmark, ESA contract 15613/01/NL/LvH.
- [62] NASA, “International Space Station on-orbit assembly, modeling, and mass properties data book; revision Q - supplemental,” JSC 26557 (July 2003).
- [63] “ESA - Human Spaceflight - International Space Station - Columbus: European Laboratory,” Web page: http://www.esa.int/export/esaHS/ESAFRG0VMOC_iss_0.html.
- [64] Excerpt with drawings from [65].
- [65] Astrium GmbH, “APM QR vol. 2; Design definition report,” COL-RIBRE-DP-0009 (Aug. 2004).
- [66] ESA, “Columbus: the first milestone,” On Station; The newsletter of the directorate of manned spaceflight and microgravity, nb. 2, pp. 4-5 (2000). (Available: <http://esapub.esrin.esa.int/onstation/os2.pdf>)
- [67] D. Dellantonio of ESA-ESTEC (TOS-MCS) (private communication).
- [68] T. Guisan of ESA-ESTEC (HME-GSS) (private communication).
- [69] G. D. Badhwar and F. A. Cucinotta, Radiat. Res. 153 (2000) 1.
- [70] E. R. Benton and E. V. Benton, Nucl. Instrum. Methods B 184 (2001) 255.
- [71] G. Reitz, et al., Radiat. Prot. Dosim. 116 (2005) 374.
- [72] V. V. Benghin, et al., Adv. Space Res. 36 (2005) 1749.